AN EXPERIMENTAL INVESTIGATION OF THE PERFORMANCE OF INSULATING WINDOWS - WIND LOADS AND DYNAMIC RESPONSE

A THESIS

Presented to

The Faculty of the Division of Graduate

Studies and Research

By

Ravindra B. Deo

In Partial Fulfillment

of the Requirements for the Degree

Doctor of Philosophy

in the School of Aerospace Engineering

Georgia Institute of Technology

June 1977

AN EXPERIMENTAL INVESTIGATION OF THE PERFORMANCE OF INSULATING WINDOWS - WIND LOADS AND DYNAMIC RESPONSE

Approved:

J. I. Craig, Chairman

R. L. Carlson

S. V. Hanagud

D. P. Giddens

B. J. Goodno

Date Approved by Chairman 6/2/77

ACKNOWLEDGMENTS

It is with greatest pleasure that I record here my deep gratitude to Dr. James I. Craig for the unfailing encouragement and the guidance he has given me during the course of this research work. I am indebted to him for many enlightening discussions, and the philosophy of experimental research that he has given me over the course of my graduate studies and also throughout this work.

I would like to thank Dr. Robert L. Carlson and Dr. Sathyanarayana V. Hanagud for their constructive criticism, and careful examination of this manuscript. My thanks are due to Dr. Don P. Giddens and Dr. Barry J. Goodno who offered valuable suggestions.

I also wish to thank Ms. Gloria Larson for the immaculate job she has done in typing this thesis.

Finally, I wish to thank my parents who gave me their wholehearted encouragement and made all this possible.

TABLE OF CONTENTS

LIST OF TABLES

LIST OF ILLUSTRATIONS

NOMENCLATURE

A_i	Constants in rotationally restrained plate solution
a_o, a_1, a_{mn}	Acceleration
a, b	Plate dimensions
b	Bias error of the estimator
B_i	Constants in rotationally restrained plate solution
C_p	Pressure coefficient defined by $p/\frac{1}{2}\rho\bar{v}^2$
$C_{p_{rms}}$	Root mean square pressure coefficient
C'_p	Root mean square about the mean pressure coefficient
$C_{p_{max}}$	Maximum pressure coefficient
$\overline{C}_p$	Mean pressure coefficient
C_{p_i}	Internal pressure coefficient
CPLS	Constant Parameter Linear System
D	Flexural stiffness of the plate
d_i	Characteristic dimension on the i^{th} floor
E	Expectation operator
F_o, F_1, F	Force
F_S	Sampling rate
F_{max}, f_N	Nyquist Frequency (F_{max} in Fourier Analyzer terms)
f_a	Frequency above resonance, where Re part of compliance reaches a peak
f_b	Frequency below resonance, where Re part of compliance reaches a peak
Δf	Frequency resolution
Δf_n	Half-power bandwidth of the resonant peak n

FFT	Fast Fourier Transform
f	Frequency
$G_{ii}(f)$	One-sided power spectral density of random process $\{i\}$
$G_{ij}(f)$	One-sided cross-power spectral density between input i and output j
$\hat{G}(f)$	Raw estimate of $G(f)$
$\tilde{G}(f)$	Smoothed estimate of $G(f)$
G, G_1, G_2	Gust factors
g	Gust factor
G_{xx}^R	Reduced power spectral density of the differential pressure
$H(s), H(f)$	Transfer, Frequency response function
$h(\tau)$	Impulse response
K_z	Velocity pressure coefficient
K_m	Gust material factor
K_δ	Linear spring constant
K_θ	Rotational spring constant
$K_{\delta mn}$	Linear spring stiffness in the mn^{th} mode
$m(t)$	Noise at the input
$n(t)$	Noise at the output
N	Total number of points in a digitized signal
n_d	Number of disjoint records
$p(x)$	Probability Density Function of x, pdf
Δp	Differential pressure across the window
Δp_g	Pressure differential in the air gap due to a volume change ΔV
P_1	Design wind pressure
PSD	Power Spectral Density

Q	Quality factor $\lvert H(f)\rvert_{max}$
$R_{ij}(\tau)$	Correlation function between random processes i and j
Re	Reynolds Number $= \frac{\bar{v}d}{\upsilon}$
$S_{ij}(f)$	Twosided spectral density function
$T(f)$	Transmissibility function
T	Length of a disjoint record, $T = \frac{1}{\Delta f}$
T_S	Total length of the record $T_S = n_d T$
$u(t)$	True input to a linear system
$u_R(t), U_R(f)$	The rectangular time window and its Fourier transform
$v(t)$	True output of a linear system with input $u(t)$
$w_H(t), W_H(f)$	The Hanning window and its Fourier Transform
$w_i(t)$	Internal glass plate displacement
$w_e(t)$	External glass plate displacement
$w(x, y, t)$	Displacement function of the glass plate
X_m, Y_n	Eigenvectors of a rotationally restrained beam
$X(f), Y(f)$	Fourier Transforms of $x(t)$ and $y(t)$
$\{x(t)\}, \{y(t)\}$	Stationary random processes
z	Height
α	Slope $\frac{\partial w}{\partial x}$
ϵ_r	Normalized random error
ϵ_b	Normalized bias error
$\phi(f)$	Phase angle
φ	Parameter of a random process or building profile coordinate
γ^2_{xy}	Coherence function between input x and output y
ψ^2_x	Mean square value of a signal

ζ	Damping coefficient = $c / \sqrt{2Km}$
υ	Kinematic viscosity
$\overline{\theta}$	Mean wind direction
ξ	Nondimensional frequency, $\xi = f.d / v$
ξ_A, ξ_B	Rotational restraint parameters
ρ_{xy}	Correlation Coefficient
ρ	Density in slugs/ft^3

SUMMARY

Full scale measurements were carried out on a glass clad medium high-rise building in an effort to characterise the dynamic wind loads on the cladding and to assess the dynamic response of typical window installations. The experimental study strived to investigate the direct effects of the wind on windows in a tall building from a phenomenological point of view rather than aiming at the acquisition of design wind load information. The wind loads acting on windows were characterized with respect to their frequency content and a qualitative sketch of their dependence on the building profile was composed. A unique application of the coherence function was utilized to quantify the extent to which the dynamic response of the window units is caused by the wind loads. Use of the coherence function also permitted isolation of window vibration sources other than the wind loads.

The window unit was modelled as an elastically interconnected double plate system and the natural frequencies of undamped motion obtained. The resonant frequencies of the window unit were also determined in-situ by impulse testing.

In general, the overall levels of the wind pressure spectra are quite small in a frequency bandwidth encompassing the first few natural modes of the double plate system, and would require considerable dynamic amplification by structural vibration to approach static load levels. However, an isolated case of significant dynamic loading in the range of 6-16 Hz was observed and the response of the window was found to be

highly coherent with the wind loads. This observation, on one of the lower floors, was attributed to the effects of the surrounding terrain and served to demonstrate the existence of critical response locations on the building facade.

CHAPTER I

INTRODUCTION

In recent years, architectural innovation has led to an increased usage of glass in the cladding or "skin" of tall buildings. All cladding is by definition nonstructural; however, it has to withstand forces arising from a variety of sources, for example, pressure loads due to wind and sonic boom, impact due to windborne debris, and interactive structural loading due to building frame distortions. In traditional engineering practice greater analytical attention has been given to major building components, e.g. building frame, than to architectural details such as the building cladding or window systems. The principal reason is, of course, that the failure of a major component would be catastrophic. However, the frequent failure of windows and cladding to perform as intended and the fact that the cladding can now account for 10-20% of the initial building cost, has noticeably increased the economic risk for advanced design concepts. A thorough reexamination of cladding design practices is, therefore, warranted.

The formulation of a rational design procedure for modern window and curtainwall construction involves consideration of a large number of loading mechanisms. These are better described in the form of a diagram, (Fig. 1), where the various loadings are considered as composed of static and dynamic components. The relative magnitudes of these factors among themselves as well as the severity of dynamic loading has not yet been

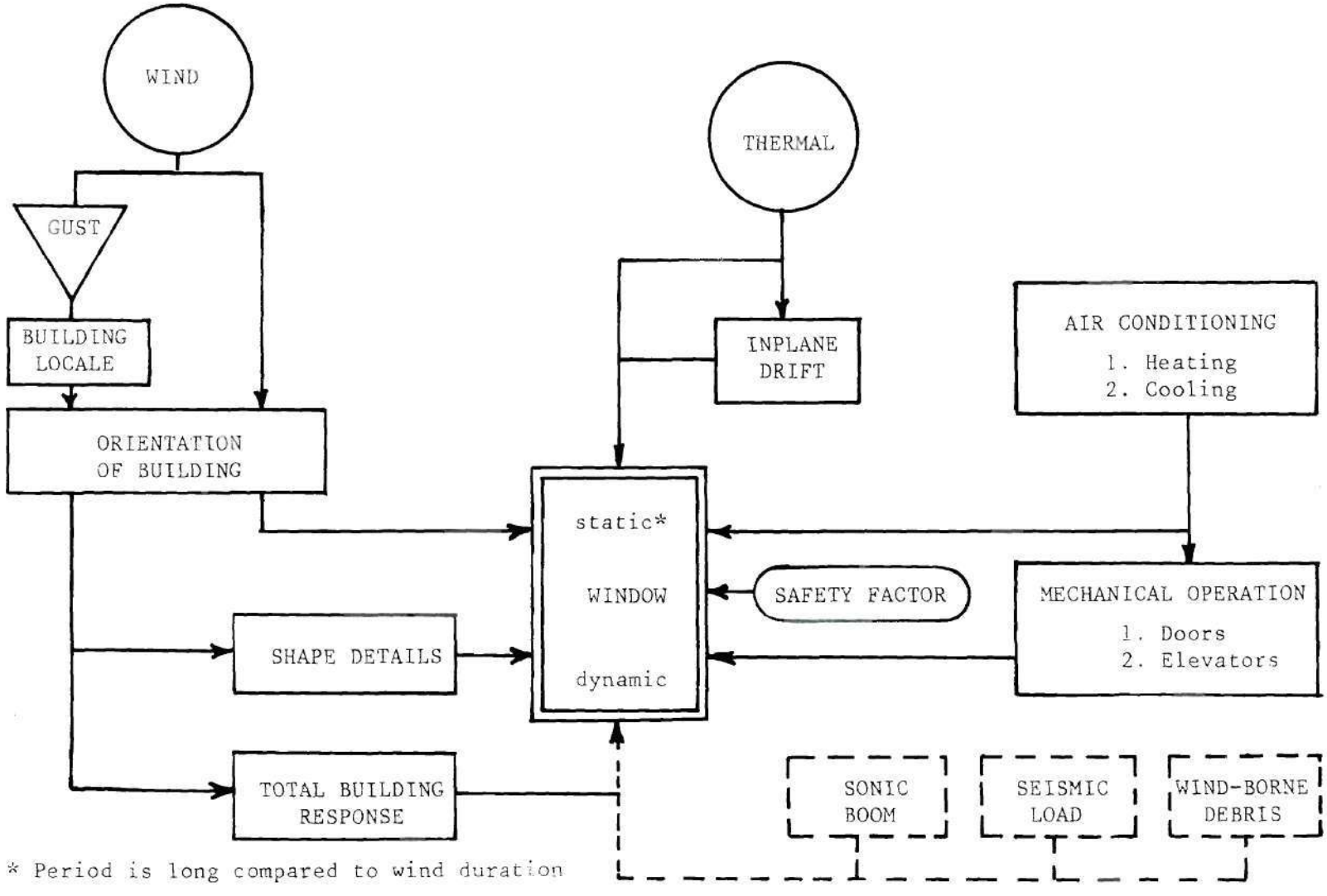

Figure 1. Factors Which Affect the Performance of Curtain Walls in High Rise Construction.

established. At the same time, the dynamic response of windows and cladding is not fully understood. As can be anticipated, the overall problem of identifying the major factors affecting the design and performance of building claddings is complex. Consequently, any program of study which aims to unravel this situation must be defined with respect to the complete problem but must necessarily be directed at only a specific facet.

The use of lightweight panelling and extensive areas of glass in the cladding of tall buildings, for reasons both of economy and aesthetics, has rendered modern high-rise buildings increasingly vulnerable to wind induced damage. In fact, the pattern of failures as recently documented in Refs. 1, 2, 3, and 4, suggests that wind forces constitute a major consideration in the design of elements of the exterior curtain wall. In developing rational procedures for the wind-resistant design of windows, an accurate description of the local wind pressure loading and an understanding of the nature of its effects (as well as the failure modes) is of paramount importance.

The nature of wind forces acting on windows is determined not only by the wind characteristics, but also by the wind-structure interaction phenomena. Even though wind forces on buildings have been of concern in the past, the fluid mechanics related to buildings in atmospheric boundary layer winds is not well understood. Unlike the aerodynamics of streamlined bodies which is highly developed for aeronautical applications, the aerodynamics of bluff buildings in turbulent, nonhomogeneous boundary layers is complex and is not well described by either analytical or numerical techniques. Consequently, the available wind force

information for buildings and structures has been obtained primarily from measurements on small scale models and in limited instances on actual structures.

Boundary layer wind tunnel measurements on tall buildings have shown that the wind structure interaction gives rise to fluctuating local wind pressures. It has been recognized that, whereas the temporal and spatial fluctuations of the local wind pressures from the mean may not affect the design of the primary structure, their effect on portions of the building such as windows and cladding panels cannot be ignored. Model tests have also shown that the most severe pressure fluctuations are associated with the following mechanisms:

a. Separation and reattachment of flow around buildings [5].

Flow separation around buildings can induce locally high suction (outward acting) pressures which often exceed the dynamic pressure of the mean wind. Probability density estimates of pressure fluctuations on tall building models indicate [6] that in regions of separation, negative values of the peak pressure coefficient $C_{p\ max}$ attain magnitudes of 8-10 times the rms pressure coefficient $C_{p\ rms}$ quite frequently. The local separation and reattachment is strongly affected by the geometrical features of the building such as triangular outsets and reentrant corners. The most severe pressure fluctuations have been found to occur at reentrant corners where flow separating at one edge of the corner reattached at the opposite edge [5].

b. Local vortex formation due to the shape of the building and its exterior architectural features and the subsequent shedding of these vortices.

Vortex flows may be developed by a particular combination of building shape and wind direction, and are responsible for periodicities in the cladding loads. In addition, the great variety of architectural treatments of the building facade lend themselves to the generation of vortices and thus pressure pulsations of various frequencies and amplitudes. Model studies of the Bank of America World Headquarters Building [7], show that fluted walls in conjunction with setbacks at various elevations are the main reasons for the appearance of various vortex flows over the entire wall surface. The shedding of these vortices is one of the primary aerodynamic phenomena which develop periodic forces on the building as well as its cladding.

The frequency content of both types of pressure fluctuations is of concern in defining wind loads for window glass and cladding panels, since sufficient energy at frequencies in the vicinity of panel resonance can result in dynamic amplification of deflections and stresses. However, the available spectral data from either model or full scale tests is rather sparse. Upwind surface pressure fluctuation spectra for a pair of square section towers have been measured on a model [8] and show that most of the pressure fluctuation energy is concentrated in the low frequency range extending to about 20 Hz. These spectra have been found to be related closely to turbulence spectra of the simulated oncoming wind.

A number of full scale tests on existing structures have provided a greater insight into the nature and severity of surface pressure fluctuations on tall buildings. Some of the pertinent full scale tests are surveyed in Table 1, partially reproduced from Reference 9. Newberry

Table 1. A Partial Survey of Full Scale Investigations of Wind Effects on Tall Buildings

Investigators	Ref.	Building		Experimental Procedure				Analysis		
				Pressure		Wind		Pressure		
		Type	Ht. in ft.	Ext.	Int.	V	Dir.	Mean	Histo-gram	PSD
C. W. Newberry K. J. Eaton J. R. Mayne	10	R. C.	267	48	3	1	1	x	x	x
W. A. Dalgliesh W. von Tobel H. S. Ward	11, 12	St. Fr.	784	34	1	2	2	x	x	x
W. A. Dalgliesh W. von Tobel H. S. Ward	13	St. Fr.	430	12	0	1	1	x		x
Mario Takeuchi Gengo Matsui Satora Kazama Ryoichi Nagai	14	Comp. St./C	251	20	0	1	1	x	x	x
W. A. Dalgliesh W. von Tobel H. S. Ward	15	St. Fr.	640	12	0	1	1	x	x	x
S. Miyoshi Masahiko Ida T. Terayama	16	St. Fr.	482	6	6	2	2			x

*Abbreviations: St. = Steel; Fr. = Frame; R.C. = Reinforced Concrete;
Comp. = Composite Steel & Concrete

et al. [10] from their measurements on an 18-story rectangular building conclude that the most severe suction pressures occur under the incidence of glancing winds and large negative excursions are apparent at locations around corners. Dalgliesh [11] in comparing model and full scale pressure coefficients points out that large values of $C_{p\ rms}$ and hence large pressure fluctuations from the mean occur when the wind is nearly parallel to the building surface on which the tap is located. The data also demonstrate a reduction in wind pressures as the ground level is approached.

Full scale measurements by Dalgliesh [12] have provided valuable information on an important aspect of the wind loading mechanism: that of the nature of gust effects. Gust action on cladding is considered as random turbulent fluctuations superimposed on the mean wind. Actual pressure measurements on a tall building have been statistically analyzed for the maximum pressure or suction that can be expected to occur during the estimated lifetime of the cladding. Static cladding design loads have been defined taking into account a gust effect factor and exposure conditions (surrounding terrain).

Results of frequency decomposition of surface pressure fluctuations on actual structures have been presented in Refs. 13, 14, 15, and 16. Pressure spectra in References 13 and 14 have been obtained over a range of low frequencies pertinent to the vibrations of the entire building. Since the fundamental frequencies of window glass and cladding panels are typically in the range of 5-50 Hz, the results of Refs. 15 and 16 are significant in that the spectral bandwidth exceeds 10 Hz. Standen et al [15] have obtained power spectra of pressures on the surface of a

rectangular planform, high-rise building for various locations. These spectra are reproduced in Fig. 2. Rapid roll-off of power density with frequency characterises Figs. 2a, b, and d. However, the increased power at higher frequencies in Fig 2c with the pressure taps subject to glancing winds shows that some locations on the surface may be susceptible to dynamic loads.

Measurements of Miyoshi et al. [16] on a tall rectangular building appear to be the first set of data which provide response information in terms of glass panel strains in addition to pressure spectra. The pressure spectra measured under typhoon conditions are reproduced in Fig. 3. An interesting feature similar to that of Fig. 2c is apparent in Fig. 3 curve P_E, where the pressure fluctuations on the easterly wall possess significant energy at higher frequencies as compared to the sharp roll-off observed in the other spectra.

In the past few years the problem of determining wind loads for cladding design has generated a great deal of interest. This has resulted in an expanding experimental data base of both model and full scale results. Much of the work, however, has centered on the assumption of static or quasi-static pressures, and, therefore, on the specification of static loads for cladding panel design against outright fracture. Current building codes, as for example the ANSI Standard, allow for large pressure fluctuations and gusts by augmenting the static loads by gust and terrain factors. The basis for the static pressure assumption is the preliminary pressure fluctuation data for buildings with simple geometries. A majority of the measured pressure spectra indicate that for short span panels the resonance frequencies are considerably higher than

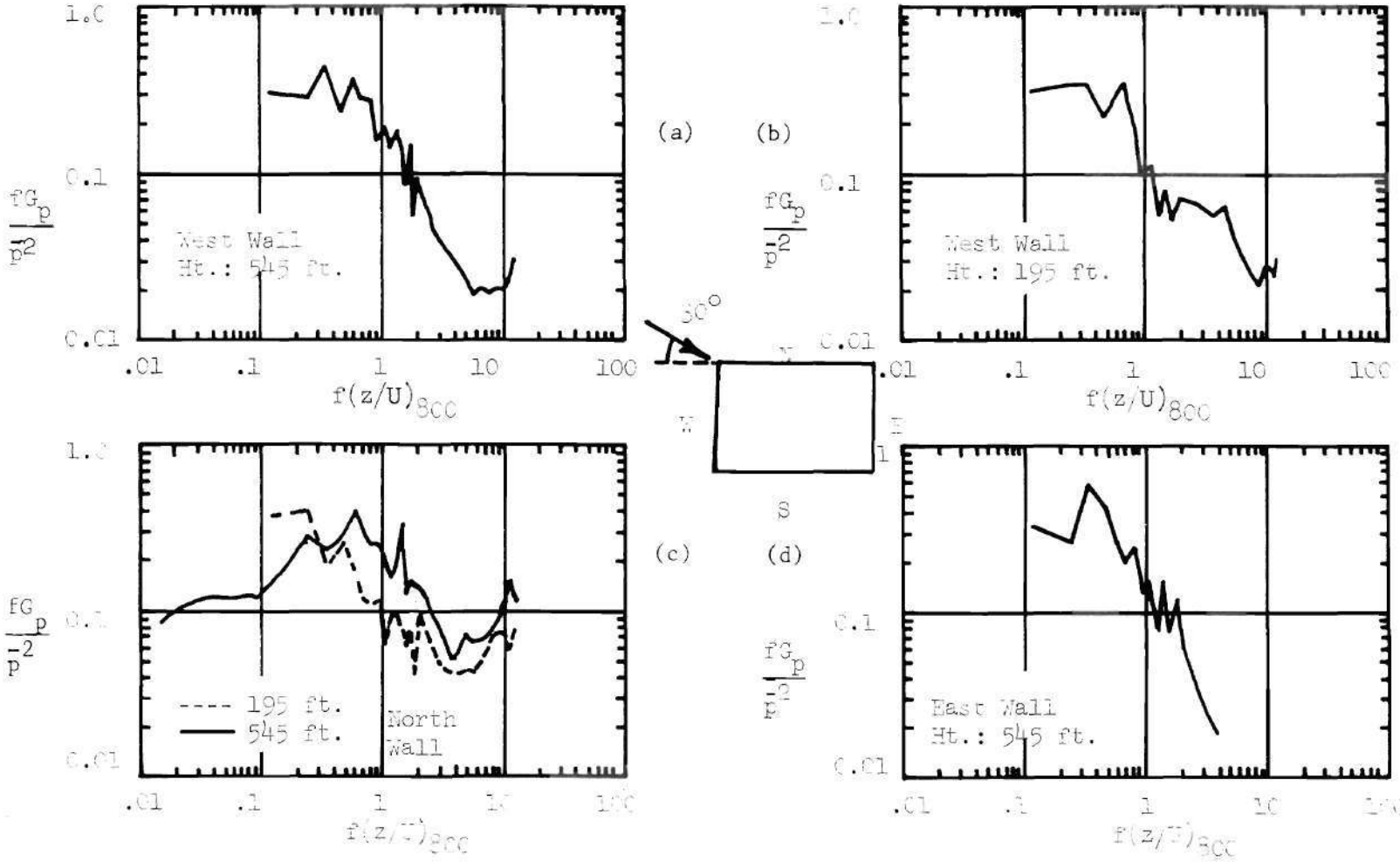

Symbols: f = frequency, $(z/U)_{800}$ = Height to velocity ratio at 800 ft., G_p = PSD

$\bar{p}^2$ = Mean square value of the pressure, U= 50 ft./sec.

Figure 2. Power Spectra From Full-Scale Tests of Standen et al. [15]

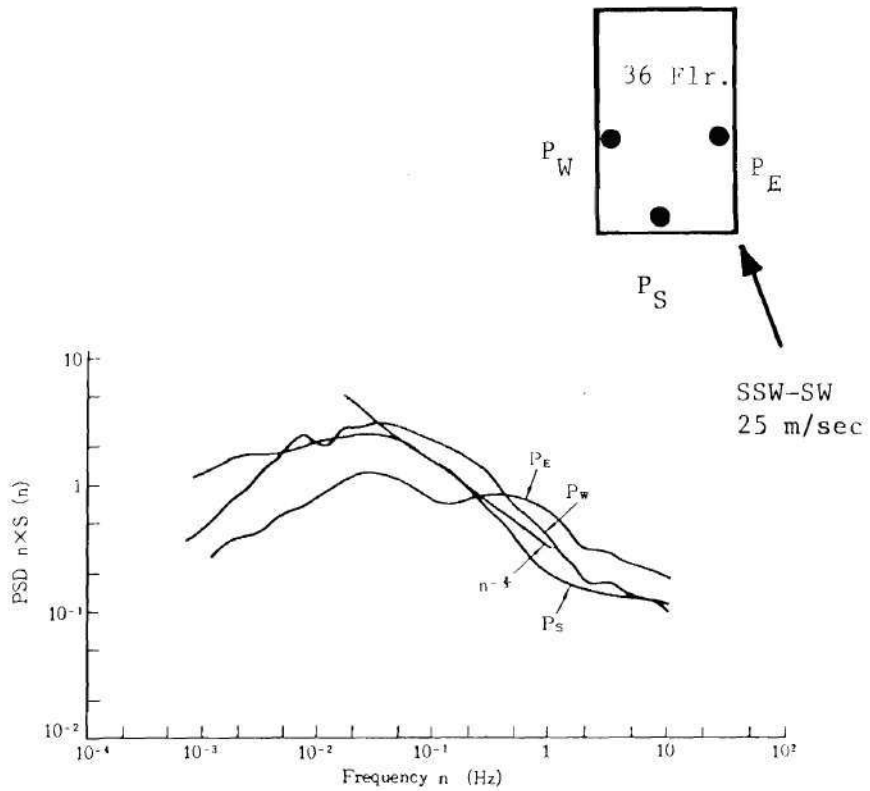

Figure 3. Power Spectra From Full-Scale Tests of Miyoshi et al. [16].

the significant pressure fluctuation frequencies. It has been acknowledged, however, that the nature and severity of local dynamic wind loads on buildings with complicated shapes such as those with fluted walls, reverse setbacks, and surface irregularities is not well understood [17, 18].

The results of Refs. 15 and 16 discussed above, hint at the existence of "critical response locations" where intense high frequency pressure fluctuations would necessitate consideration of dynamic loading mechanisms and their effects. Wind tunnel tests have illustrated that these critical response locations depend on the nature of the wind-structure interaction. Relatively large windows and cladding panels in these locations would be susceptible to vibration and flutter, and damage in the form of glass panel breakage, cladding panel fatigue failure, and panel anchor failure. Therefore, design of window glass for static loads, in such locations would be inadequate. In addition, design to minimize breakage may not in itself be a solution to the window failure problem.

The specification of dynamic wind loads for modern glass curtain walls has received little attention to date and the precise effects of such loadings have not been fully considered. Dynamic load considerations have been restricted to those arising from sonic boom and a rational design procedure for window glass subjected to an N-shaped sonic boom pressure wave has been proposed [19]. The extension of such a procedure to any dynamic loading although possible does not account for dynamic effects which may be of significance.

Wind loads for buildings under design can be obtained only by measurements on models in wind tunnels. However, to establish a systematic set of simulation criteria and to ensure the predictive quality of model test results, measurements on actual structures and model/full-scale comparisons are essential. Full scale tests are also of value in understanding the wind loading mechanisms and the characteristic response. However, since full scale experiments pertain to particular structures with unique properties and exposure conditions, an ensemble of such measurements need to be examined prior to rational definition of wind loads and formulation of design procedures.

It is the purpose of the present research to study the dynamic response characteristics of window installations, and to assess the properties and effects of the wind loading by conducting full scale measurements on a high-rise glass clad building. This approach to the problem of window design has been adopted to understand the nature of dynamic wind loads and heretofore unknown dynamic effects of 'normal' wind, and thus contribute to the evolution of a unified rational design philosophy.

CHAPTER II

LOADING AND RESPONSE IDENTIFICATION - THEORETICAL ASPECTS

Introduction

In formulating rational design procedures for the elements of a glass curtain wall, the first step is to translate the wind environment of buildings into a set of numerically defined loads. The kinds of failures that these loads might cause must then be studied in light of the different response mechanisms. This process leads to the formulation of a set of failure criteria. Once the loads have been defined and the failure criteria established, the design problem reduces to one of predicting the response of the window system, and evaluating this response in terms of the damage criteria.

The present study concerns itself with the problem of dynamic wind load and response identification for doubly glazed windows. Mathematical modelling of wind loading and the window response, in the strictest sense of identification is not within the scope of this work. Instead, a majority of the effort was devoted to an assessment of the wind loads and the window dynamic response with regard to the following:

(a) Capability of the wind loads to excite window vibrations and the dependence of the wind loads on the building profile.

(b) The degree of dependence of the window response on wind loads from amongst other excitation sources.

(c) Vibration parameters of the window system from measured data.

In this chapter the wind loading and response identification problem is formulated. Currently used static load specifications and the dynamic failure mechanisms which could warrant consideration in design are examined. Linear system theory with random forcing functions, its application to the definition of wind loads, and the evaluation of response are outlined.

Design Considerations

A prerequisite for a unified rational design procedure for window systems is: given a design wind velocity one should be able to predict the response of the system in the form of peak stresses, accelerations, deflections etc. This in turn requires mathematical models for the prediction of the aerodynamic forces of interaction of the main structure and the turbulent, gusty wind, and the response. The forces of wind-structure interaction can be aerodynamic as well as aeroelastic. In so far as window systems in building structures are concerned, only aerodynamic forces are important. Considering the current state-of-the-art, the greatest uncertainty is in defining the wind environment of buildings and translating it into cladding loads.

The American National Standards Institute ANSI 58.1-1972 standard [20] contains a method for determining wind loads applicable to the design of parts and portions of a building. Design wind pressures for window glass are assumed to be static and are defind by:

$$P_1 = .00256\, V_{des}^2\, K_z .\, G(C_p - C_{p_i}) \qquad (1)$$

where,

P_l is the design pressure in lbs./ft^2 (Psf)

V_{des} Fastest mile wind speed with a 50 year recurrence period, in MPH

K_z Velocity pressure coefficient which depends on the exposure and the height z above ground.

G Gust response coefficient

C_p External pressure coefficient

C_{p_i} Internal pressure coefficient

Minimum values of $C_p - C_{p_i}$ for locations susceptible to large suctions ($C_p - C_{p_i} < 0$)* are specified. The standard was founded on the available wind research and was prepared for use in conjunction with common building shapes (i.e. rectangular). A similar static wind load definition is employed by the National Building Code of Canada [21].

The current window design procedures, as for example that in the Southern Standard Building Code [22], assume the design pressure as a uniformly applied static design load. With this load, a factor of safety is used, the latter representing a value which has appeared to give an acceptable probability of breakage in extensive static strength tests conducted by window glass manufacturers [23].

Recent efforts at improving upon the static load specifications have been directed at modifying the gust factor G. In Ref. 17 it is suggested that G be expressed as:

---

*For example in the vicinity of corners.

$$G_1 = \left[1 + g.\frac{C_p'}{\overline{C}_p}\right] \qquad (2)$$

where g is a gust effect factor

C_p' rms value of the pressure coefficient about the mean, given by $C_p' = \sqrt{\frac{1}{T}\int_0^T (C_p - \overline{C}_p)^2 dt}$

$\overline{C}_p$ mean pressure coefficient

C_p instantaneous pressure coefficient

The gust effect factor g from Eq.(2) has values lying between 3 and 5 for windward faces, as determined experimentally. Allen and Dalgliesh [24] have proposed a gust factor G_2 which incorporates effects of dynamic wind loads on glass resistance as well as dynamic amplification. These dynamic effects are included in the gust factor as a "gust material" factor K_m with the reasoning that the effects are related only to the turbulent component of the wind. The gust factor is then expressed as:

$$G_2 = \left(1 + g.K_m.\frac{C_p'}{\overline{C}_p}\right) \qquad (3)$$

Design of window glass requires consideration of some of its unusual mechanical properties [Appendix A]. The statistical variation in glass strength, due to its sensitivity to surface flaws, is accounted for by designing on the basis of probability of breakage. Design

procedures for window glass considering its static fatigue* property have been proposed, where gust factors are replaced by pressure coefficients averaged over a period determined from the strength-load duration curves [25, 26]. Consideration of edge supports, clearances and glazing details has been emphasized in a design method [27] based on static pressures defined by the ANSI standard.

The widespread adoption of static design loads is a direct consequence of the available experimental data. The experimental data base has also provided valuable insight into the wind-structure interaction phenomena. However, the model test results are beset by a lack of confidence in their predictive quality. Full scale tests have been limited in their scope by the emphasis on measurements for validation of wind tunnel test techniques, and have used buildings with simple shapes. Wind load data for tall buildings with complex shapes, and for urban locations with upwind obstructions (such as in downtown areas), are still in the process of being assembled. Assessment of factors influential in specification of wind loads for curtain walls is as yet incomplete.

The local nature of failure of windows, especially those near the corners of a building, has been recognized. It is not unreasonable to suspect that the severe pressure fluctuations in the separation region at a corner of the building could excite the window dynamically as well. Buildings with the following shape characteristics are prime candidates for localized regions of relatively high frequency loading:

---

*In the accepted definition "static fatigue" implies decrease in breaking stress with increased duration of load.

(a) Setbacks or reverse setbacks along the height

(b) Fluted walls presenting a cascade of triangular outsets and reentrant corners to the flow

(c) Rough surface texture of the building facade as dictated by the architectural details.

These "critical response locations" would also depend upon the directional properties of the wind.

In regions where dynamic wind loads are severe enough to offset the alleviating effect of glass static fatigue, dynamic response of the glass panels becomes an important consideration. Ejection type failures, where relative motion between the glass and its frame is suspected, accentuate the need to define the response of the entire window assembly. A review of curtainwall damage caused by a hurricane [28] shows that all the components of a window assembly should be included in a rational design philosophy.

Dynamic Effects

The components of window systems on which measurements, to be described in the next chapter, were conducted are shown in Fig. 4. Such a system when subjected to dynamic loads, is susceptible to failure due to any of the dynamic effects listed below:

(a) Dynamic amplification of forces in the vicinity of panel resonance.

(b) Excessive deflection of the two glass panes coupled with out-of-phase dynamic response leading to contact and eventual breakage.

(c) Asymmetric vibrations of adjacent panels causing the open-

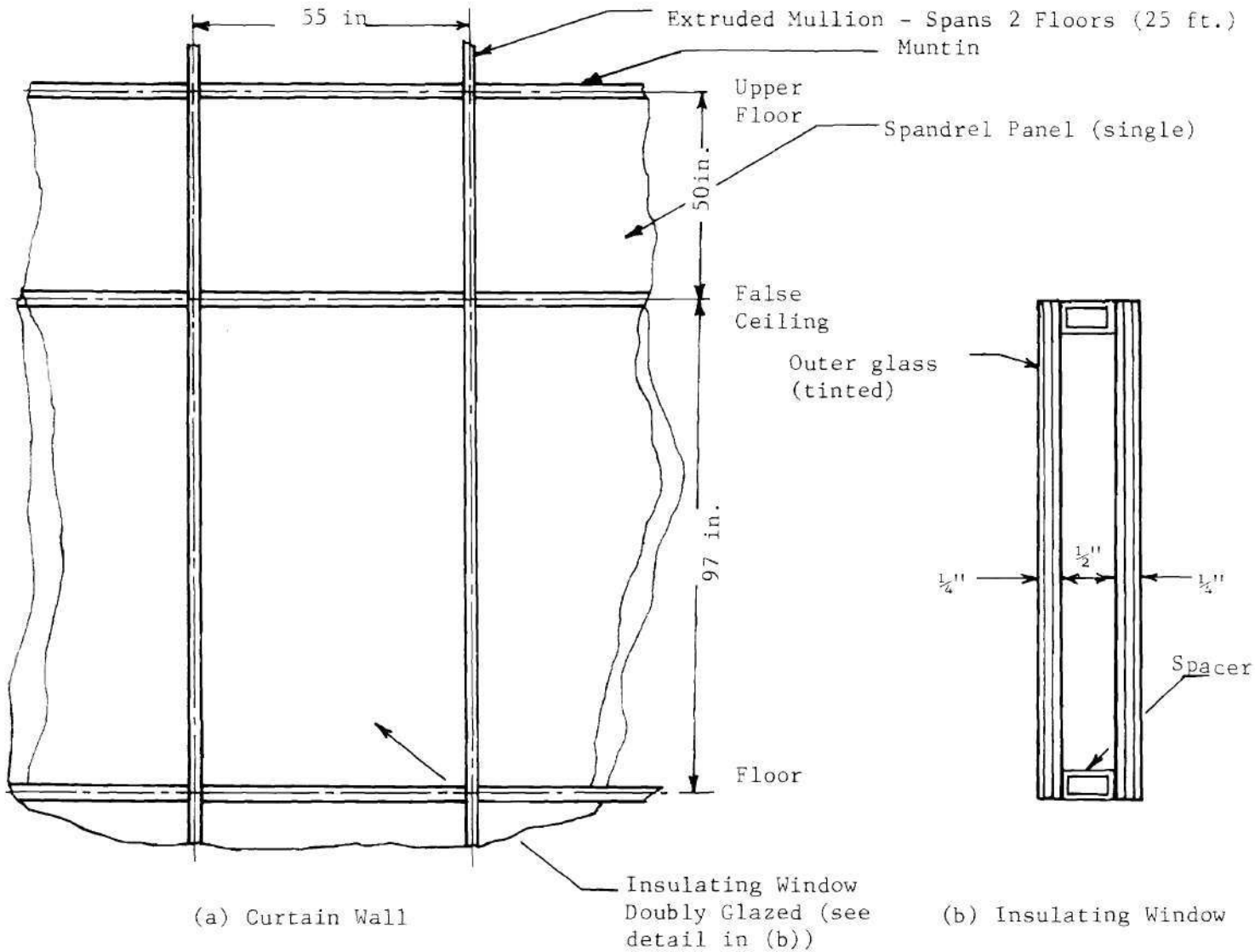

Figure 4. Components of a Curtain Wall and a Doubly Glazed Window Unit.

section mullions to twist. This can lead to glass breakage, mullion fixture failure, or mullion failure with subsequent glass ejection.

(d) Fatigue of the flaw sensitive glass.

Before any explicit means for the evaluation of these failure criteria can be established a complete understanding of the dynamic response of window assemblies is required. In addition, it is imperative that the dependence of critical response locations on the building profile and wind load characteristics be known. At the same time the severity of dynamic loads in these regions must be assessed.

The hypothesis that regions of relatively high frequency wind loading may exist on a building facade and that resistance to dynamic wind loads may have to be designed into window assemblies constitutes the subject of this research. The investigation was accomplished by full scale measurement of surface pressure fluctuations and window response. A detailed description of the experimental program is given in the following Chapter. At this stage it seems appropriate to briefly describe the analytical tools required for wind load characterization and response identification. To this end the window is modelled as a single input/single output system with the dynamic wind loads constituting the input. The loading and response identification problem for such a system is described in the following section.

The Window System as an Input-Output Model

Considering the model of Fig. 5, the present investigation is concerned with the inverse problem in engineering where the input to the system and the resulting response are measured and are to be used to

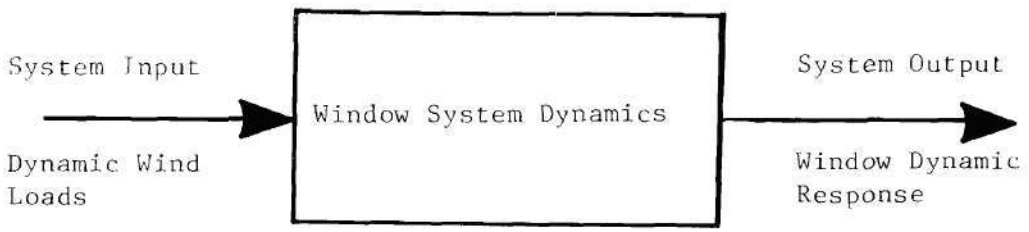

Figure 5. The Window System as an Input/Output Model.

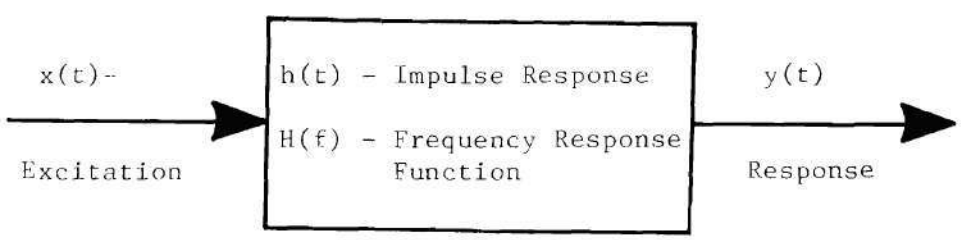

Figure 6. Single Input/Single Output Linear System.

describe the system dynamics as well as the input characteristics.

The input, i.e. the wind loading, itself can be visualized as the ouput of another system describing the wind flow interaction with the structure. In the present study this wind-structure interaction system identification is not considered. In this context the term load identification implies a study of the measured wind loading with respect to a *set of parameters describing* the wind characteristics and the building profile.

As is the case in the majority of real-world large systems, the window as a structural system is expected to have nonlinear and time dependent properties. These properties, for example, could be due to the fact that a window unit is an isolated part of an entire curtain wall, and that glass strength is sensitive to surface flaws which are affected by service load duration. The identification problem in this case can be formidable [29]. In this investigation, the nonlinearities of the system and its time dependent character are neglected. The system model is, therefore, simplified so that it can be described by linear, constant coefficient differential equations. The theory of linear system response to a random forcing function, therefore, can be readily used as an interpretive tool for the measured data.

Linear system theory is the mainstay of the data analyses procedures. In this approach the window assembly is assumed to be the linear system and the dynamic wind loads considered as the band-limited random input. The theoretical concepts are not new; however, their application to large structures is broader in scope, specifically, with respect to

the use of the coherence function in assessing the linear dependence of the response on the wind loads.

In the following sections, the salient features of the theory, and its application, in view of the research objectives are described.

Time Invariant Linear System

In the following the input-output relations for a stable linear system are briefly summarized.

A linear, time-invariant system also called a constant parameter linear system (CPLS) is one which can be described by linear differential equations with constant coefficients. The dynamic characteristics of a constant parameter linear system can be described by its impulse response function $h(\tau)$. The input-output relations for such a system, represented by the block diagram of Fig. 6, can be described by the convolution integral:

$$y(t) = \int_{-\infty}^{\infty} h(\tau)\, x(t-\tau)\, d\tau \qquad (4)$$

For a physically realizable system $h(\tau) = 0$, if $\tau < 0$. The system can also be described by a transfer function $H(s)$, which is the Laplace transform of $h(\tau)$:

$$H(s) = \int_{o}^{\infty} h(\tau) e^{-s\tau}\, d\tau \qquad s = a+jb \qquad (5)$$

An alternate representation of the transfer function is the frequency response function where $s = jw = j2\pi f$. The frequency response function

is the Fourier transform of $h(\tau)$ and is given by

$$H(f) = \int_{-\infty}^{\infty} h(\tau) e^{-j2\pi f\tau} d\tau \tag{6}$$

$h(\tau)$ and $H(f)$ are Fourier transform pairs. Taking Fourier transforms of both sides of Eq.(4) yields the input-ouput relation in the frequency domain

$$Y(f) = H(f)\ X(f) \tag{7}$$

Equation 7 can also be obtained as a direct result of a convolution theorem which states that convolution in the time domain is equivalent to multiplication in the frequency domain and vice versa.

The frequency response function $H(f)$ is a complex valued quantity and can be written in polar notation as:

$$H(f) = |H(f)| e^{-j\phi(f)} \tag{8}$$

For a physically realizable system the lower integration limit in Eq.(6) can be replaced by 0. Thus,

$$H(f) = \int_{0}^{\infty} h(\tau) e^{-j2\pi f\tau} d\tau \tag{9}$$

From Eq.(9) it follows that

$$H(-f) = H^*(f) \quad \text{*denotes complex conjugate}$$

$$\text{and, therefore} \quad |H(-f)| = |H(f)| \tag{10}$$

$$\phi(-f) = \phi(f)$$

If the excitation $x(t)$ is a sample function of a stationary random process $\{x(t)\}$ then $y(t)$ is a sample function of a stationary random process $\{y(t)\}$, as will be shown. The input-ouput relations for this case must be described in terms of the expected values of the input and the output. The expected value of any real single-valued continuous function $g(x)$ of the random variable x is given by:

$$E[g(x)] = \int_{-\infty}^{\infty} xp(x)dx \tag{11}$$

where, $p(x)$ is the probability density function of x. For stationary random processes, $\{x(t)\}$ and $\{y(t)\}$ the correlation functions are defined as follows:

$$R_{xx}(\tau) = E[x(t)\ x(t+\tau)]$$

$$R_{yy}(\tau) = E[y(t)\ y(t+\tau)] \tag{12}$$

and,

$$R_{xy}(\tau) = E[x(t)\ y(t+\tau)] \tag{13}$$

Equations 12 are the autocorrelation functions of $\{x(t)\}$ and $\{y(t)\}$ respectively. Equation 13 defines the cross correlation function between $\{x(t)\}$ and $\{y(t)\}$.

For the single input-single output linear system of Fig. 6 the ouput autocorrelation function can be obtained from the input autocorrelation function as follows:

$$y(t).y(t+\tau) = \int_0^\infty \int_0^\infty h(t_1)h(t_2)x(t-t_1)x(t+\tau-t_2)dt_1dt_2 \qquad (14)$$

The expected value of Eq.(14) yields [30]:

$$R_{yy}(\tau) = \int_0^\infty \int_0^\infty h(t_1)h(t_2)R_{xx}(\tau+t_1-t_2)dt_1dt_2 \qquad (15)$$

Thus the response of a CPLS to a stationary random input is a stationary random process. Similarly, the stationary cross-correlation function $R_{xy}(\tau)$ between the input $x(t)$ and the output $y(t+\tau)$ is:

$$R_{xy}(\tau) = \int_{-\infty}^{\infty} h(t).R_{xx}(\tau-t)dt \qquad (16)$$

The transformation of Equations 15 and 16 to the frequency domain yields input-output relations in terms of auto and cross-power spectral densities. These are:

$$\begin{aligned} S_{yy}(f) &= |H(f)|^2 S_{xx}(f) \\ S_{xy}(f) &= H(f)\, S_{xx}(f) \end{aligned} \qquad (17)$$

Where S_{xx}, S_{yy} and S_{xy} are the theoretical two-sided spectral density functions defined over $-\infty \leq f \leq \infty$ as:

$$S_{ij}(f) = \int_{-\infty}^{\infty} R_{ij}(\tau) e^{-j2\pi f\tau} d\tau \qquad \text{(Wiener-Khintchine Relations)} \qquad (18)$$

From symmetry properties of stationary correlation functions it is seen that S_{xx} and S_{yy} are real, non-negative, and symmetric functions of f, whereas S_{yx} is complex valued.

In practical situations, however, the negative frequencies have no real significance, and it is more convenient to define a practical power density function $G_{ij}(f)$, which exists for positive frequencies only,

$$\begin{aligned} G_{ij}(f) &= 2S_{ij}(f) \quad \text{for} \quad f \geq 0 \\ &= 0 \qquad\quad \text{otherwise} \end{aligned} \qquad (19)$$

Equation 17, therefore, can also be written as

$$\begin{aligned} G_{yy}(f) &= |H(f)|^2 G_{xx}(f) \\ G_{xy}(f) &= H(f) \cdot G_{xx}(f) \end{aligned} \qquad (20)$$

Equation (20) provides the basis for the physical application of linear system theory to the problem of dynamic loading and response of window systems.

The cross power spectral density function $G_{xy}(f)$, may be shown to satisfy the inequality [31]:

$$|G_{xy}(f)|^2 \leq G_{xx}(f) G_{yy}(f) \qquad (21)$$

From Eq.(21), a generalized cross-spectral density function, known as the coherence function may be defined,

$$\gamma^2_{xy}(f) = \frac{|G_{xy}(f)|^2}{G_{xx}(f)G_{yy}(f)} = \frac{|S_{xy}(f)|^2}{S_{xx}(f)S_{yy}(f)} \qquad (22)$$

where for random processes

$$0 \leq \gamma^2_{xy}(f) \leq 1$$

The Coherence Function

The coherence function, also known as mean squared coherence or the coherence coefficient, was introduced by Wiener [60] in 1930. The terminology was motivated by the interference effects of coherent, and incoherent light sources; however, the "coefficient of coherency" was derived as a natural extension of the theory of harmonic analysis of time series. Wiener also pointed out the analog between the coefficient of coherence and the correlation coefficient, ρ_{xy} between two random variables x and y defined as:

$$\rho_{xy} = \frac{C_{xy}}{\sigma_x \sigma_y}$$

where, C_{xy} is the covariance of x and y and σ_x and σ_y the standard deviations of x and y, respectively. It was remarked that the correlation coefficient is a tool for the statistical analysis of frequency series, where time does not enter as a parameter; whereas, the

coefficient of coherence is a tool in the analysis of time series.

For two stationary time series $x(t)$ and $y(t)$, the coherence function, Eq.(22), as a consequence of the Schwarz inequality, Eq.(21), is restricted to values between 0 and 1. For deterministic signals the coherence function can only take the values 0 or 1. As applied to stationary stochastic processes, the coherence function possesses the properties outlined below, which suggest several of its applications.

Consider the linear system configuration shown in Fig. 7, [52]. It is assumed that $s(t)$, $n_1(t)$, and $n_2(t)$ in Fig. 7 are sample functions of stationary uncorrelated random processes. By the application of Eqs.(20) and the basic relations for multiple input linear systems Ref. 31, pp. 147 , it can be shown that

$$\gamma^2_{y_1y_2} = \gamma^2_{r_1r_2} = \frac{G^2_{xx}(f)\left|H_a(f)H_b^*(f)\right|^2}{\left(G_{xx}(f)\left|H_a(f)\right|^2+G_{n_1n_1}(f)\right)\left(G_{xx}(f)\left|H_b(f)\right|^2+G_{n_2n_2}(f)\right)} \tag{23a}$$

where $*$ indicates the complex conjugate. The properties of the coherence function can now be summarized from Eqs.(22) and (23a) as follows:

1. The coherence function is a real valued function conveniently normalized to lie between zero and unity.

2. Since $\gamma^2_{y_1y_2}(f)$ is independent of $H_1(f)$ and $H_2(f)$ in Eq.(23a), the coherence function between two time series is not affected by the arbitrary linear processing of these signals. In other words, the coherence function is invariant under linear filtering operations.

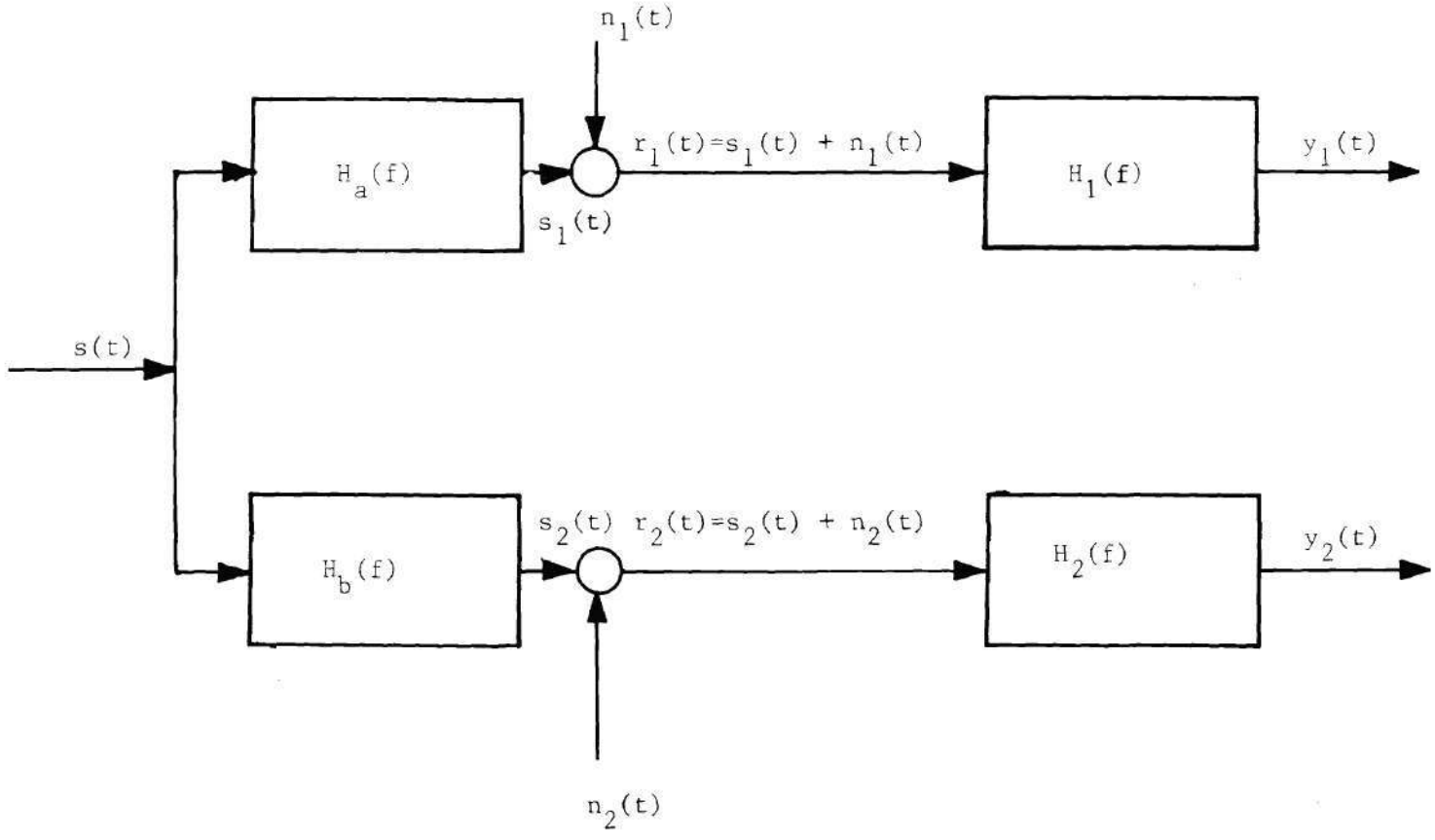

Figure 7. Configuration for Examining Properties of the Coherence Function.

3. With $n_1(t) = n_2(t) = 0$, $\gamma^2_{y_1y_2}(f) = 1$. Consequently the coherence function of two signals derived from the linear operations on the same signal is unity. Equivalently, the coherence of two linearly related signals is unity. It can be shown [37], that the coherence function is less than unity for any nonlinearities in the system, and the linear-to-nonlinear ratio (in the absence of noise) is given by

$\gamma_{y_1y_2}/1-\gamma_{y_1y_2}$.

4. For a linear system, the presence of noise, i.e. $n_1(t)$ and $n_2(t)$, tends to reduce the true value of the coherence function. In such a case $\gamma_{y_1y_2}/1-\gamma_{y_1y_2}$ is a measure of the signal to noise ratio.

5. An interesting property of the coherence function is obtained from its relation to the error spectrum resulting from a linear prediction $\hat{y}(t)$ of $y(t)$ from $x(t)$, described by [31]:

$$\hat{y}(t) = \int_o^\infty h_o(t)x(t-\tau)d\tau \tag{23b}$$

where $h_o(t)$ is a weighting function to be determined and $x(t)$, $y(t)$ are sample functions of a stationary stochastic process.

When the linear filter is chosen to minimize the mean square value of the error $e(t)$, i.e., the area under the error spectrum, where,

$$e(t) = E\left[\{ y(t) - \hat{y}(t)\}^2\right] \tag{23c}$$

the error spectrum takes the form [31, 34]:

$$G_{ee}(f) = [1-\gamma^2_{xy}(f)]G_{yy}(f) \qquad (23d)$$

Therefore, the error is small when the coherence function is near unity indicating that the y series can be predicted very well from the x series data. On the other hand when $\gamma^2_{xy}(f)$ is near zero, the error spectrum very nearly coincides with that of $y(t)$ and the $x(t)$ data contributes almost nothing to the predictability of $y(t)$. This property relates closely with the intuitive meaning of coherence, i.e., two time series can be described as "coherent" at a frequency f when $\gamma^2_{xy}(f) \simeq 1$. When $\gamma^2_{xy}(f) \simeq 0$, they are referred to as "incoherent". Alternatively, $\gamma^2_{xy}(f)$ is the proportion of $G_{yy}(f)$ contained in the linear component of $y(t)$, and $1-\gamma^2_{xy}(f)$ is the proportion of $G_{yy}(f)$ contained in the error, or, in the absence of noise, in the nonlinear component of $y(t)$.

Properties (3) and (5) indicate that the coherence function can be used as a measure of linearity. Furthermore, property (5) enables the use of the coherence function in establishing the degree of linear dependence of a system output $y(t)$, on the input $x(t)$. Property (4) indicates that the coherence function can be used in measuring the signal to noise ratio. It is because of these properties that the coherence function has found widespread application in communication systems [e.g. 61] in estimating the signal/noise ratio and determination of time delay. The coherence function has numerous other applications, as for example in control systems for system identification [62], and in

geophysics [63] to assess the signal to noise gain of an array of sensors.

The earliest applications of the coherence function to the structural dynamics of mechanical systems appear to be those of Kaneshige [64] and Barnoski [65]. The coherence function, however, was used only to assess the validity of the estimated frequency response functions.

A novel application of the coherence function in acoustic noise measurements [35] is based on the capability of $\gamma^2_{xy}(f)$ to determine if two signals that produce a spectral line are correlated. This property enables the detection of noise sources in a mechanical system.

The above application suggests use of the coherence function in the identification of loading sources that produce vibrations in a structural system. Recalling properties 3 and 5, it is seen that $\gamma^2_{xy}(f)$ can be used to assess the degree of linear dependence of the dynamic response of a structure on a particular loading source. With this point of view, the coherence function can be utilized to assess the causality in a complex system. For example, in the present study the coherence function can be used to evaluate the causality of the wind loads in exciting the dynamic response of window units or other elements of the curtain wall.

Theoretically, a similar assessment can, of course, be made by cross-correlation techniques. In fact, cross-correlation techniques have been applied to isolation of noise sources [66], where the technique was used for the separation of noise at a given point X into components according to the source, the transit time form the source to point X, and the frequency.

The choice of which approach to adopt for a particular problem can only be made when the overall objectives of the study and the methodology to be used have been established. If the problem description is based largely on a frequency domain formulation, for instance, using modal analysis or eigenvalue techniques, a transfer or frequency response function characterization is most appropriate, and use of the coherence function would provide more readily useable information. On the other hand, if a time domain formulation of the problem was made, for example, to study transient response behavior or transit time effects, then a correlation function approach would likely be preferable. Generally, the type of approach used in any situation will depend on the computational efficiency and the type of information desired, and the choice of using either the coherence or correlation function for source identification purposes must be made accordingly.

The modelling of the window system as an input/ouput system, and the choice between time-domain or frequency domain characterization of the structural system are discussed in the following sections.

Application To Dynamic Wind Loads and Window Response

The window assembly shown in Fig. 4, which together with smaller spandrel panels formed the exterior curtain wall of the building, is divided into two linear subsystems for the present application, Fig. 8.

Wind loads act on the double plate system formed by the two glass panes and through boundary connections are transmitted to the supports (shear forces in the case of simply supported boundary conditions). The

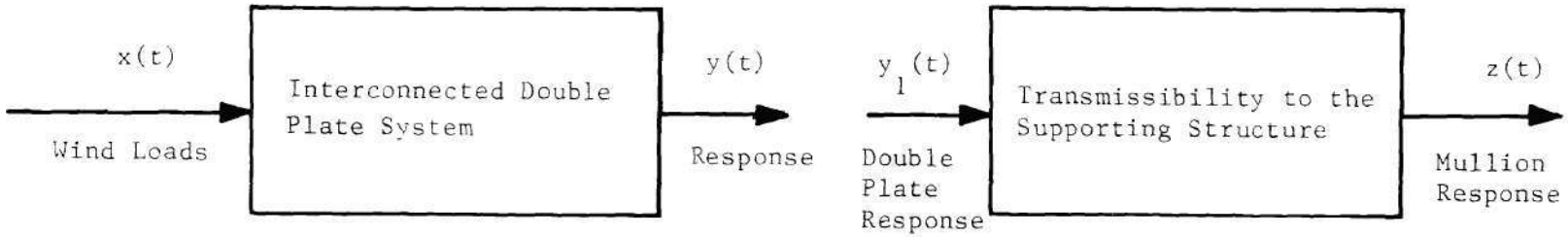

Figure 8. Subdivision of The Window Assembly Into Linear Systems.

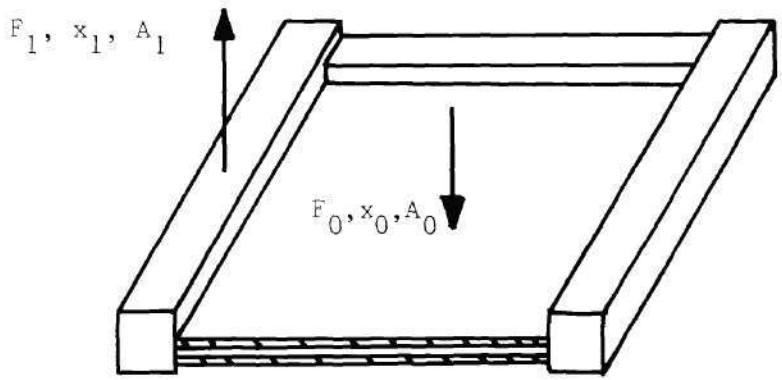

Figure 9. Definition of Transmissibility.

two systems are assumed to behave linearly under ambient wind loads*. The supports are assumed to be rigid for the evaluation of the transmissibility function defined below.

The input to the interconnected double plate system is the nondeterministic surface pressure due to the wind. The displacement response of the two plates, Fig. 4, was considered as the output. The input and the response parameters in the transmissibility model of the supporting structure depend on the definition of transmissibility used. From Fig. 9 the force transmissibility is defined as the magnitude of the ratio of the total force F_1 transmitted to the plate perimeter to the driving force F_o [32]. The force F_1 comprises a distributed force around the plate boundaries plus four discrete forces one at each plate corner. The displacement transmissibility is defined as the magnitude of the ratio of the displacement x_o of the midpoint of the plate to the displacement x_1 of its boundary [32]. As a result of a general transmissibility theorem [33] the two definitions are identical in the frequency domain. Furthermore, at any given frequency the displacement transmissibility is identical with the corresponding acceleration ratios:

$$|T(f)| = \left|\frac{F_1}{F_o}\right| = \left|\frac{x_o}{x_1}\right| = \left|\frac{A_o}{A_1}\right| \qquad (24)$$

---

* "Ambient Wind Loads" excludes unusually strong meterological phenomena such as tornadoes and hurricanes. Observations in strong squalls ($\bar{v}$ (0) 65 mph) indicated that static glass pane deflections comparable to glass thickness occur and linearity may not hold.

Since the rigid body accelerations can be measured with relative ease, in an experimental study, the acceleration ratio is generally measured.

The structural dynamic behavior of the two linear systems shown in Fig. 8 can be completely characterized by either their impulse response functions $h(\tau)$ and $s(\tau)$ in the time domain or by their transfer functions $H(f)$ and $T(f)$ in the frequency domain. The use of the transfer function i.e. frequency domain characterization is convenient in an experimental study where, as in the present case, the system characteristics are not known. Among the reasons for the choice are:

(a) the difficulties associated with interpreting the time domain response of a linear structure where several modes have been excited. This situation is aggravated if the modes are closely spaced.

(b) the ease with which background noise in the measured input and response can be minimized in frequency domain analyses.

(c) use of the Fast Fourier Transform (FFT) algorithm permits rapid analysis of voluminous data on a digital processor thereby providing greater computational efficiency in the estimation of frequency domain functions, e.g. power spectra.

The disadvantage of the frequency-domain viewpoint is that it is not directly applicable to nonlinear systems.

In the present application, however, the system behavior is assumed to be linear and only the steady state characteristics are of interest. Therefore, frequency domain representation of the CPLS is used, with Eqs.(20) and (22) providing the basis. The most severe restrictions in the use of this formulation are that the system must be

linear, time invariant, and the input must be a stationary random process.

The Input - Wind Loads

The natural wind turbulence together with the roughness effects of the earth's surface features cause the wind pressures on a building facade to be random in nature. Cladding loads, therefore, must be considered as a random process and described in terms of statistical functions. It appears reasonable to assume that over a short period of time the wind loads can be classified as stationary*. The frequency decomposition and distribution characteristics of the process can then be described by its power spectral density function (PSD) and amplitude probability density function (pdf).

The wind-structure interaction modifies the free stream wind properties i.e. the PSD's and the pdf's. The surface pressure frequency content and amplitude distribution depend on the following variables:

1. Surrounding terrain conditions or exposure.
2. Mean wind speed denoted by $\overline{v}$.
3. Mean wind direction $\overline{\theta}$.
4. Building profile assumed to be described by the parameters ϕ, and z. Where, ϕ denotes the surface location at a height z.

These features of the wind flow past a bluff body may combine to produce the following effects related to cladding loads in the time and frequency domain:

---

* The classification of cladding loads as stationary in light of the experimental data is discussed in Chapter IV.

I. Time domain - The descriptor in this case is the amplitude pdf.

(a) Variation in the magnitude of rms pressure fluctuations as indicated by the variance of the pdf.

(b) Variation in gust factors g as defined by Eq.(2).

(c) Negative peak C_p excursions as determined from the extreme values in the pdf.

II. Frequency Domain - The descriptor in this case is the power spectral density function and effects of interest are related to dynamic loading i.e. of bandwidth including at least the fundamental frequency of the window.

(a) Periodic forces due to vortex shedding.

(b) Narrow band pressure pulsations.

(c) Modification of the slope of the spectrum from the Kolmogorov inertial subrange spectrum which is proportional to $f^{-5/3}$.

(d) Variation in levels of the spectrum. This variation is related to the severity of dynamic loading.

To assess the dependence of these effects on the four variables mentioned above it is necessary to examine the roles each one of these plays in the present investigation.

(i) Terrain Conditions - The terrain surrounding the building used as the test site shows no characteristic variation and, therefore, can be eliminated from the list of independent variables.

(ii) Wind speed - Wind speed is converted to the nondimensional Reynolds number $Re = \frac{\bar{v}d}{\upsilon}$ where d is a characteristic dimension. The Reynolds number does not explicitly appear as a variable since it affects

the surface pressures only with a transition from one Reynolds number range to another.

(iii) Wind direction - The wind direction θ is an explicit variable in that it governs the relative pressure distribution on the building facade.

(iv) Building profile - The building geometry is best described in terms of a coordinate system similar to cylindrical. The coordinates ϕ and z can be visualized as a polar angle and the height, respectively. For a qualitative study, however, the angular description ϕ is discarded and instead ϕ is given discrete labels corresponding to the sites at which measurements were conducted.

If $x(t)$ is a random variable describing the instantaneous surface pressure, then a realistic functional form of the power spectral density can be hypothesized as:

$$G^R_{xx}(\xi) = F_x(\phi_z, z, \xi, \theta; R_e) \tag{25}$$

where,

$$G^R_{xx}(\xi) = \frac{G_{xx}(\xi)}{\frac{1}{2}\rho \bar{v}^2 \, 2} \quad \text{in 1/Hz} \qquad \text{is the reduced PSD}$$

ξ is the reduced frequency given by $\frac{f.d}{\bar{v}}$

Local pressures due to the wind may not necessarily follow the Gaussian distribution. Wind tunnel measurements [6] show that for the windward face of a structure, the local pressures follow the same distribution as expected for velocity fluctuations in the approach flow

(usually Gaussian for open exposure). For the leeward side, however, the positive local pressures show a generally Gaussian character whereas the large negative pressures are non-Gaussian. It has been pointed out by Davenport [34] that the strong negative tails are exponential in form. Since the pdf depends on the nature of the wind-structure interaction, the mean and the variance of the pdf of C_p's can be expected to have a functional form as follows:

$$\text{Mean} \qquad \overline{C}_p = C_1[\theta, \varphi_z, z; R_e] = \frac{\int_{-\infty}^{\infty} \Delta p \, . \, p(\Delta p) \, . \, d\Delta p}{\frac{1}{2} \rho \, \overline{v}^2}$$

$$\text{Standard Deviation} \qquad C_p' = C_2[\theta, \varphi_z, z; R_e] = \frac{\int_{-\infty}^{\infty} (\Delta p - \overline{\Delta p})^2 \, . \, p(\Delta p) \, . \, d\Delta p}{\frac{1}{2} \rho \, \overline{v}^2} \tag{26}$$

where, $p(\Delta p)$ is the probability density function of the surface pressure Δp and $\overline{v}$ is a mean reference velocity. Experimental investigation of the hypothesis of critical response locations, therefore, reduces to a parametric study of the functional forms of Eqs.(25) and (26). Load identification consists of examining the effects of the independent variables on the estimated PSD's and pdf's.

Causality of Wind Loads

There are several possible sources of the dynamic loading acting on a window system as mentioned in Chapter I. Therefore, the degree of linear dependence of the response on the direct wind loads must be known in order to establish the causality of wind loads in exciting the window response. This can be accomplished by means of the coherence function,

Eqs.(22) and (23). The use of a coherence function for identification of noise and vibration sources is a recently established technique [35, 36], although its meaning in communication theory has been known for several decades.

The theoretical coherence function is a measure of the linearity between two processes. In practical applications, however, measurement noise becomes an important consideration and the real valued coherence function may be simultaneously affected by the nonlinearity in the system and the measurement noise. When the system between the input and the output is linear then $\gamma^2_{xy}(f)$ assumes the value 1. Low values of the measured coherence function are indicative of:

(i) Extraneous noise present in the measurements,

(ii) The system relating $x(t)$ and $y(t)$ is not linear,

(iii) $y(t)$ is an output due not only to $x(t)$ but also other unspecified inputs (Partial coherence problem).

System linearity for multiple inputs is estimated from the multiple coherence function. For several correlated inputs the system linearity is determined from the partial coherence function. In the present application the ordinary coherence is used.

The Response

The frequency response function of the double plate system $\underset{\sim}{H}(f)$ can be represented in a matrix form as:

$$\underset{\sim}{H}(f) = \begin{bmatrix} H_{11}(f) & H_{12}(f) \\ H_{21}(f) & H_{22}(f) \end{bmatrix} \tag{27}$$

where $H_{ij}(f)$ is the ratio of the displacement response at plate j to an input force at plate i. The force to displacement transfer function is called the compliance transfer function. The elements of the transfer function matrix of Eq.(27) may themselves be matrices.

The frequency response function estimated from the measured input and output can be used to determine the vibration properties of the double plate system, namely

(a) Natural Frequency

(b) Damping

(c) Mode Shapes

(d) Modal Mass

(e) Modal Stiffness

An excellent survey of system identificaiton techniques is given in Ref. 39. The particular procedure used in the identification of the modal parameters of the double plate system is detailed in Chapter V.

The transmissibility function is used to evaluate the effect of the glazing retaining the double glass plate in the supports. Comparison of theoretical and measured acceleration transmissibilities will provide an estimate of the reduction in support acceleration and thus forces caused by the neoprene gasket.

The Research Objectives

With the above background, the research objectives can now be stated. The experimental and analytical studies were planned to meet the following:

1. Characterization of wind loads using Eqs.(25) and (26) as the basis.

2. Assessment of degree of dependence of window response on direct wind loads.

3. Formulation of a simple analytical model of the double plate system and its solution to obtain the natural frequencies.

4. Identification of the modal parameters of the double plate system.

5. Estimation of the glass plate to support (mullion) transmissibility function.

In concluding this chapter, it should be pointed out that the application of linear system theory to practical measurement problems falls in the realm of Time Series Analysis. These procedures are elaborated on in the following chapter.

CHAPTER III

THE EXPERIMENTAL METHODOLOGY

Introduction

Successful completion of the field study outlined before required that the design of the measurement system and the logistics of data acquisition in periods of strong wind be given careful consideration. In addition, suitable techniques and streamlined procedures were required for the rapid sorting and analysis of the large volume of test data.

In this chapter the test site used and the instrumentation employed are described. The test procedures and data processing techniques are outlined. Finally, digital computation requirements for analysis of the time series of data are presented.

The Test Site

The structure selected is a 29-story steel frame medium high-rise building of modern design. 'Tower Place' is an office building located some six miles north of the downtown Atlanta area on the crest of a ridge and one-half mile from the nearest comparable building to the northeast. The lightweight exterior curtain wall makes extensive use of aluminum extrusions in its design. The cladding consists of large (100 in. x 57 in.) doubly glazed windows incorporating a heat reflecting exterior light and smaller singly glazed spandrel panels. A view of the building just after completion is shown in Fig. 10, and details of the mullion and glazing are shown in Fig. 11.

Figure 10. Tower Place, Atlanta; A View from the South East Relative to the Building Axis.

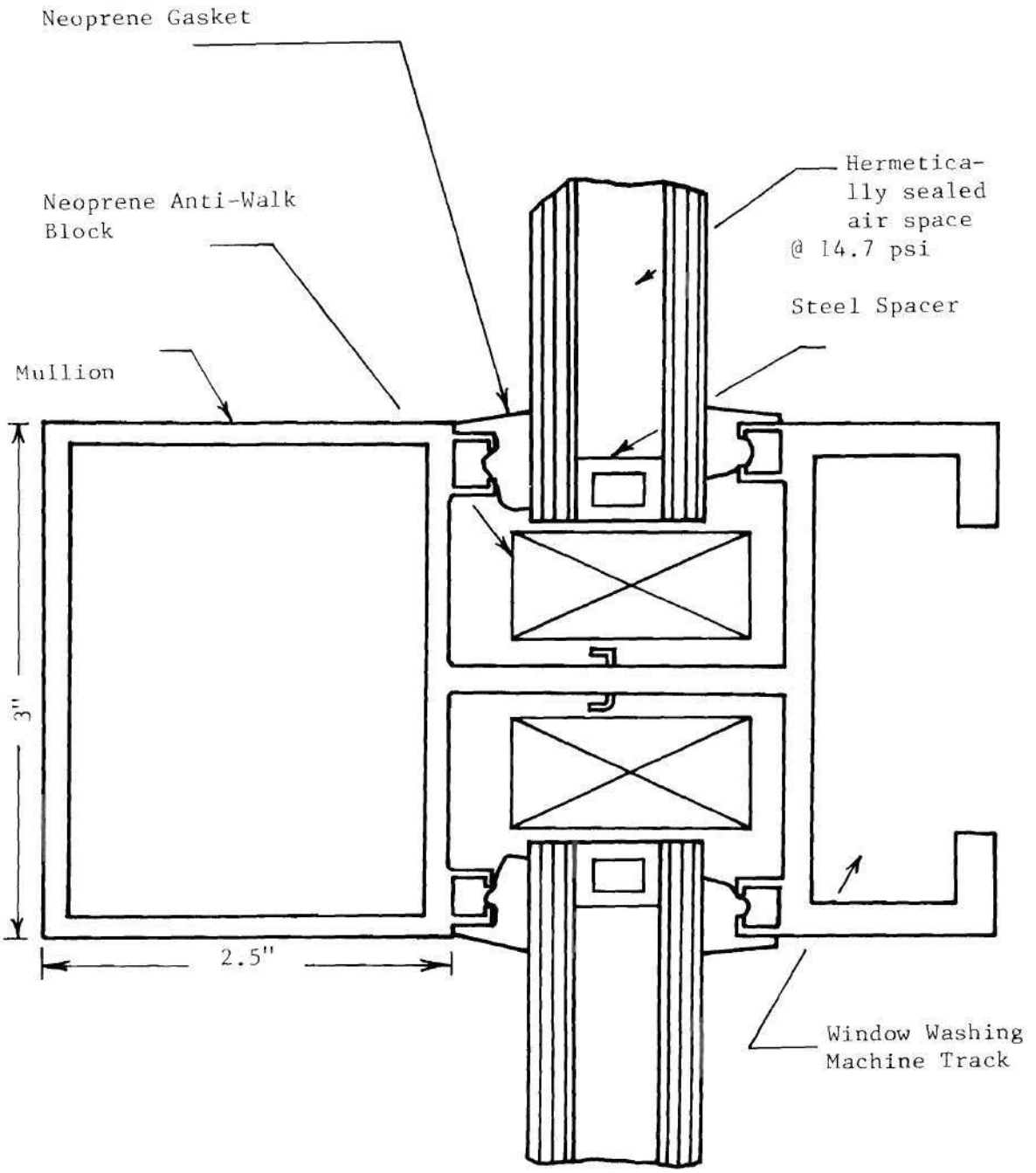

Figure 11. Mullion and Glazing Detail.

The 400 ft. tall structure is essentially prismatic with a planform that includes twelve exterior right corners at the base. The geometry is modified for the upper twelve floors to provide twenty and thirty-six corner floor plans, Fig. 12. In the aerodynamic sense, the building presents profiles to the wind which change with height. The architectural features contribute to a striking design, and provide the large number of corners suited to the present investigation.

The prevailing wind direction for the Atlanta area is the northwest. The exposure of the building to prevailing winds can be described as heavily forested relatively flat region of residential construction. The terrain in other directions with respect to the building can be similarly described with surrounding low rise buildings 3-4 stories high. The exposure conditions dictate the vertical velocity profile of the mean wind boundary layer. The profile can be approximated by the relation

$$\frac{v}{v_o} = \left\{\frac{z}{z_o}\right\}^{1/n} \tag{28}$$

where v_o is the measured wind speed at height z_o, and v the velocity at a height z. The exponent n depends on the aerodynamic roughness of the surrounding terrain and in accordance with Ref. 40, the following relationships apply:

Terrain	1/n
Open Sea	0.1
Flat Open Country	0.16
Wooded Forest	0.28
Urban Area	0.40

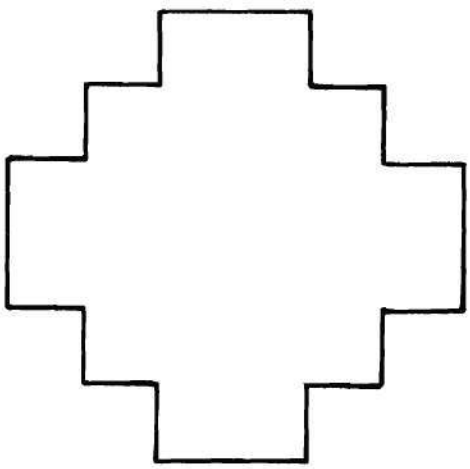

(a) Floors 1 thru 17

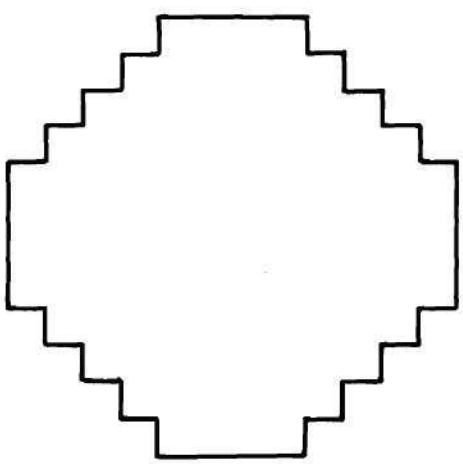

(b) Floors 18 thru 24

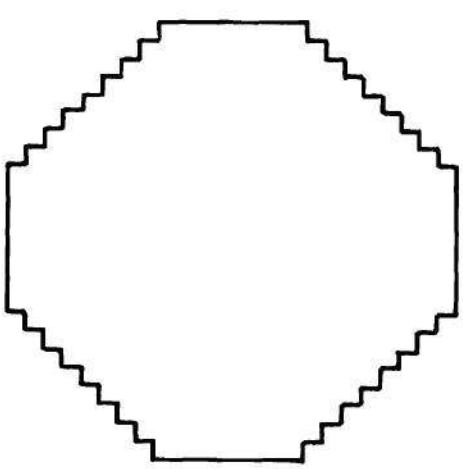

(c) Floors 25 thru 29

Figure 12. Floor Plans

The velocity profile for the wooded area surrounding Tower Place can be approximated by:

$$\frac{v}{v_o} = \left\{\frac{z}{z_o}\right\}^{0.28} \tag{29}$$

Instrumentation

The experimental plan called for the measurement, at various locations throughout the building, of cladding loads and the response of the two glass plates and the mullion to these loads. In addition, the reference wind velocity and direction were also required. The inaccessibility of the outdoor light from within the building required that a method for measuring its response without direct contact be devised. The design of such a transducer and its successful implementation is a noteworthy accomplishment of this research. Conventional transducers with suitable performance specifications were chosen for the measurement of the other variables. The instrumentation and its integration into a portable system is described below.

Wind Loading

The pressure loading on a window is assumed at the outset to be uniform over the area. The assumption although at first seemingly crude, is realistic since the window area is relatively small compared to the building facade and, therefore, sudden spatial variations of pressure over this area are not expected. With this assumption the wind loading

on a window can be measured from the difference in the external and internal pressure provided the internal pressure is known.

Internal pressure variation due to the normal building activity, such as opening and closing of doors, operation of elevators and mechanical services of the building does not permit its use as a reference pressure. The ideal reference pressure would give a zero output for a transducer when the wind speed was zero. In comparing full scale measurements with wind tunnel tests, various methods of referencing the wind pressure have been proposed, including most recently, the use of absolute pressure transducers [41, 42]. However, since the cladding loads are simply the differential pressure between the inside and the outside, no reference pressure is required in the present measurements. The differential pressure transducers used were Datametrics Type 501-11 Barocels. These pressure sensors are variable capacitance types with an internal volume of 0.15 cu. in. Datametrics Types 1014 and 1015 signal conditioners were used with the Barocels. Use of the auto-ranging Type 1015 manometers was made to ensure that the pressure signals were not clipped in strong squalls, and were useful in providing an adequate dynamic range.

With the uniform pressure assumption a single point pressure measurement can provide a measure of the loads on a window. A pressure tap through the mullion was planned initially but the channel shaped mullion exterior was anticipated to cause upflow interference effects. The pressure tap was ultimately located on the muntin (horizontal top support) of the window, flush with the exterior of the muntin. The other

port of the Barocel was vented inside. The external pressure tap and its location are shown in Fig. 13.

The use of the sensor in dynamic pressure measurements required that the length of tubing used for the external pressure tap be selected to ensure adequate dynamic response. A suitable length was chosen after considering the resonance effects and damping in the system, and hardware limitations. Details of the response estimate are given in Appendix B. A value of $L \simeq 18$ in. gave a flat response bandwidth of ~ 38 Hz with phase linearity up to ~ 22 Hz. The bandwidth was considered suitable for pressure measurements (auto spectra) and the range of phase linearity adequate to span at least two structural response modes.

Reference Wind Velocity and Direction

The reference wind speed and direction were measured with an MRI Model 1022 Wind Sensor. The speed sensor has a range of 0.5-80 mph. To obtain reasonably undisturbed measurements of wind speed and direction, the anemometer was mounted on an 'open' antenna tower at a height of approximately 455 ft. above the ground level. Due to the existence of an atmospheric boundary layer compounded by interference effects due to the building, the velocity measured is not that of the mean wind. If the building interference effects are ignored, however, velocities at any other height can be obtained by using Eq.(29) applicable to the terrain conditions in the vicinity of Tower Place.

The wind speed and direction were recorded on strip chart recorders and the records used to compute the mean wind speed and direction over a certain length of time.

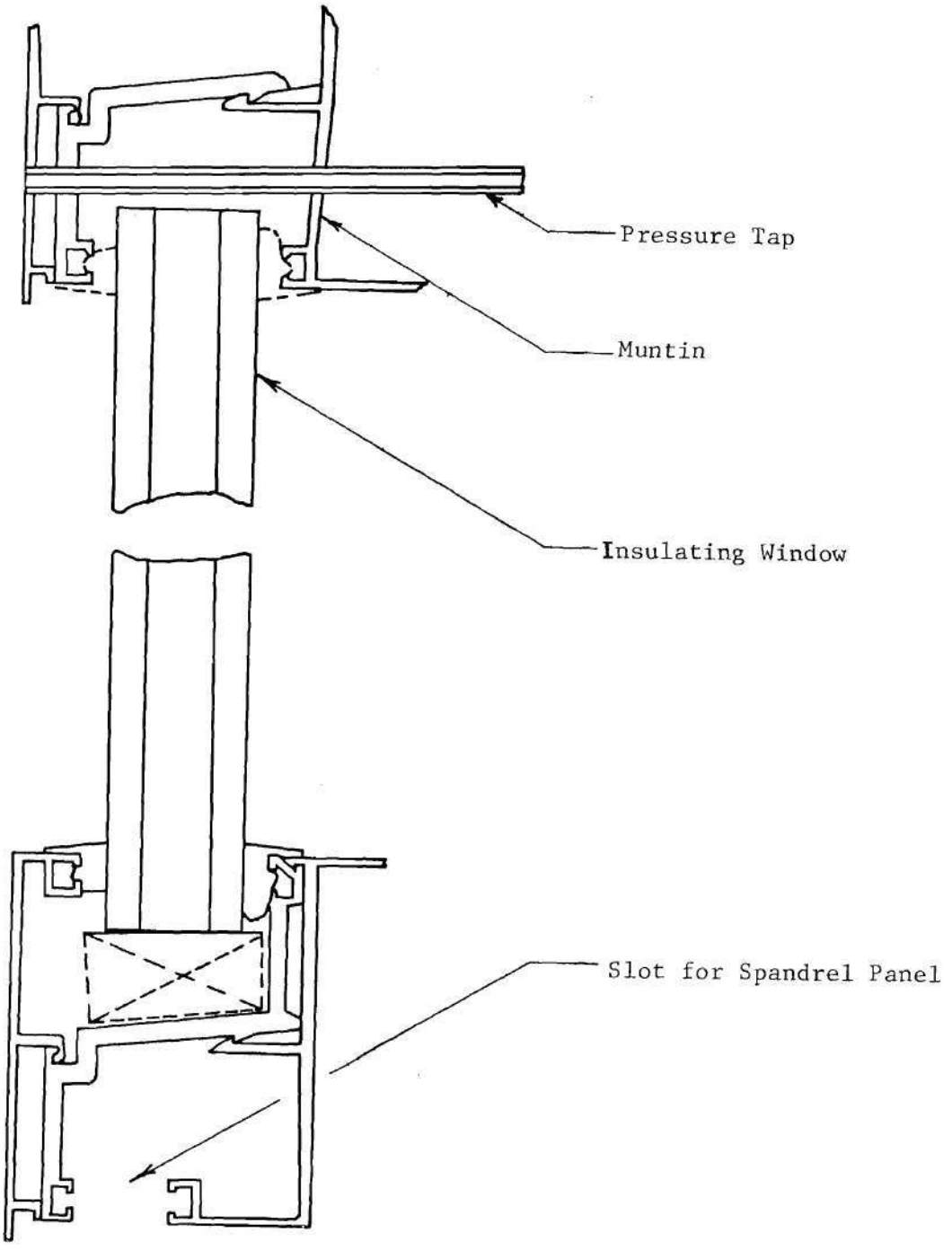

Figure 13. Pressure Tap and its Location.

Response Measurement

The primary response parameters for the window glass were single point transverse surface displacements, w_i and w_e, of the inner and outer panes, respectively, and mullion acceleration a_m.

The inner glass displacement, w_i, was measured by a linear variable differential transformer (LVDT) mounted in a fixture referenced to the building structure. The LVDT core was flexure-mounted so as to enable it to follow the glass displacement. The range was 0.1 in. and was considered adequate to measure the displacements due to the ambient wind load. To avoid the nonlinearities around the null of the transducer and to keep the core in contact with the glass for inward as well as outward motion, the LVDT housing was positioned so as to preload the core. The carrier frequency of the LVDT of 9 KHz permitted adequate dynamic response (1/10 fc).

The mullion acceleration was measured using an MB accelerometer. The piezoelectric accelerometer could not be used for frequencies below 5 Hz although the upper limit of the bandwidth was quite large. However, for transmissibility measurements in the vicinity of resonance ($\sim$ 10 Hz, 1st mode) the dynamic response posed no serious limitations.

Measurement of w_e for a double glazed window is complicated by the inaccessibility of the outer pane to measurement by conventional transducers located inside the building. Therefore, a method for measuring w_e without direct contact was required. Some common contactless transducer designs utilize capacitive, inductive or optical effects. However, capacitive and inductive methods require treatment of the outer glass. Optical techniques, on the other hand, were judged most

promising and a variety of available optical displacement transducers were evaluated with respect to their performance and portability. However, some of these require relatively complex processing of the measured signals and others were found to be unsuitable since they have a limited range of measurands and are affected by the presence of background illumination. A unique transducer was, therefore, designed which provided simplicity of operation, sufficient range and accuracy, and a capability of integration into a portable measurement system.

The sensor operates on geometric optics and utilizes a He-Ne laser beam for a collimated light source. The geometric movement of a beam reflected off the outer glass pane is sensed by an array of linear semiconductor detectors. The detector output after conditioning by a set of preamplifiers and analog computing circuits produces voltages proportional to the motion and intensity of the beam. The design of the geometrical configuration of the laser-detector system and other details such as elimination of the effect of rotation in the vertical plane, and signal conditioning electronics is given in Appendix C.

The transducer is capable of measuring both transverse displacements, and rotation in a plane normal to the window. Based on the design considerations of Appendix C, the preamplifier outputs had to be algebraically manipulated to obtain voltage signals linearly related to the displacement, w_e, and rotation α. To accomplish this, a computing circuit utilizing integrated circuit operational amplifiers and function modules was designed.

Typical calibration curves and dependence of sensitivity on the geometrical configuration are shown in Appendix C. For the particular

configuration used in the measurement of w_e, the transverse displacement sensitivity was 6.25 V/in. The usable range of displacements was 0.35 in. before effects of detector differential nonlinearity and violation of small angle assumptions caused the output to deviate from the linear relation.

Physical construction of the transducer is best described by Fig. 14, where the laser and the detector enclosure box are shown mounted on a 4" x 4" steel beam supported by a torsionally rigid tripod. The laser displacement meter (LDM) support also served as the fixture for the LVDT which is partially visible. The Barocel sensor seen clamped to the beam was located on the top horizontal support during an actual run. Retractable wheels on the tripod permitted easy transport of the LDM/LVDT combination to various locations throughout the building. Figure 14 shows the displacement transducers positioned (by means of aluminum 'spacer' rods to ensure calibration) opposite a window to record displacement histories.

The LVDT and LDM were positioned to measure the transverse displacements at corresponding points on the two panes. The measurement point was at the centroid of the horizontal axis and approximately 5 in. below the centroid of the vertical axis. This arrangement is suitable for detecting motion in any symmetric modes of the window glass. To measure the displacement response of the plates in antisymmetric modes a position closer to the supports is desirable and could be used by repositioning the platform.

A schematic of the entire instrumentation is shown in Fig. 15. The LDM and LVDT outputs for a differential pressure transient observed

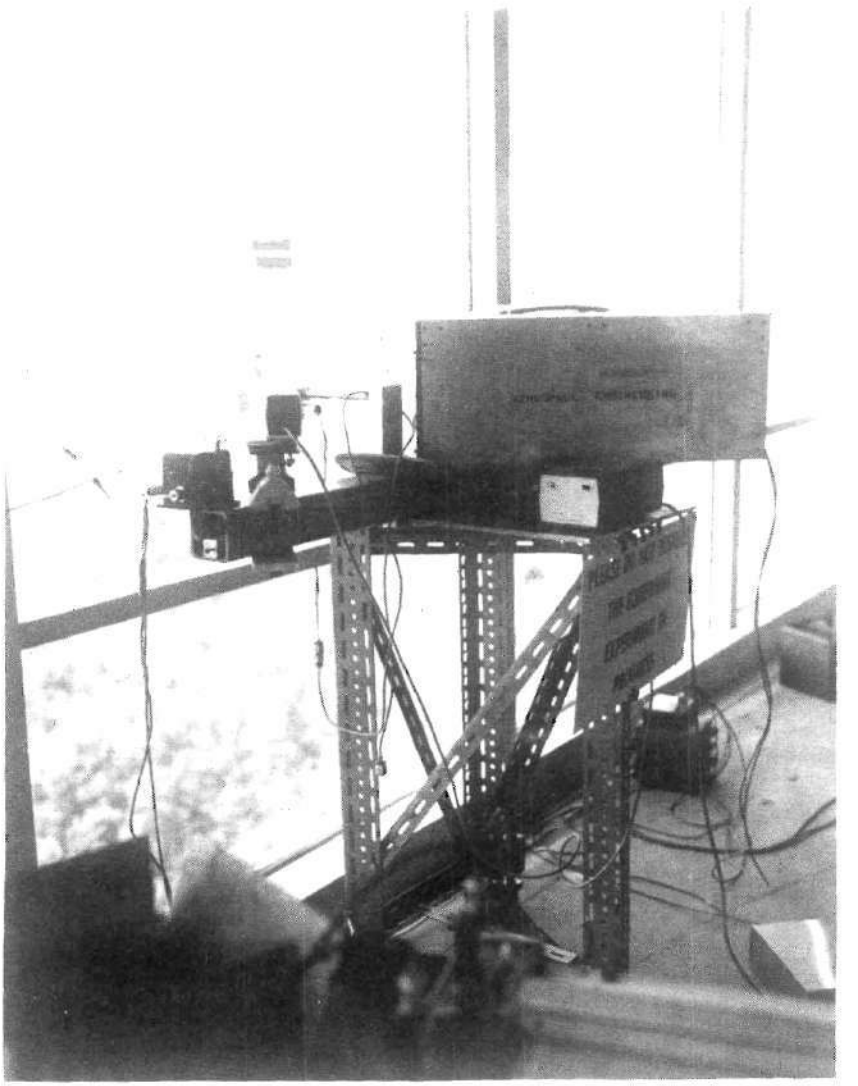

Figure 14. The Experimental Set Up.

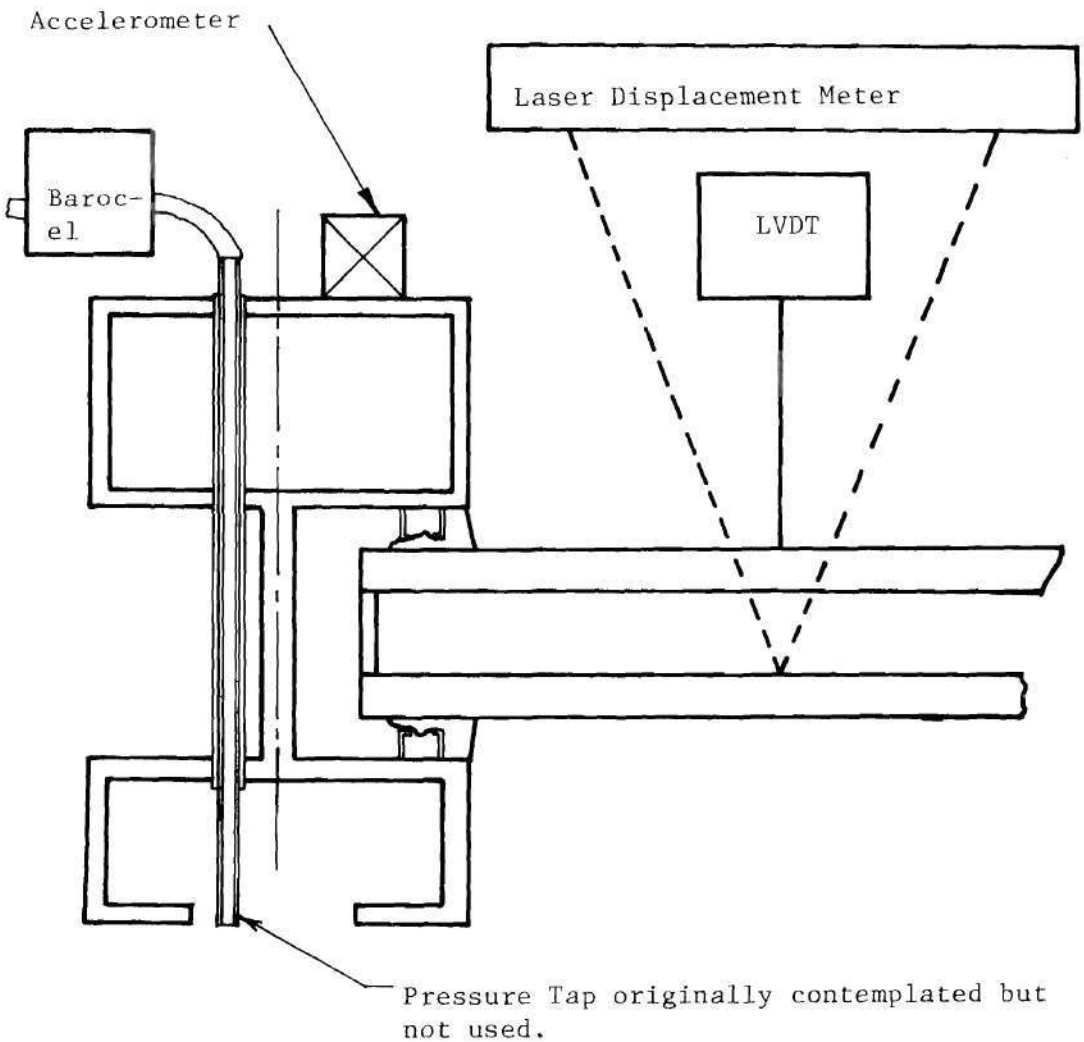

Figure 15. Schematic of the Instrumentation.

in one of the actual data records is shown in Fig. 16. A comparison of the power spectrum of the external plate response to an impulse (applied by an instrumented hammer to provide a wide-band input) as measured by the LDM with the internal plate response measured simultaneously by an accelerometer is shown in Fig. 17. This verified the performance of the LDM in measuring dynamic displacements.

Data Recording

The large quantities of data inherent in full scale investigations requires that careful consideration be given to a data acquisition system. Portability, unattended operation for several hours and compatibility of the system with the transducers is essential. While the use of a total digital recording system would have facilitated digital data analysis, the cost and lack of portability of such a system led to the choice of analog recording. For the present experiments the analog signals form all the transducers except the remotely located anemometer were recorded on a portable FM tape recorder (HP 3968A). Since the planned data analyses required only a mean wind speed and direction for a set of sample records from the response and load transducers, the use of strip chart recorders for the anemometers posed no serious problems. Data recording was continuous for a particular session and the records were sorted for relatively large pressure fluctuations prior to analysis.

Test Methodology

Weather forecasts were used to select days on which the experiments were run. The test sites for the measurements were selected on the

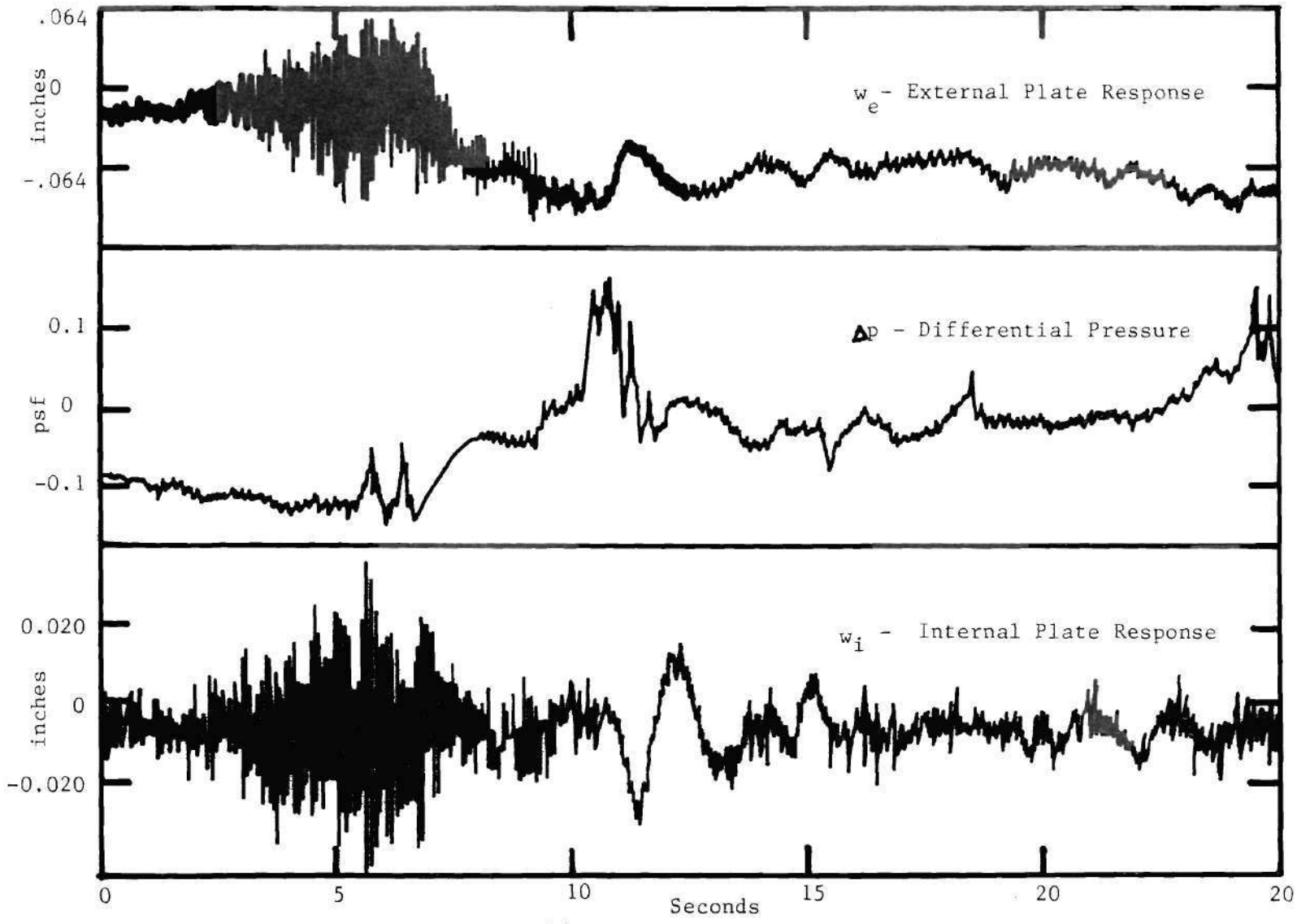

Figure 16. Pressure and Response Transients.

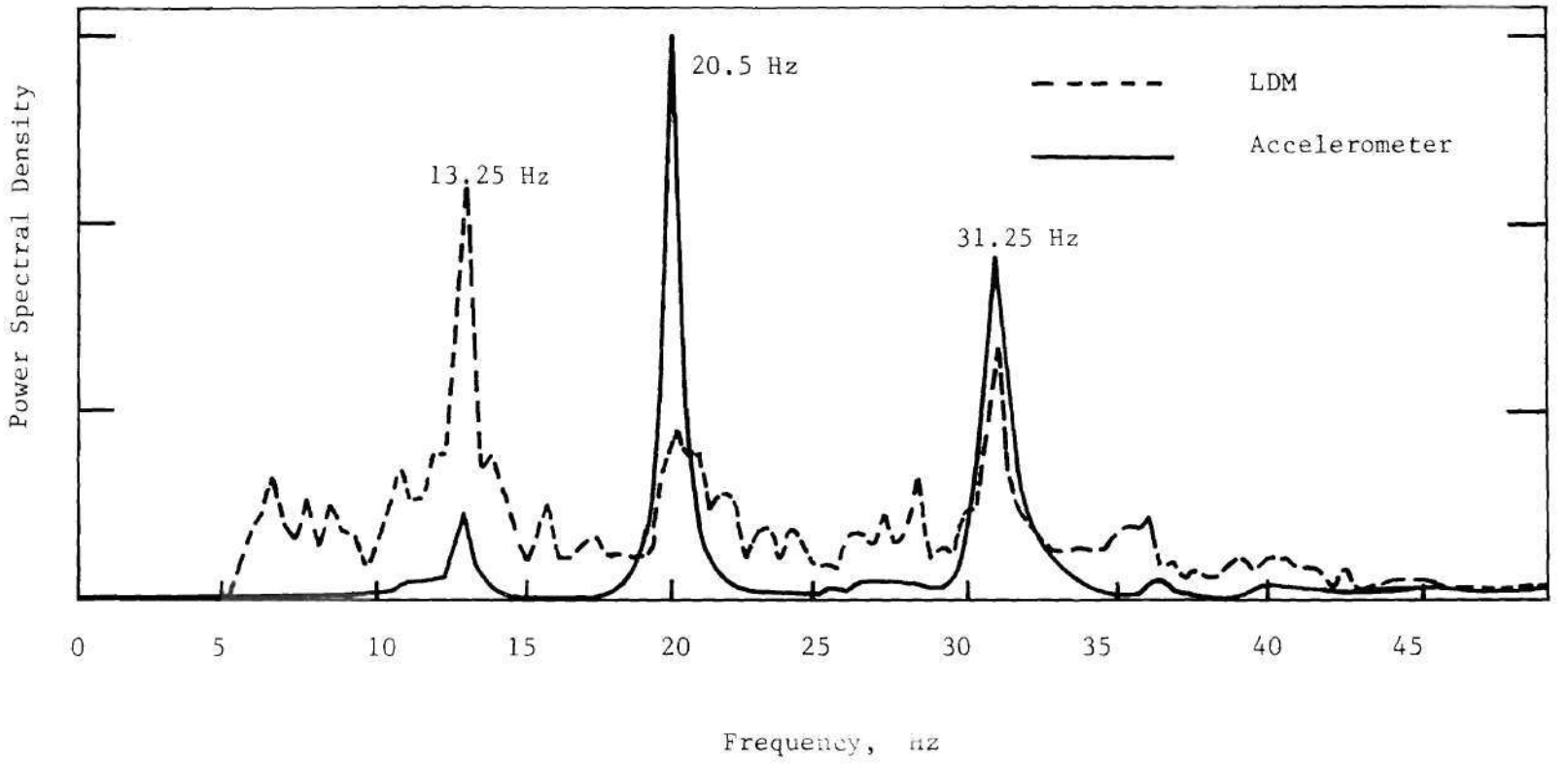

Figure 17. Comparison of Response Spectrum as Measured By the LDM With That From an Accelerometer.

basis of available wind tunnel pressure distribution data from an earlier simulation [43]. Windows were selected in areas where large negative pressure coefficients occurred in the simulation with the prevailing wind direction as the flow direction. In order to assess the variation of wind loads with height, tests were planned to include three different floors of the building, viz. 9th, 21st, and 28th. The window nomenclature used and the wind directions for which data were recorded are shown in Fig. 18.

On days when reasonable wind velocities were forecast (about 15-20 mph) the portable instrumentation system was set up at a suitable window, depending on the wind direction, and the data recorded. For unexpected storm systems moving into the area data acquisition was not possible due to the time required to get to the test site and make the measurement system operational. A summary of the acquired data is shown in Table 2. Recording sessions were usually unattended and on the average were conducted over periods of approximately six hours.

The major problem encountered in the data acquisition process was one of dynamic range of the transducers. The selection of transducer signal conditioner range was dictated by the extremes of adequate signal-to-noise ratio and avoidance of clipping of the high amplitudes. The range selected in the first hour or so of a run, therefore, in some cases was inadequate for the strong gusts that occurred later in the recording period. To overcome this problem for the pressure transducer, an autoranging signal conditioner was used. The signal conditioner automatically switched to a higher or lower range when a preset threshold was crossed and was accompanied by a switching pulse to indicate the change.

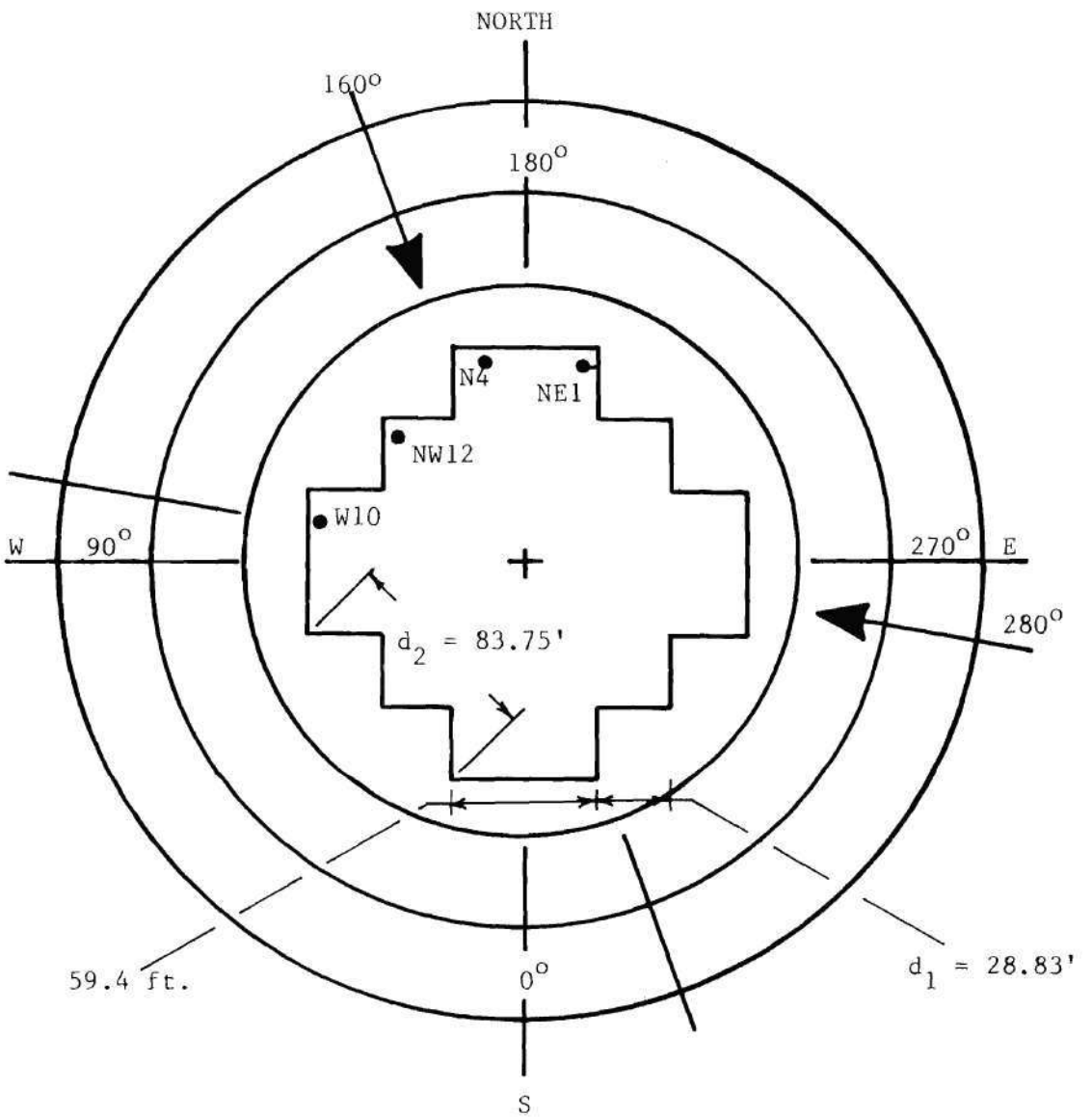

(a) 9th Floor

Figure 18. Window Nomenclature; Directions With Respect to Building Axis.

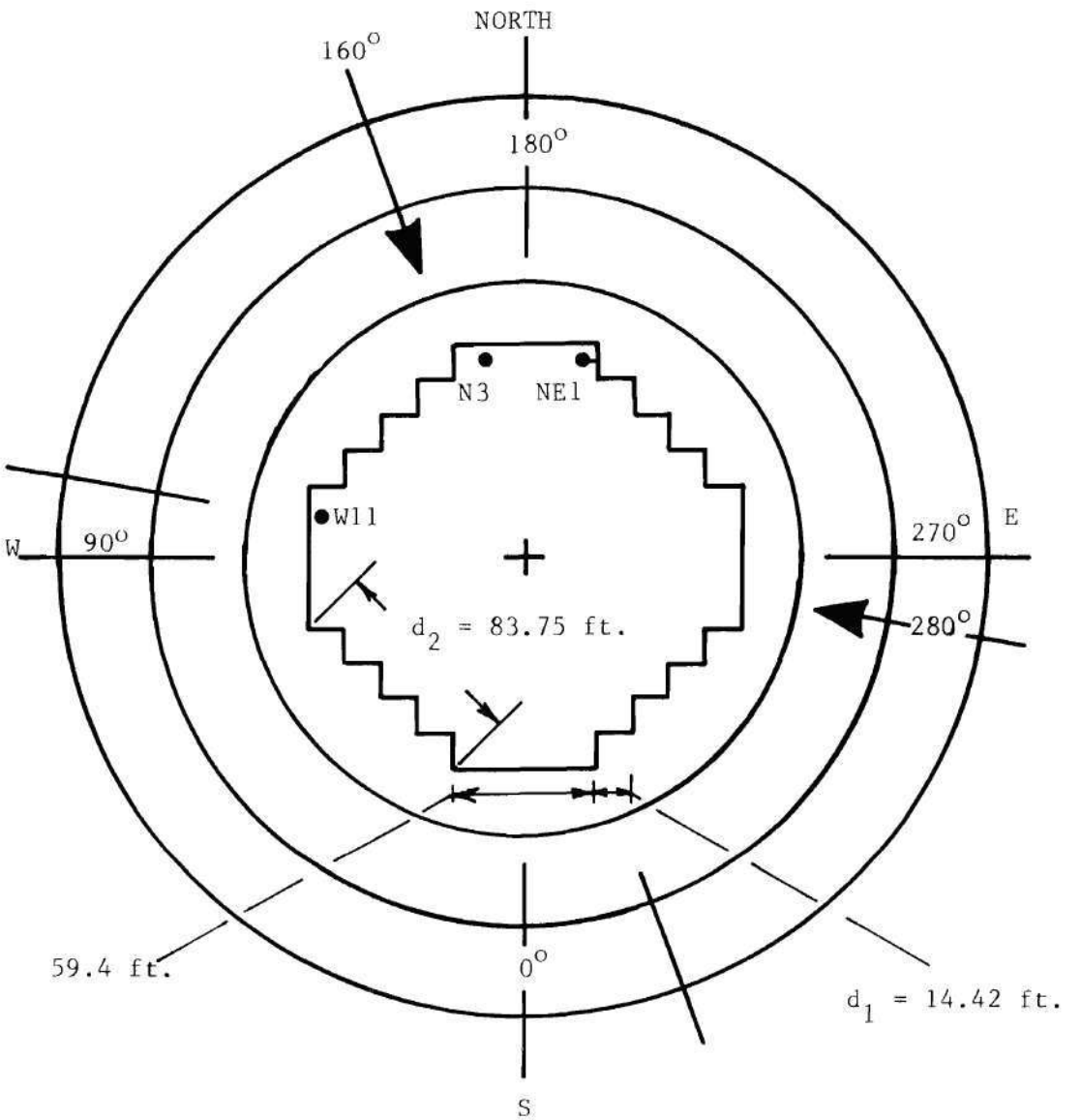

(b) 21st Floor

Figure 18(contd.). Window Nomenclature; Directions With Respect To Building Axis.

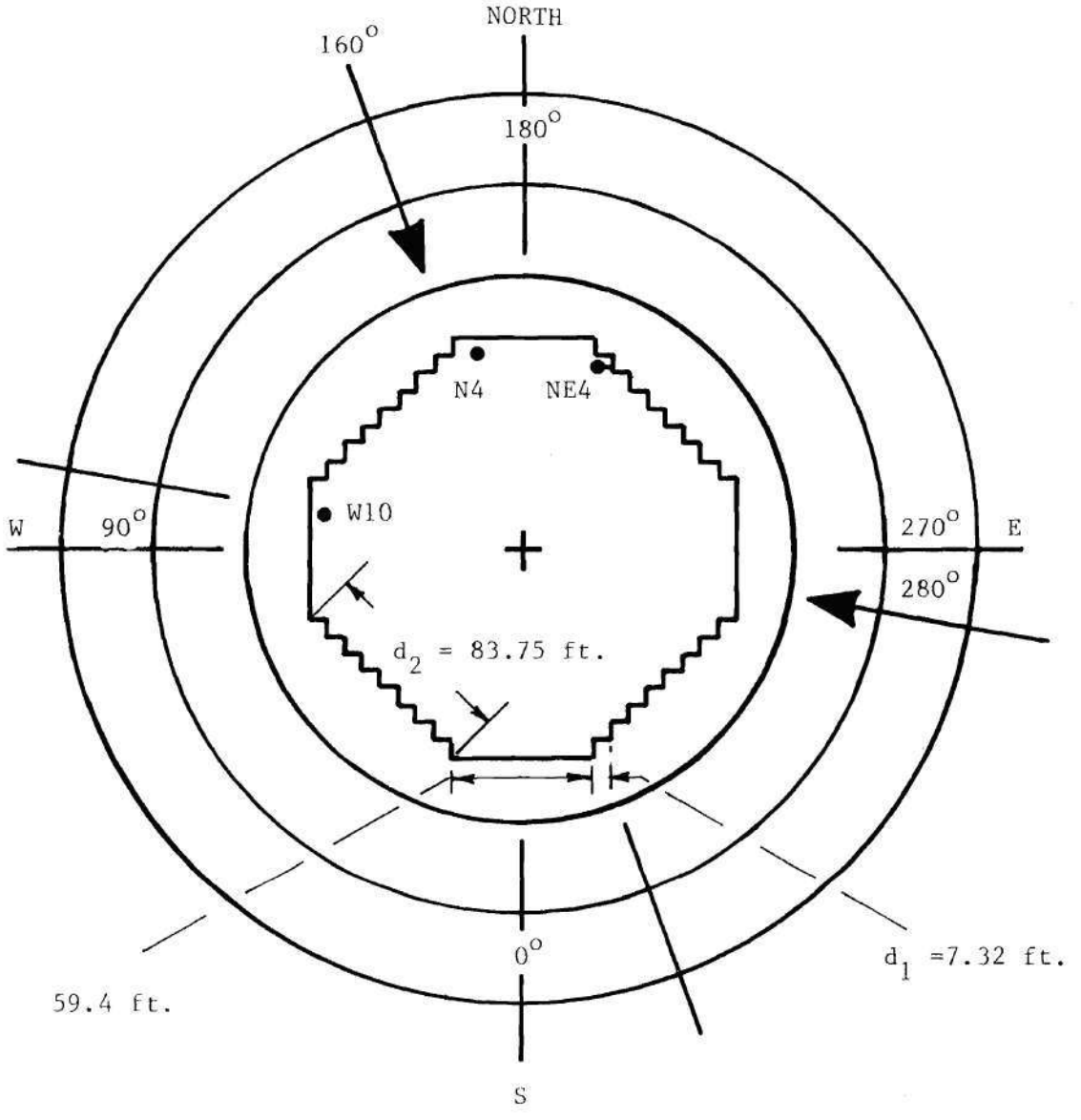

(c) 28th Floor

Figure 18(contd.). Window Nomenclature; Directions With Respect To Building Axis.

Table 2. Summary of the Data Collected

#	Date (1976)	Duration Start/# hrs	Window	fps $\bar{v}$	0° S $\bar{\theta}$	Transducers Used				
						Δp	Wext	Wint	Am	Δp mull
1	6-2	3:52pm/3	F28/W10	23	108°	x	x	x		x
2	6-5	2:35pm/4	F28/NE3	23	290°	x	x	x		x
3	6-6	2:52pm/6	F28/N10	18	270°	x	x	x	x	
4	6-7	5:43pm/3	F28/N4	15	281°	x	x	x	x	
5	6-15	2:45pm/6	F21/NE1	12	324°	x	x	x	x	
6	6-16	3:50pm/8	F21/W11	15	98°	x	x	x	x	
7	6-19	3:58pm/4	F21/NW19	12	72°	x	x	x	x	
8	7-16	12:30pm/5	F21/N3		194°	x	x	x		
9	7-16	8:09pm/6	F21/N3	15	108°	x	x	x		
10	8-2	2:55pm/3	F21/N3			x	x	x		
11	8-3	2:29pm/4	F21/NE1			x	x	x		
12	8-18	4:05pm/4	F21/N3,NE1	23	280°	x	x	x		
13	8-19	1:42pm/5	F9/N4,NE1,NW12	30	270°	x				
14	8-20	2:13pm/8	F9/N10,N4,NE1	15	270°	x	x	x		
15	9-10	1:38pm/5	F9/W10,N4,NE1	30	160°	x	x	x		
16	9-17	5:42pm/3	F21/NE1,N3,W10	18	160°	x				
17	9-21	6:20pm/8	F28/W10,N4,NE4	23	160°	x				
18	10-21	10:30pm/8	F9/N4,NW12,NW4	30	160°	x	x	x	x	

Use of the signal conditioner in this mode was not possible since the range switching was fairly rapid during a normal run. Its use, however, in an AUTO UP mode where the range was scaled upward only, proved feasible. In a typical run the starting range and that at the end of the run were recorded. The switching transients in the data were then used to associate the correct scales with the recorded segments.

Data Processing

The large quantities of inherently nondeterministic data that resulted from the experimental study required that the data processing techniques be fast and fairly streamlined. In recent years, the advent of high performance, low cost minicomputers, and the Fast Fourier Transform algorithm have made digital processing of time series of data attractive. The various frequency domain quantities in the transfer function description of linear system dynamics, can be rapidly computed using digital time series analysis procedures. Digital techniques also offer the advantages of ease of manipulating the processed results, and greater dynamic range. These considerations and the availability of a digital system, to be described later, dictated use of digital computation of the various auto and cross-power spectra from the experimental data.

The mathematical development of the frequency-domain input-output relations for a linear system dealt with exact values of the frequency-domain quantities. This means, in the case of random time series, that the spectra are based on time samples of data that are both infinite and continuous. In practice, of course, the sample lengths are finite and in

the case of digital analysis are further limited to discrete data values. The effect of truncating the data is that magnitude and phase information in the frequency domain is obtained only at discrete frequencies. The effect of sampling at discrete time increments is to limit the highest frequency at which valid information is obtained. In addition, to determine the descriptive properties of random time series from finite data, estimators, as for example the sample mean and the sample variance, for the various spectral quantities must be used. This means that only estimates of the properties of a random process can be obtained. Thus, it is necessary to recognize the uncertainty or statistical variation in the estimates and know the techniques to minimize this uncertainty.

Digitization of random analog data and estimation of their descriptive properties from finite samples, therefore, requires consideration of the following:

(a) Sampling at discrete time increments

(b) Effects of truncation of the random time series

(c) The Estimators used

(d) Statistical errors in the estimates

Practical implications of these aspects of digital time series analysis in computing the various frequency-domain quantities are briefly outlined in the following paragraphs.

Digitization of Analog Data

Digitizing analog data of duration T by sampling in the time domain with an interval Δt requires that the frequency spectrum be band limited to a frequency $\frac{1}{2\Delta t}$. This is a consequence of Shannon's sampling

theorem which states that it requires slightly more than two samples per period to uniquely define a sinusoid [44]. In terms of the time domain and frequency domain interrelationship this can be written as

$$F_{max} < \frac{1}{2\Delta t} \tag{30}$$

where, F_{max} is the highest frequency present in the spectrum. The sampling rate $F_s = \frac{1}{\Delta t}$ determines a Nyquist folding frequency $f_N = 2F_s$. Frequencies in the spectrum which are greater than f_N are seen as replicas of frequencies in the base band $(0 - f_N)$ e.g. $f_N + f_i$ will be seen as $f_N - f_i$ [45]. This folding back of frequencies is known as aliasing, and the "image" frequencies cannot be distinguished from the true baseband spectrum. In practice aliasing can be avoided by low pass filtering the data with a cut-off frequency slightly less than f_N. The total number of samples $N = T/\Delta t$. In digital computation N is frequently referred to as the block size.

Effects of Truncation

Sampling the data over only a finite duration T results in discretization of the frequency domain i.e. the Fourier transform of the sample can be calculated only at a finite number of frequencies spaced $\Delta f = \frac{1}{T}$ apart. The frequency resolution Δf is related to the Nyquist frequency f_N and the total number of discrete values N in the time domain as follows:

$$\Delta f = \frac{f_N}{N/2} \tag{31}$$

This is because N discrete values in the time domain allow computation of frequency and phase information in the frequency domain at N/2 points. Theoretically, discretization of the data in the frequency domain at intervals of $\Delta f = \frac{1}{T}$ is equivalent to assuming the data to be periodic, i.e. the sampled segment repeats itself with a period T.

Truncation of a random time series is mathematically equivalent to multiplication of the data by the boxcar function shown in Fig. 19, and expressed as:

$$\begin{aligned} u(t) &= 1 \qquad 0 \leq t \leq T \\ &= 0 \qquad \text{Otherwise} \end{aligned} \tag{32}$$

The data are then said to have been viewed through a rectangular window of width T. The Fourier transform of the rectangular window also known as its line shape function is:

$$U(f) = \frac{\text{Sin } \pi f T}{\pi f} \tag{33}$$

Computation of Fourier transform of a finite data sample, therefore, is equivalent to taking the Fourier transform of the product of an infinite data record and the time window. The result in the frequency domain is the convolution of the transform of the record of infinite length with the transform of the time window. For example, if $G_{xx}(f)$ denotes the true power spectrum of a stationary time series $x(t)$ and $\tilde{G}_{xx}(f)$ the net result of convolution with the time window transform, then

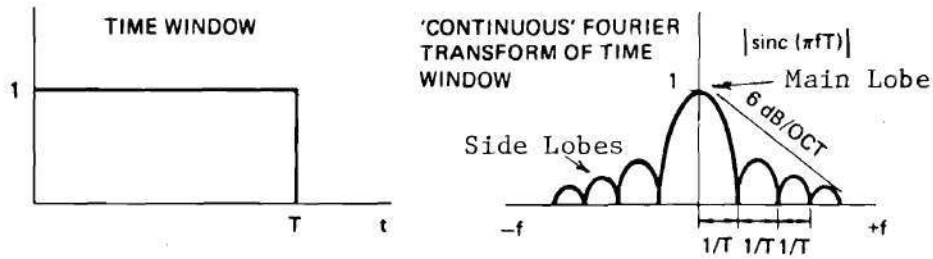

Figure 19. Boxcar Function and Its Fourier Transform.

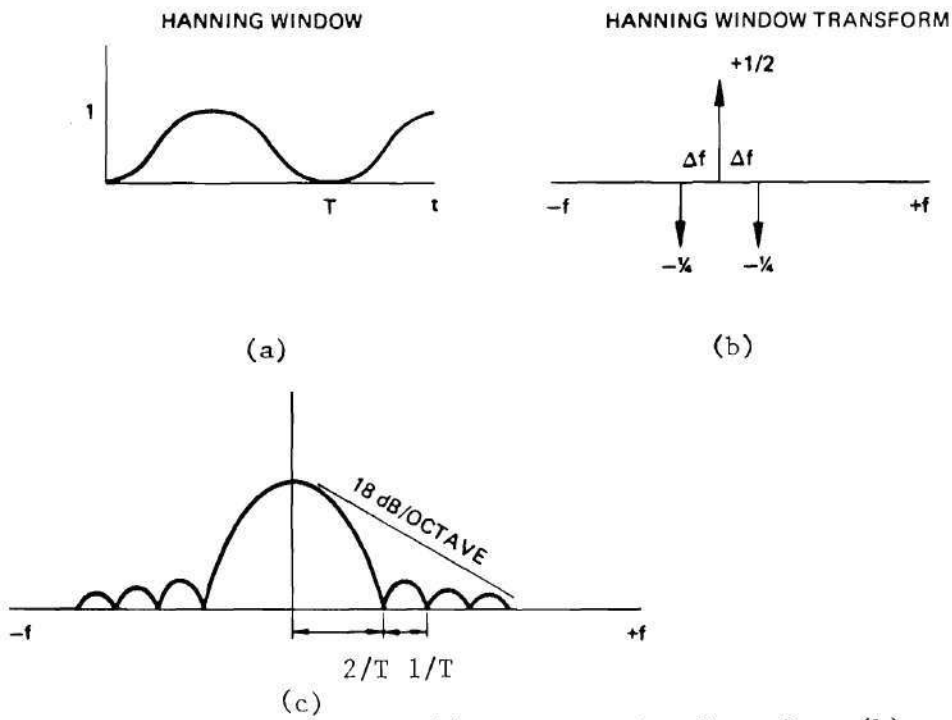

Figure 20. Hanning Window (a), its Fourier Transform (b), and its Convolution With The Boxcar Function(c).

$$\tilde{G}_{xx}(f) = \int_{o}^{\infty} G_{xx}(\alpha) U_T(f-\alpha)\, d\alpha \tag{34}$$

Thus, the true spectrum is "smeared" by the window line shape. This convolution is effected before quantization along the frequency axis. Thus, if the original data are periodic such that there is an integer number of periods in the time window, the line shape does not appear in $\tilde{G}_{xx}(f)$ because frequency samples occur only at zero crossings of $U_T(f)$. However, if there is an odd number of half cycles in the time window, frequency samples occur at the peaks of $U_T(f)$ and a single frequency waveform may transform into a broad band of frequencies. This phenomenon is known as frequency leakage and the cure is to reshape the time window to produce a line shape with smaller side lobes (see definition of terms in Fig. 19). This technique will broaden the main lobe and hence reduce frequency resolution, but it reduces the interference of one frequency with its neighbors.

The selection of a time weighting function to reshape the rectangular window transform and thus suppress leakage reduces to a study of the various windows and their line shapes. A number of weighting functions, also called windows, and their line shapes are described in Refs. 31, 44, 45, and 46. For the present application the Hanning window of Fig. 20 described by

$$\begin{aligned} w_H(t) &= 0.5\left(\text{Cos}\ \frac{2\pi t}{T} - 1\right) \\ W_H(f) &= 0.5\delta(0) - 0.25\delta(\Delta f) \end{aligned} \tag{35}$$

was used. The Hanning window is attractive due to its relatively narrow

main lobe together with greatly reduced amplitude of the side lobes [47].

Digital Computation Requirements

The descriptive properties of a random process $\{x(t)\}$ cannot be precisely determined from sample data. Therefore, suitably defined estimators have to be used in computing the spectral density, transfer, and coherence functions from finite samples of data. The raw estimates (denoted by superior carets) thus obtained require smoothing operations to reduce the statistical uncertainty in the estimates. The smoothed quantities are denoted by superior tildes.

The accuracy of parameter estimates based on sample values can be described by a mean square error defined as [31]:

$$\text{Mean Square Error} = E[(\hat{\phi} - \phi)^2] \tag{36}$$

where, $\hat{\phi}$ is an estimator of ϕ and E is the expectation operator. The root mean square can also be expressed as

$$\text{rms error} = \sqrt{\sigma^2[\hat{\phi}] + b^2[\hat{\phi}]} \tag{37}$$

or, the normalized random error $\epsilon = \sqrt{\epsilon_r^2 + \epsilon_b^2} = \dfrac{\sqrt{\sigma^2[\hat{\phi}] + b^2[\hat{\phi}]}}{\phi}$

where, $b[\hat{\phi}]$ is the bias error in the estimate and $\sigma[\hat{\phi}]$ is the standard deviation of the estimate and where $\epsilon_r = \dfrac{\sigma[\hat{\phi}]}{\phi}$ is called the normalized random error and is a measure of the variance of the estimate. $\epsilon_b = \dfrac{b[\hat{\phi}]}{\phi}$ on the other hand is a measure of the bias of the estimate and is called the normalized bias error. An estimator with a small

random error is said to have high stability and that with a small bias error is said to reproduce the true function with high fidelity.

Estimates of power spectral density functions from digital data can be obtained by one of the following two methods [31]:

1. Blackman - Tukey Method

The power spectral density function is computed by first estimating the autocorrelation function and then Fourier transforming it, i.e. by using the Wiener-Khintchin relations of Eq. (18).

2. Cooley - Tukey Method

This is based on computing the discrete finite Fourier transform, via the FFT, of the original data.

Considerations of wrap-around error in evaluating the autocorrelation function from the finite sample and the computational speed advantage of the direct FFT make the second method more attractive. The Cooley-Tukey method was used in the present study to compute the various spectra. In this method, raw estimates of the spectral density functions are computed as follows:

$$\begin{aligned} \hat{G}_{xx}(k\Delta f) &= \frac{2}{T}\left|X(k\Delta f)\right|^2 = \frac{2}{T}\,X(k\Delta f).X^*(k\Delta f) \\ \hat{G}_{xy}(k\Delta f) &= \frac{2}{T}\,X^*(k\Delta f)\;Y(k\Delta f) \end{aligned} \tag{38}$$

where, $X(k\Delta f)$ and $Y(k\Delta f)$ are discrete Fourier transforms of stationary, Gaussian, zero-mean random processes $\{x(t)\}$ and $\{y(t)\}$ respectively. The index k is an integer and $*$ denotes the complex conjugate.

The estimator $\hat{G}$ of Eq. (38) can be shown to be a χ^2_2 random variable and has a substantial random error [31]. In practice the random error of an estimate produced by Eq. (38) is reduced by smoothing over an ensemble (averaging) or by smoothing over frequency. The averaging technique was used in the present application and consists of dividing a record of length T_S into n_d disjoint segments such that $T_S = n_d T$ and $T = N\Delta t$ where N is the number of values in each data segment. Individual estimates are computed for each of the n_d disjoint segments and the smoothed estimate $\tilde{G}$ obtained by averaging these. The normalized (with respect to the expected value) random error for smoothed estimates is given by

$$\varepsilon_r[\tilde{G}(f)] = \sqrt{\frac{1}{n_d}} = \sqrt{\frac{1}{\Delta f . T_S}} \tag{39}$$

The bias error $b[\tilde{G}(f)]$ is proportional to $\Delta f^2 = \left(\frac{1}{T}\right)^2$. Hence, T should be made as large as possible to minimize bias at the same time $n_d = \frac{T_S}{T}$ should be large to reduce the random error. Thus, reduction of bias and random errors imposes conflicting requirements on the data analysis parameters.

The overall level or mean square value estimates can be readily obtained from the power spectra by using Parseval's theorem which can be stated as follows:

$$\text{Let} \quad \Psi_x^2 = \lim_{T\to\infty} \frac{1}{T} \int_0^T x^2(t)dt$$

be the true mean square value of $x(t)$, then Ψ_x^2 can also be expressed as:

$$\Psi_x^2 = \int_0^\infty G_{xx}(f)df \tag{40}$$

The implication of Parseval's theorem is that the mean square value of a signal is the area under its power spectrum. Alternatively, the area under the power spectrum in a frequency band $(f, f+\Delta f)$ is the mean square value of the signal in that frequency band. This provides the basis for analog computation of the power spectral density function by filtering and squaring.

The mean square value can be estimated from the spectral density as

$$\hat{\Psi}_x^2 = 2 \sum_{k=1}^{N/2} \tilde{G}_{xx}(k\Delta f) \tag{41}$$

The errors in the estimate $\hat{\Psi}_x$ depend on the errors in the smoothed estimates $\tilde{G}_{xx}(f)$. It can be shown [35] that relatively large errors in power spectrum estimates will have relatively small errors for $\hat{\Psi}_x^2$ when N is sufficiently large.

Coherence function estimates can be obtained from two sample time history records of $\{x(t)\}$ and $\{y(t)\}$, assuming the sample records to exist over a common time interval T, as:

$$\hat{\gamma}_{xy}^2(f) = \frac{\left|\tilde{G}_{xy}(f)\right|^2}{\tilde{G}_{xx}(f)\tilde{G}_{yy}(f)} \tag{42}$$

The statistical accuracy of the estimate $\hat{\gamma}^2_{xy}(f)$ depends on the estimation procedure of Eq. (42) as well as the accuracy of the power spectral density estimates. Empirical studies of Ref. 48 show that estimates of the coherence function in the range of $0.35 \leqq \gamma^2_{xy} \leqq 0.95$ based upon spectral density estimates with $n_d \geq 20$ can be evaluated in terms of the transformation

$$\hat{w}(f) = \tanh^{-1}\left\{\hat{\gamma}_{xy}(f)\right\} \tag{43}$$

In terms of n_d, the number of disjoint independent segments, the bias and variance errors are given by

$$\begin{aligned} b[\hat{w}(f)] &\simeq \frac{1}{2n_d - 2} \\ \sigma[\hat{w}(f)] &\simeq \frac{1}{2n_d - 2} \end{aligned} \tag{44}$$

The frequency response function estimate for a single input-single output CPLS with transfer function $H(f)$ input $\{x(t)\}$ and output $\{y(t)\}$ is obtained as:

$$\hat{H}(f) = \frac{\tilde{G}_{xy}(f)}{\tilde{G}_{xx}(f)} = \left|\hat{H}(f)\right| e^{-j\hat{\varphi}(f)} \tag{45}$$

The bias and random errors in the estimate of Eq. (45) are shown in Ref. 31 to depend on the number of degrees of freedom $n = 2n_d$ of the spectral density function estimates and the coherence function estimate $\hat{\gamma}^2_{xy}(f)$. The bias error is generally less than the random error for any

given combination of n and $\hat{\gamma}^2_{xy}(f)$. The random error of $\hat{H}(f) \to 0$ as either $n \to \infty$ or $\hat{\gamma}^2_{xy}(f) \to 1$. In interpreting practical measurements if $\hat{\gamma}^2_{xy}(f) \approx \gamma^2_{xy}(f) = 0$, it follows that no physical system exists between the measurement points and no frequency response function can be defined. On the other hand, if $\gamma^2_{xy}(f)$ has a nonzero value, no matter how small, then a frequency response function can be estimated with any desired degree of accuracy given sufficient data to make n appropriately large. Thus, $\hat{\gamma}^2_{xy}(f)$ is an indicator of the validity of the frequency response function.

The Digital Processor

For computation of power spectra, transfer and coherence functions and amplitude histograms by digital techniques, a minicomputer based Fourier Analyzer (HP 5451B) was used. The main features of the Fourier Analyzer are a 2 channel, 12 bit analog-to-digital converter which accepts analog data to 25 kHz, and a dedicated minicomputer (32k core). Time-domain and frequency domain computations are performed in accordance with instructions from a keyboard. Simultaneous two channel operations are possible and the results can be recorded on a x-y plotter or punched on paper tape. "Quick Look" data inspection is possible on a CRT display, an integral part of the unit.

CHAPTER IV

A PARAMETRIC ANALYSIS OF THE WIND LOADS

Introduction

In Chapter II, functional forms for the wind load characteristics, namely the reduced power spectral density, the mean and the rms pressure coefficients, were hypothesized, Eqs.(25) and (26). The differential pressure measurements were, therefore, conducted to examine the effects of changes in the independent variables on the wind loads.

It can be anticipated that determination of the exact functional forms of Eqs.(25) and (26) by field tests on an actual structure is a practical impossibility. Rather, in the present case, data from sites preselected on the basis of wind tunnel tests and from the viewpoint of susceptibility to dynamic loads are analyzed. The objective is to assess the severity of dynamic loading and describe in a qualitative fashion the dependence of the load properties at these sites on the various profile and flow parameters. The results of such an analysis can then be used to predict a "critical" combination of the independent variables which could give rise to dynamic wind loads at a particular site.

In this chapter, the results of a parametric analysis of the pressure records are presented and discussed. Before proceeding with the analyses of the data, however, certain preprocessing operations were required. The large volume of data (close to 100 hours, real time) necessitated selection of segments from the analog records where, for

example, significant pressure fluctuations were observed. Error considerations in the estimation of the spectra required that the spectral analysis parameters be suitably chosen. In the following sections, the data sorting procedures used, and design of the spectral analysis are described.

Data Sorting

The differential pressure and the response in a particular run are recorded over a span of a few hours. In this interval, periods of calm where the wind speeds are so low as to produce insignificant cladding loads are expected and were observed in the recorded data. Unless the winds are due to a storm system passing through the area, the periods of calm can be of long duration. Therefore, selection of those segments of pressure and response signals where the signal amplitudes are high is necessary to ensure a high signal-to-noise ratio.

This sorting process may, of course, be obviated if the recorder were "kicked on" when, for example, the reference wind velocity crossed a certain threshold. There are, however, several drawbacks to this mode of data acquisition, viz:

1. The recorder takes some time (of the order of 3 secs.) to reach the correct recording speed, during which a significant part of the data may be lost.

2. The triggering process may introduce nonstationarity in the mean square value.

3. Due to the 3-dimensional nature of the flow around the building, the wind speed measured at the remotely located anemometer may not be indicative of the local activity.

In the present investigation the data segments to be analyzed were selected on the basis of the wind speed records and visual inspection of the pressure data. By visual inspection portions of the analog records with relatively large pressure fluctuations were isolated. The corresponding wind speed and direction records were then inspected to choose the segments where $\bar{v}$ and $\bar{\theta}$ showed a fairly constant mean value over a period of about 15-30 min. Records from a given run with $\bar{v}$ greater than 20 fps were then analyzed.

In order to assess the dependence of the wind loads on the independent variables of Eqs.(25) and (26), the analyses were carried out in accordance with the following:

1. Variation of wind loading with height z. Corresponding window locations were chosen on each of the three floors, 9th, 21st, and 28th. For each of these locations, records corresponding to a constant wind direction $\bar{\theta} = \bar{\theta}_o \pm 10^o$ were processed to obtain the PSD and the histograms.

2. Dependence of the wind loading on the wind direction $\bar{\theta}$. The variables ϕ_z and z were kept constant by selecting pressure records, for a particular window on a given floor, corresponding to wind directions differing by at least 30^o.

3. Variation of wind loading along the building profile. To assess this effect, the variables $\bar{\theta}$ and z had to be kept constant and the local pressure characteristics examined as ϕ_z was varied. Thus for a preselected wind direction (accurate to within 10^o) the pressure spectra and histograms for a number of windows on a given floor were obtained. The variation of wind direction from the selected mean for

each of these windows was less than 20^{o}. The difference was due to the data being recorded in different sessions.

In all, about 96 hours of usable data were recorded (Table 2). The grouping of the sorted data is summarized in Table 3.

Estimation of the power spectra with high stability and fidelity from the analog records required that careful consideration be given to the analysis parameters. The selection of these parameters is described in the following section.

Design of The Spectral Analysis

The formal mathematical basis for power spectrum estimation techniques can be found in the more general topic of estimation theory. However, power spectrum estimation as it is currently practiced has a very strong empirical basis [45]. As a consequence in digital computation of spectra there are generally tradeoffs involved between different analysis parameters. In designing a spectral analysis in advance of data collection, therefore, a general agreement on the best combination of analysis parameters is rare. After data acquisition, however, the analysis parameters can be suitably chosen by conducting a pilot analysis. In the following, such a pilot analysis is described and the selection of the various analysis parameters illustrated.

Before conducting a spectral analysis of the raw data certain preprocessing operations are necessary. Important amongst these are:

1. Sampling considerations
2. Trend removal
3. Stationarity check

Table 3. Data Sorting on the Basis of Wind Direction

Window Location	$\bar{\theta}$	$\bar{v}$ fps	Record #	$\bar{\theta}$	$\bar{v}$ fps	Record #	$\bar{\theta}$	$\bar{v}$	Record #	$\bar{\theta}$	$\bar{v}$	Record #
F28 W10	160°	24	17				108°	24	1	72°	24	1
N4	160°	24	17	280°	15	4						
NE3	160°	24	17									
NE3				280°	24	2						
N10				280°	18	3						
NW4												
F21 W11	160°	18	16				81°	15	6			
N3	160°	18	16	280°	24	12	119°	21	8			
NE1	160°	18	16	280°	24	12	324°	12	5			
NW2												
NW19												
F9 W10	160°	30	15									
N4	160°	30	15	270°	30	13						
NE1	160°	30	15	270°	30	13						
NW4	160°	30	18									
NW12	160°	30	18	270°	30	13						

Sampling considerations require that the maximum frequency, F_{max}, expected in the data be known and that digitization should be in accordance with Shanon's sampling theorem. The maximum frequency in the pressure data was limited to 50 Hz by an analog low pass filter with a roll-off rate of 48 dB/octave, to minimize aliasing errors. The actual frequency range of interest was about 40 Hz since it was sufficient to include the first few response modes, and was within the dynamic response bandwidth* of the pressure transducer.

A trend in the data is defined as any frequency component whose period is longer than the record length. Translated into Fourier Analyzer terminology this means that the least frequency in the data should be greater than the frequency resolution Δf. A low frequency trend is illustrated by curve (a) of Fig. 21. In general the trend is removed by means of linear or polynomial regression. For the pressure data, considering the physics of the phenomena (significant energy at low frequencies) high pass analog filtering with a cut off frequency of approximately $2\Delta f$ was used. The advantages afforded by high pass filtering were threefold:

(a) Reduced quantization noise. To keep the quantization noise level low the signal must occupy as much of the input range of the A/D converter as possible [47]. High-pass filtering eliminates the large low frequency excursions and permits digitization of the small fluctuations about the mean with reduced quantization noise.

---

* Note that the power spectrum contains no phase information and as a result the phase response of the transducer is inconsequential.

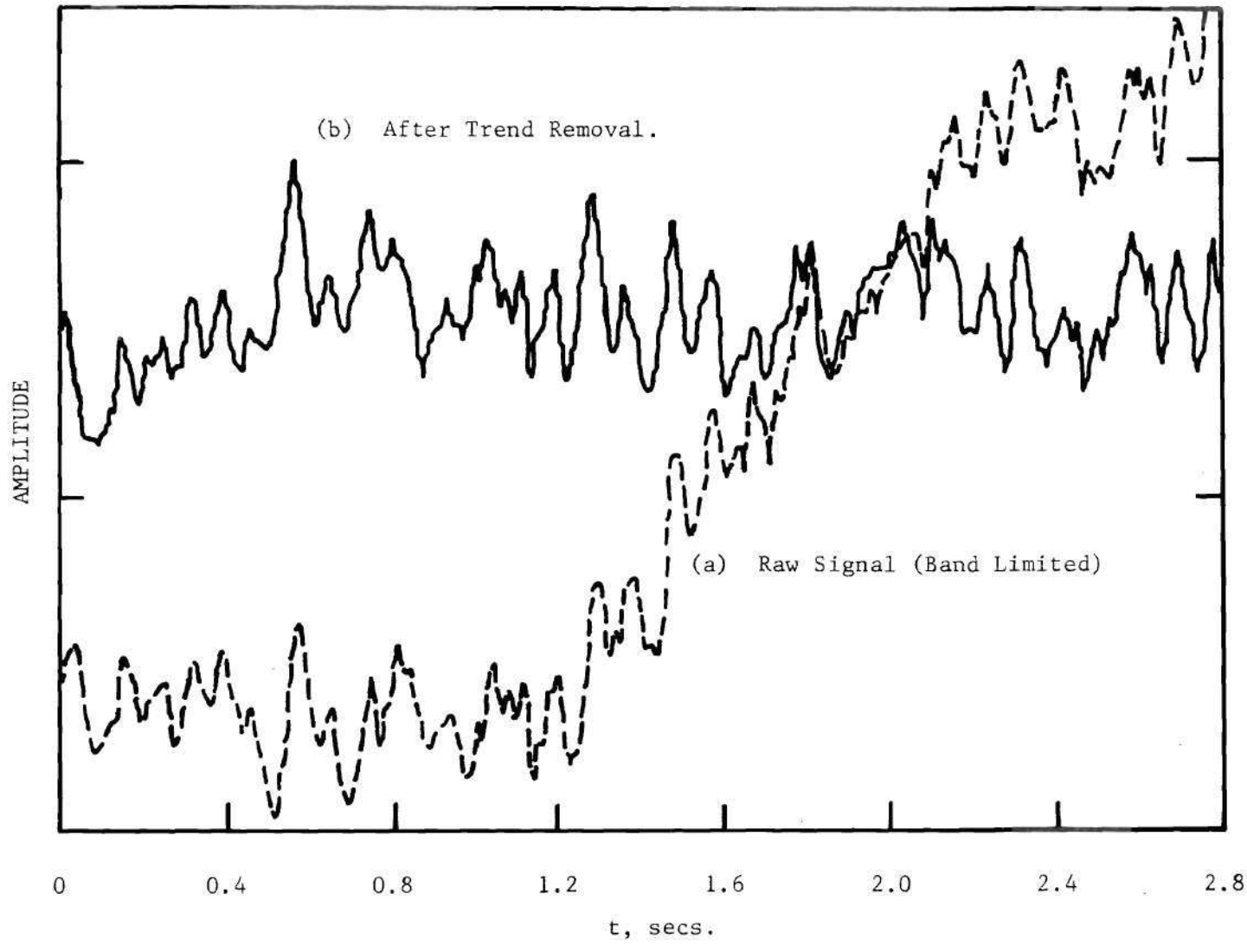

Figure 21. Trend Removal.

(b) Increased dynamic range. Dynamic range, for present purposes, can be defined as the ratio of the highest and lowest spectral component that the processor can detect from the roundoff and quantization noise. The dynamic range of the Fourier Analyzer is 90 dB (double precision spectra, 32 bit word size). The high value of the dc component can often exceed this range and can effectively drown out the small values at the high frequency end of the spectrum. High pass filtering thus provides increased dynamic range.

(c) Removal of the low frequency trend, curve (b) Fig. 21. Trend removal by high-pass filtering required that the pressure spectrum be analyzed in two parts, namely in a high frequency and a low frequency band. The subdividing frequency was chosen after the analysis parameters had been finalized.

The wind pressures are not expected to be stationary over the entire recording period ($\sim$6 hrs.) due to temperature changes and gust variations. However, stationarity over a short period (an hour or so) was checked for representative data by the run test in accordance with Ref. 31. The procedure is summarized in Appendix D. Over these periods, the data were found to be stationary.

Estimation of the power spectra from the stationary random data requires consideration of the following errors:

1. Frequency Leakage
2. Bias errors in the estimate
3. Variance errors in the estimate

Referring back to Chapter III, Eqs.(39) thru (45), the error

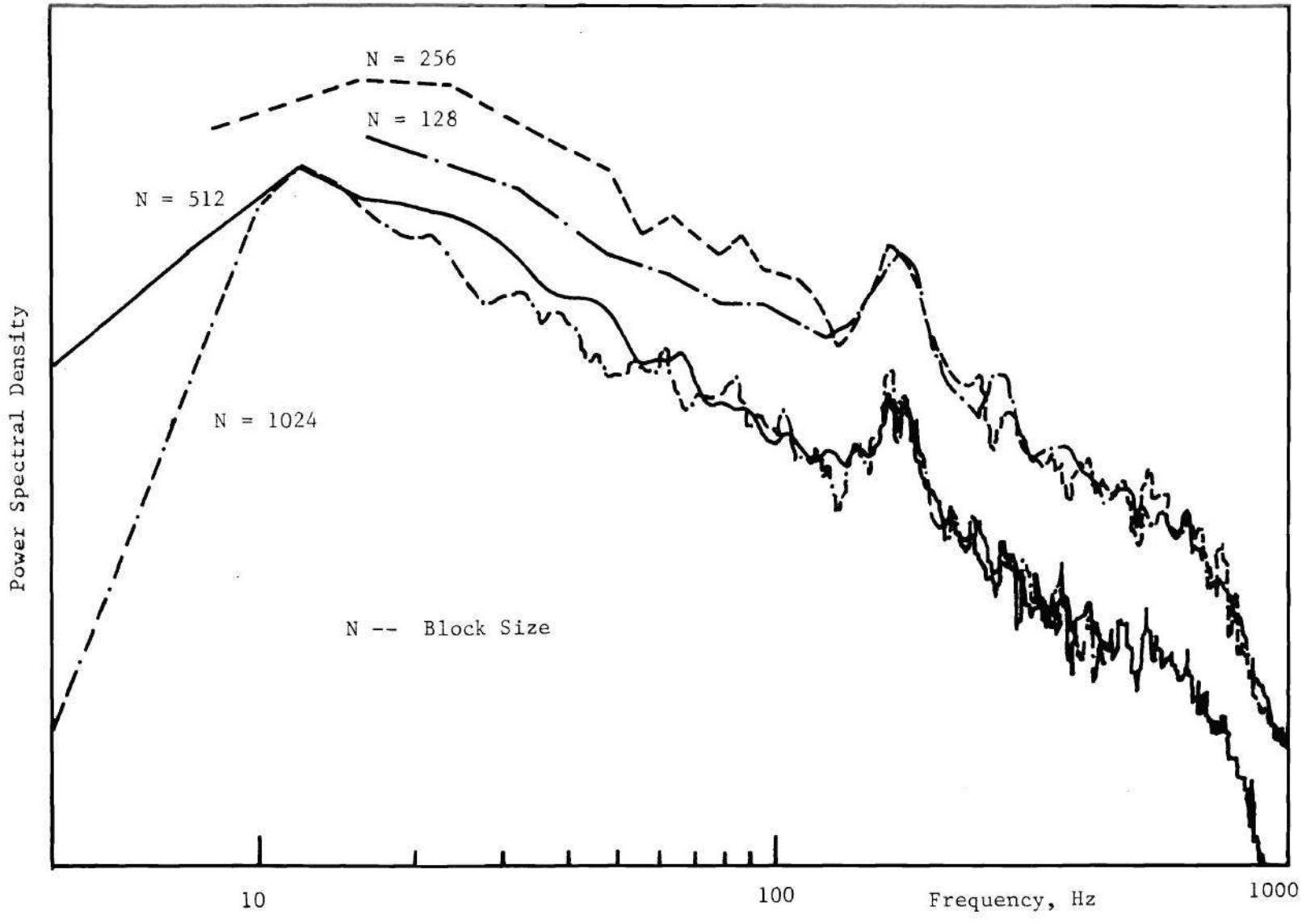

Figure 22. Effect of Block Size on Spectral Estimates.

considerations reduce to the selection of:

(a) a suitable time window $w(t)$

(b) frequency resolution Δf or block size N

(c) number of averages n_d

The choice, to a large extent, depends on the nature of the data and constitutes the design problem. The single Hanning window was chosen to reduce leakage since it provides considerable side lobe suppression with a small main lobe width [46].

Figure 22 illustrates the effect of varying the block size N and hence Δf^* on the bias of the estimate. It is seen that for N = 512, 1024 the bias has been reduced at the expense of the variance. The variance can be reduced by increasing the number of disjoint records averaged, n_d according to the following [38]:

$$\frac{\sigma}{\mu} = \frac{1}{\sqrt{n_d}} \tag{46}$$

Assuming a Gaussian distribution the mean can be estimated within 10% of its true value with 95% confidence if

$$\frac{1.96\sigma}{\mu} = .01 = \frac{1.96}{\sqrt{n_d}} \tag{47}$$

---

*$\Delta f = F_{max} / N/2$, i.e. for a given F_{max} increasing the block size is equivalent to increasing the frequency resolution.

which yields $n_d \simeq 384$. The reduction in variance is apparent from Fig. 23.

The bias of estimates for N = 512 and 1024 shows no significant change. However, the computation time for N = 1024 is increased. Hence N = 512 was chosen.

The analysis parameters can be summarized as follows:

1. Maximum Frequency = 50 Hz
   Block Size = 512
   High Pass Filter = 0.625 Hz
   Anti-Aliasing Filter Set at 50 Hz
   Number of Averages = 400

The lowest frequency that can be resolved with the above parameters is about 0.75 Hz. Hence the low end of the spectrum had to be analyzed separately. The parameters used for the low frequency part of the spectrum were:

2. Maximum frequency = 3.125 Hz
   Block Size = 512
   High Pass Filter = 0.025 Hz
   Anti-Aliasing Filter = 3 Hz
   Number of averages 30

The lowest frequency that could be resolved was 0.025 Hz, which corresponds to a period of 40 secs., sufficient to include short duration gusts.

Results and Discussion of Results

In describing the wind loading as a random process the data were

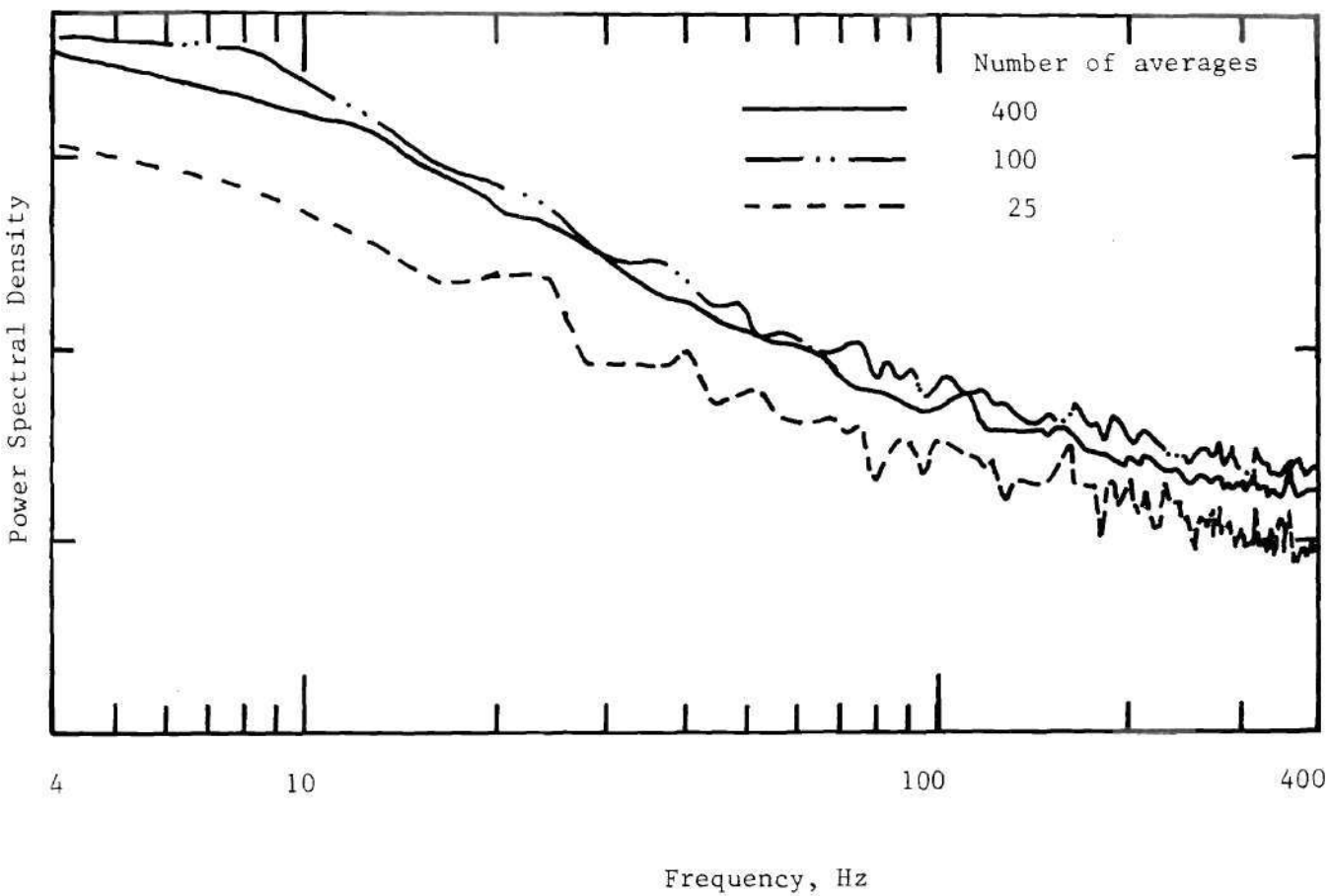

Figure 23. Effect of Averaging on Spectral Estimates.

processed to obtain the following descriptors:

1. High frequency band spectra (0.8-40 Hz)
2. Low frequency band spectra (0.03-3 Hz)
3. Normalized histograms

The available data permit a qualitative assessment of the wind loading with respect to the following values of the independent variables:

1. Wind Direction, θ		160^{o}, 280^{o} ($\pm 10^{o}$)
2. Height	z	28th Floor (357.5 ft.)
(Total height 376.15 ft.)		21st Floor (270 ft.)
		9th Floor (120 ft.)
3. Window Locations		N4, W10, NE1, (Fig. 18)

It appeared convenient to group and evaluate the results in two categories associated with the two wind directions 160^{o} and 280^{o}.

Wind Incidence $\bar{\theta} = 160^{o}$

Figures 24a, b and c show the spectra and normalized histograms for window N4 with the height z as a parameter and $\bar{\theta} = 160^{o}$. The respective floor planforms and wind incidence for the three floors are shown in Fig. 18. The window N4 is on the windward side, and the turbulence characteristics of the distant flow are expected to be preserved.

If the flow is visualized as 2-dimensional, the location N4 is expected to be downstream of the stagnation point and in the reattached region (flow separation at the corner). The pressure fluctuations, therefore, must be due to the wind turbulence and possibly due to

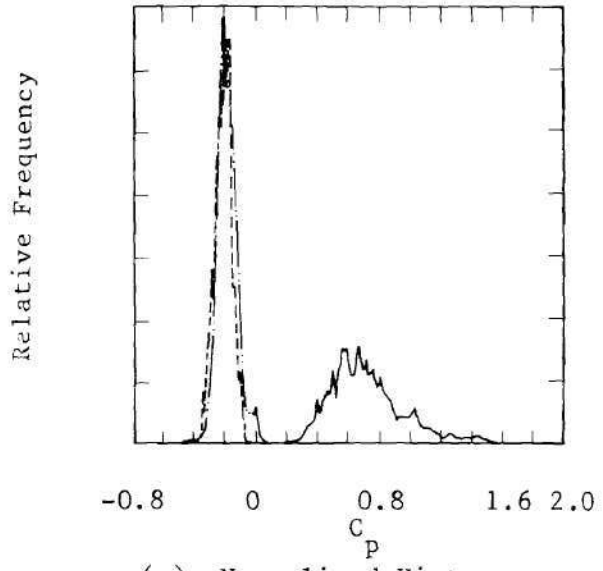

(a) Normalized Histogram

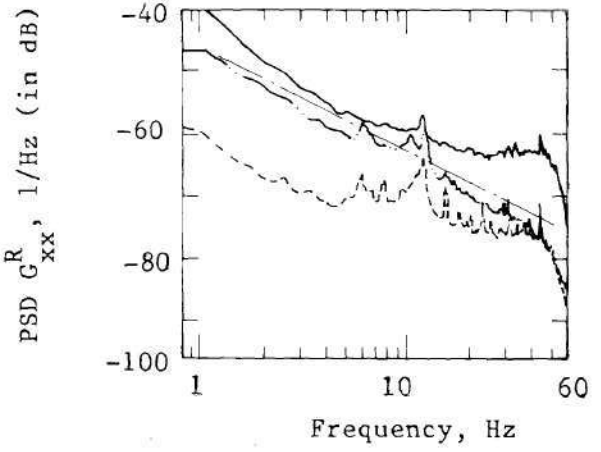

(b) High Frequency Band PSD

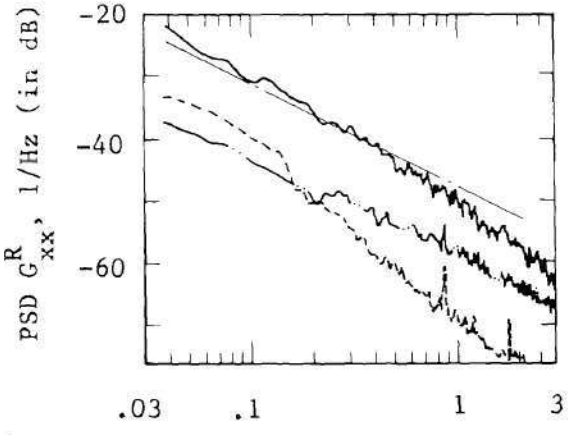

(c) Low Frequency Band PSD

Notes:

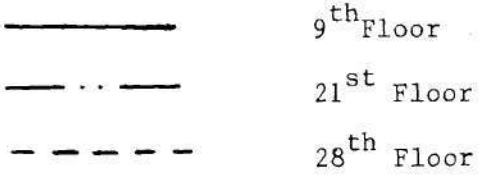

PSD in dB Relative to 1 1/Hz
e.g. -20 dB = 10^{-2}

Figure 24. Spectra and Normalized Histograms, Window N4, $\bar{\theta} = 160^{\circ}$

roughening caused by the mullions. It appears reasonable then to consider the pressure characteristics at N4 as reference and examine with respect to these the pressure fluctuations at aerodynamically complex locations such as W10 and NE1. It is recognized, however, that in reality the flow is 3-dimensional and pressure characteristics at the higher floors may be considerably altered due to upflow.

Magnitudes of the pressure coefficients are seen, from Fig. 24a, to be considerably higher at the 9th floor than at the upper floors. The positive pressure coefficients at the 9th floor and the mostly negative C_p's at 21st and 28th suggest the existence of an upflow. At the same time discrete frequencies are seen in the low frequency band spectra as follows:

1. 28th $f_1 = 0.86$ Hz $f_2 = 1.7$ Hz
2. 21st $f_1 = 0.86$ Hz
3. 9th None

These frequencies could be due to vortex shedding from the reverse setbacks at the 19th and the 24th floor, Fig. 10. In the event that there is some upflow, the pressure fluctuations at the 21st floor are affected by a single change in cross-section, whereas at the 28th the flow has traversed two cross-sectional changes. The fact that $f_1 = 0.86$ Hz is seen in the PSD for 21st as well as the 28th and that $f_2 = 2f_1$, serves to reinforce the observation that there is an upward flow component (not necessarily vertical) and periodicities are induced by the setbacks. That $f_1 = 0.86$ Hz is generated by the characteristic corner dimension $d_{19} = 14.42'$ and $f_2 = 1.7$ Hz is generated by the

characteristic corner dimension $d_{24} = 7.32'$ is evident from the Strouhal number, $S = \frac{fd}{\bar{v}} = 0.48$ in both cases. The Reynolds number based on the corner dimension is of the order of 10^6.

The high frequency band spectra, Fig. 24b, reveal that the mean square value of the pressure fluctuations decreases with increasing height. The PSD levels in dB are with respect to $G^R_{xx} = 1\text{sec}^*$. The histograms, Fig. 24a, show, however, that the variance at the 28th and the 21st floors is approximately the same. This is because of the increased energy at the 28th (higher PSD level, Eq.40) floor for low frequencies, Fig. 24c. In Fig. 24b, a discrete frequency component is seen at approximately 12 Hz in all three spectra. f = 12 Hz corresponds to the fundamental frequency of the glass plates and has appeared in the spectrum due to feedback to the wind pressure and/or motion of the pressure tap which was located on the window support. Association of this frequency with the flow characteristics, therefore, seems tenuous at best. The narrow band noise about 6 Hz in PSD-21 and PSD-28 could be due to the external architectural features such as the protruding mullions affecting the flow. In PSD-9 this frequency band has lost prominence due to higher energy levels. The flattening of PSD-9 and PSD-28 seen beyond about 20 Hz in Fig. 24b is unusual as regards turbulence spectra, but was also observed in a number of other instances. One possible reason is that in these particular runs the combination of the transducer range and the tape recorder gain served to restrict the

---

* G^R_{xx} has been defined in Chapter II as the reduced spectrum $G_{xx} / \left\{\tfrac{1}{2}\rho\bar{v}^2\right\}^2$ having the dimension 1/Hz.

dynamic range and thus caused the low amplitude high frequency fluctuations to be drowned out by the noise. Another feature, i.e., the effect of the anti-aliasing filter is clearly seen from the sharp roll-off beyond 50 Hz.

Figures 25a, b, and c show the results for the aerodynamically more complex case of window W10 with $\bar{\theta} = 160^{o}$. The location of the window W10 is downstream of a varying number of corners depending on the height being considered.

The magnitudes of the pressure coefficients are smaller than for N4 at $z = 9$. The pressure coefficients at $z = 9$ and $z = 28$ are predominantly negative, whereas at $z = 21$ they are distributed such that $\bar{C}_p \simeq 0$ (actually $\bar{C}_p = 0.008$). One explanation for this behavior is the roughening effect provided by the corners. The large corner dimensions and the small number of corners at $z = 9$ may not dramatically affect the flow at location W10. Hence the pressure coefficients at W10 are expected to be the same as they would be for flow around a right corner, thus accounting for negative C_p's. However, negative C_p's are also predominant at $z = 28$. In this case the much smaller corner dimensions and the large number of corners tend to smooth out the diagonal from face N to face W. Therefore, W10 again happens to be around a corner with respect to the flow, although the corner is not as sharp as at $z = 9$, and negative C_p's can be expected. At the 21st floor on the other hand the corners may be expected to roughen up and thus randomize the flow. This results in negative and positive C_p's occuring equally often. Considering the roughening effect in terms of

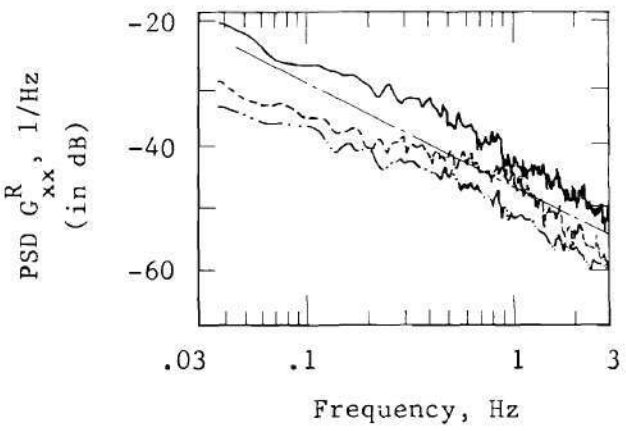

(c) Low Frequency Band PSD

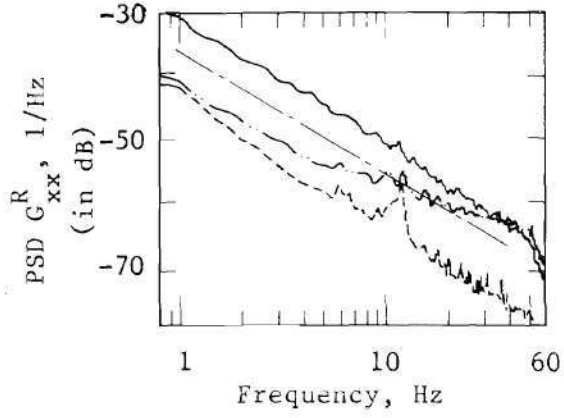

(b) High Frequency Band PSD

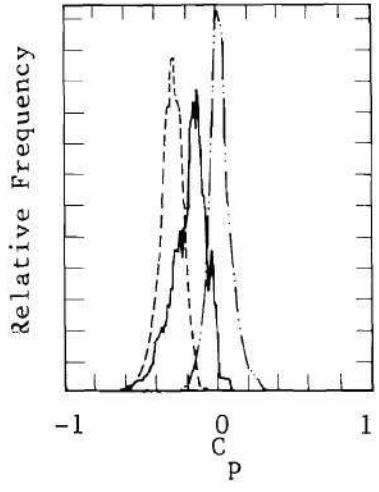

(a) Normalized Histogram

Notes:

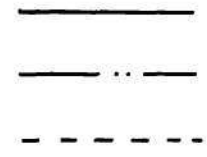

9^{th} Floor

21^{st} Floor

28^{th} Floor

PSD in dB Relative to 1, 1/Hz

e.g. -20 dB = 10^{-2}.

Figure 25. Spectra and Normalized Histograms, Window W10, $\bar{\theta} = 160^{\circ}$

the ratios $r = \frac{d_1}{d_2}$ (see Fig. 18 for notation) it is seen that $r_9 = 0.34$ and $r_{28} = 0.085$ provide the extremes, whereas, $r_{21} = 0.17$ tends to alleviate the pressure loads.

The high frequency band spectra are somewhat different from those at N4. The energy levels of the spectra at $z = 9$ and $z = 28$ are considerably higher for W10 (of the order of 10 dB or by a factor of 3 on the rms values of the pressure) than on N4. However, the spectra for W10, $z = 9$ and 28 roll-off much faster with frequency. The flattening out of PSD-9 and PSD-28 in Fig. 24b is attributed to the energy levels being in the noise floor. The trends in PSD levels, however, are similar in that the levels decrease with height. At W10 for $z = 21$ the PSD levels, Fig. 25b, are almost the same as in Fig. 24b, $z = 21$, although the slopes differ somewhat. These observations suggest that higher levels of PSD, i.e. higher energies in a frequency band occur in regions of negative pressure in so far as $z = 9$ and $z = 28$ are concerned. On the other hand the small changes in energy levels at $z = 21$ could be due to flow randomization. The observation that the energy levels decrease with height in the two cases considered, suggest that the lower building regions are affected by the terrain features so as to increase the bandwidth of the wind loads. The peaks in the spectra around 12 Hz may be fictitious as pointed out before. The low frequency band spectra, Fig. 25c, except for minor differences in levels are similar.

Window NE1 is located at a reentrant corner with respect to the flow direction being considered. The results for this case are shown in Figs. 26a, b, and c. Referring to Fig. 26a, it is seen that the pressure coefficients for $z = 9, 21$ are predominantly negative whereas at

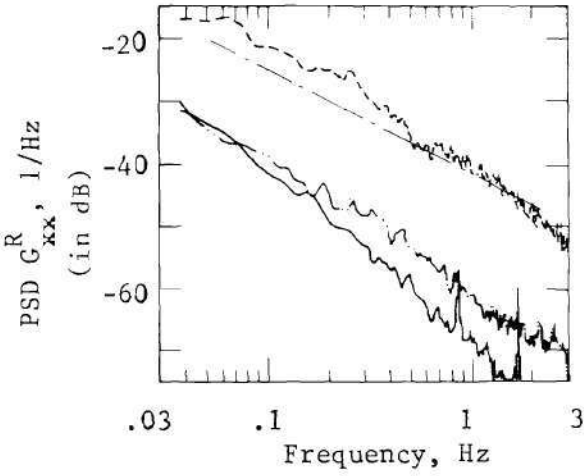

(c) Low Frequency Band PSD

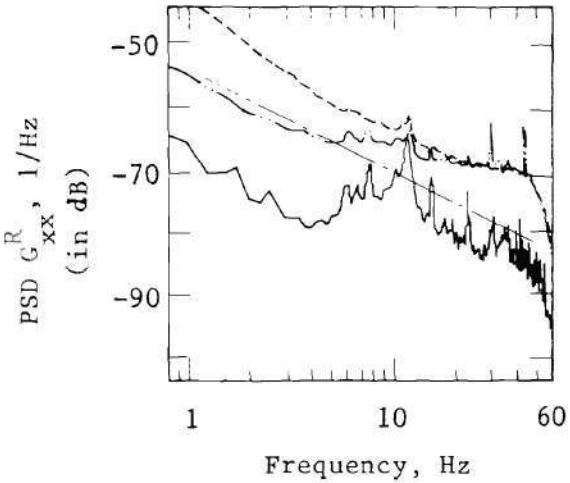

(b) High Frequency Band PSD

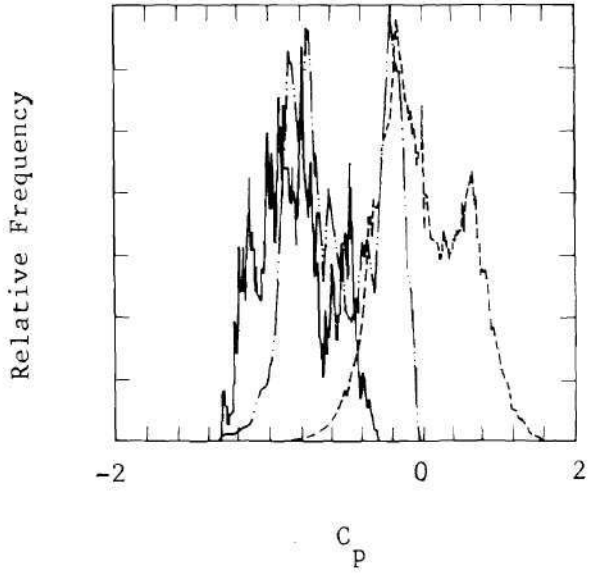

(a) Normalized Histograms

Notes:

———— 9^{th} Floor

— · · — 21^{st} Floor

– – – – 28^{th} Floor

PSD in dB Relative to 1, 1/Hz

e.g. -20 dB = 10^{-2}.

Figure 26. Spectra and Normalized Histograms, Window NE1, $\bar{\theta} = 160^{o}$

$z = 28$ they are more evenly distributed. Table 4 shows the different C_p values and the factor g from Eq.(3) for the various window locations considered so far. The aerodynamic effects are more complex at this location than the previous cases. This is evidenced by the shape of the histograms. Even after taking into account variance in the pdf estimates, the pdf's at $z = 21$ and 28 appear to have periodic components as manifest by the presence of dual peaks. A cross-check with the respective spectra does not reveal any discrete frequency component of comparable amplitude.

The high frequency band spectra are now reversed in energy levels, in that the overall energy levels and hence the mean square values increase with height, Fig. 26. This suggests that in a region of separation, such as can be expected at NE1, the rms values of the pressure fluctuations increase with height. For $z = 21$ the PSD contains a discrete frequency peak at 30 Hz and it is suspected that rotating machinery in the building (such as 1800 rpm motors used in the airconditioning unit) may have caused it to appear in the signal.

The low frequency band spectra of Fig. 26c show level variations similar to the high frequency band. However, the PSD for the 9th floor reveals the discrete frequencies 0.86 Hz and 1.7 Hz. The flow effects in this region are extremely complex and although the characteristic frequencies could have been produced by a downwash, such a description is at best crude conjecture at this time.

Wind Incidence, $\bar{\theta} = 280^{o}$

Figures 27 a, b, and c show the spectra and histograms for window

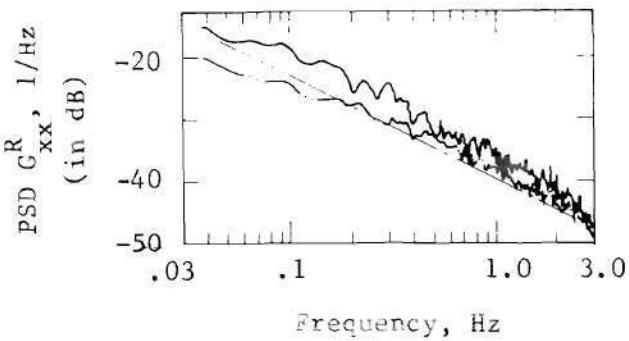

(c) Low Frequency Band PSD

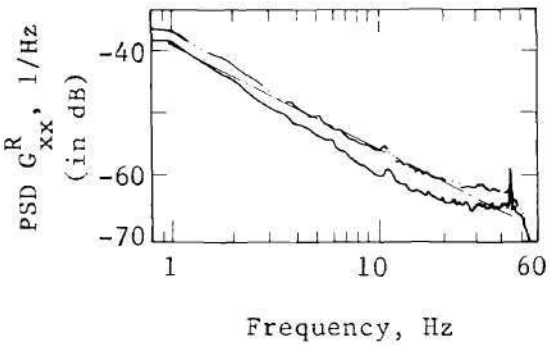

(b) High Frequency Band PSD

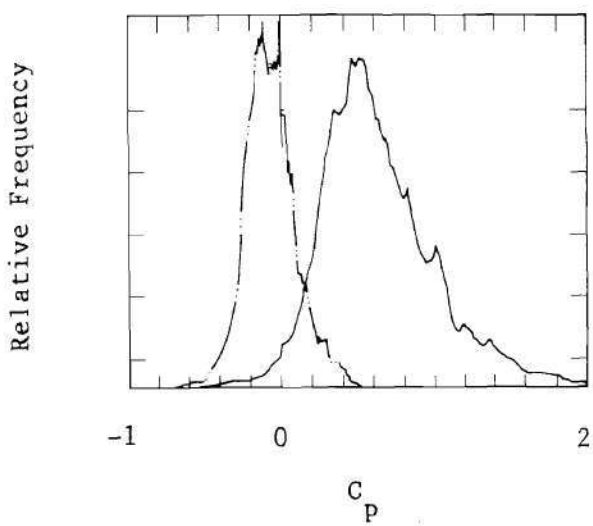

(a) Normalized Histogram

Notes:

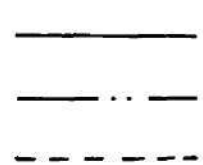

9^{th} Floor

21^{st} Floor

28^{th} Floor

PSD in dB Relative to 1, 1/Hz

e.g. -20 dB = 10^{-2}.

Figure 27. Spectra and Normalized Histograms, Window NE1, $\bar{\theta} = 280^{\circ}$

Table 4. Pressure Coefficients and Gust Factors for $\bar{\theta} = 160^{o}$

Floor	Window	$\bar{C}_p$	$C_{p_{rms}}$	C'_p	$C_{p_{max}}$	$g = \frac{C_{p_{max}}}{C'_p/\bar{C}_p}$
28	W10	-.307	.313	.061	-.7	3.52
	N4	-.203	.210	.054	-.38	1.43
	NE4*	+.014	.277	+.277	+.86	.043
21	W11	+.008	.075	.075	+.384	.041
	N3	-.197	.206	.06	-0.53	1.73
	NE1	-.55	.622	.29	-1.36	2.6
9	W10	-.398	.524	.339	-2.64	3.08
	N4	+.46	.472	.106	.84	3.66
	NE1	-.591	.764	.234	-1.77	4.47
	NW12	.539	.753	.526	+2.80**	2.87

*NE4 presents the same profile to the flow as NE1 except for an additional upstream corner.

**Positive C_p greater than +1 since the local velocities may be considerably different from the reference velocity.

NE1 at z = 9 and 21. The windward location of NE1 together with the larger corner dimension at z = 9 results in 9NE1 having C_p histogram which is almost entirely on the positive side*.

The high frequency band spectra, Fig. 27b, show that the mean square value of the pressure fluctuations is larger at z = 21 than at z = 9. On the other hand in the low frequency band, Fig. 27c, the PSD levels, at frequencies below 0.5 Hz, are greater at z = 9. Considering the negative C_p's at z = 21 and differences in PSD levels it appears that an upflow component may exist and that the building facade features tend to produce increased higher frequency loading.

Window N4 is downstream of NE1 with respect to the flow and the wind direction is almost parallel to the wall on which the pressure tap is located. From Fig. 28a, the randomization effect of the corners at the 21st floor is apparent in that at z = 9, the C_p's are mostly positive and at z = 28 large negative C_p excursions occur, whereas at z = 21 the distribution is almost symmetric with respect to a zero mean.

The high frequency band spectra, Fig. 28b, have almost the same slope and closely follow the $f^{-5/3}$ Kolmogorov inertial subrange spectrum. The PSD levels do not show any particular trend with height thus asserting the complex 3-D nature of the flow interaction. The PSD level at N4 is reduced from that seen at NE1 for the 21st floor whereas for z = 9 it is almost the same. The periodicity at 12 Hz is

---

* The erroneous values $C_p > +1.0$ result because of differences in the local speeds and the remote reference velocity of the wind used for normalization.

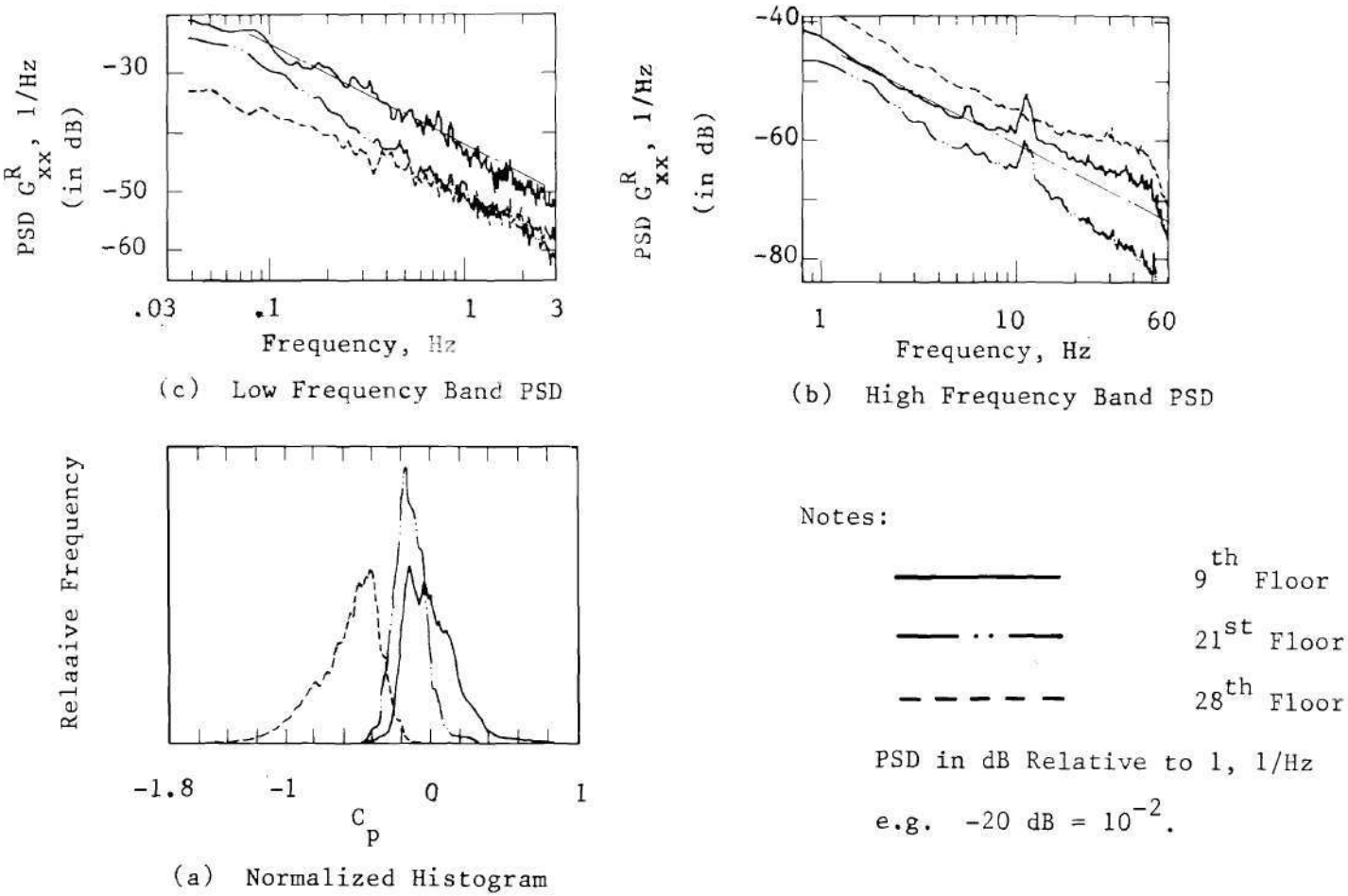

Figure 28. Spectra and Normalized Histograms, Window N4, $\bar{\theta} = 280^{\circ}$

associated with the window response although the amplitude of this component is higher than those observed in other cases.

Discrete flow effects such as peaks are not seen in the low frequency band spectra of Fig. 28c. The relative levels are same as in Fig. 28b.

In concluding this chapter, some observations about the general character of the pressure spectra are made, and the identified features of the cladding loads are summarized. With regard to dynamic cladding loads the overall PSD levels or the mean square values of the loading are of concern.

Higher spectral levels were seen to occur on faces where the pressure coefficients were predominantly negative. In other words the highest spectral levels can be expected when the bulk of the counts in a pressure histogram lie on the negative C_p side and the magnitude of the negative mean C_p is largest. The variance of the normalized histogram (pdf) and the area under a power spectrum are one and the same quantity, namely the mean square value of the random process (By Parseval's theorem Eq.40). This implies that the higher variance should be associated with the histogram having the larger magnitude of the negative mean pressure coefficient $\overline{C}_p$. That this is indeed the case is manifested by the longer negative tails in the histograms as $\overline{C}_p$ tends to be more negative.

The PSD levels on the windward side increased as the building ground level was approached, which is consistent with the assumption that gusts due to the effects of the surrounding terrain are largely responsible for the increase. The additional observation that in regions of

separation, i.e. where the wind effects are not direct, the spectral levels increase with height - serves to reinforce the speculation of the effects of surrounding terrain.

Discrete flow effects such as vortex shedding, narrow band pressure fluctuations (bandwidth approximately 1 Hz), and spikes in the high frequency band spectra, are seen only for some particular combination of ϕ, θ, and z. Exterior architectural features, such as mullions, are suspected to be the prime contributors to spectrum levels by way of narrow band fluctuations in the flow. Existence of an upflow and consequent vortex shedding at the reverse setbacks is responsible for the low frequency spectral lines corresponding to a Strouhal number of 0.48.

The multiple corners in the building planforms appear to act as roughness elements on the building profile. The relatively small number of large dimension corners, described by the nondimensional coefficient value $r = 0.34$, essentially act as bluff extensions of the building floor plan and are largely unaffected by the other corners. On the other hand, for a relatively large number of smaller dimension corners, described by $r = 0.085$, the roughening is considerably less. The side with such corners acts essentially as a flat wall, the corners at the ends of which are nearly unaffected by the intermediate corners. A building profile roughness described by $r = 0.17$, however, serves to randomize the flow effects, resulting in diminished mean and rms values of the pressure fluctuations (small mean and variance in the pdf, and low PSD levels). A preliminary indication, therefore, is that a roughness ratio in the vicinity of $r = 0.2$ could have an alleviating effect on the cladding loads.

A feature of the low frequency band spectra that deserves mention is that the spectra do not level-off or show a peak at the extremely low frequencies. This behavior is expected because of the finite energy in the pressure signal. The absence of a peak or limiting behavior could be due to the restricted bandwidth of the spectra. At these low frequencies the external wind pressures are no longer distinct from the internal building pressure variations due to normal building operations. The period of the internal pressure fluctuations could be considerably longer, perhaps extending over an entire day. Periods longer than about 30 secs. are not encompassed by the low frequency band spectra.

An inspection of the histograms for pressure taps located on a flat face with the flow nearly parallel to the face, shows that the distribution of the instantaneous C_p's moves to the negative side as the height increases. This is not at all a surprising result, but only an instance substantiating two of the conclusions drawn in the preceding. Specifically, it was seen that the spectral levels increase with height in regions of separation, and that higher spectral levels are associated with predominantly negative pressure coefficient histograms, i.e. where the bulk of the counts in a pressure histogram lie on the negative C_p side. The above observation, therefore, provides increased confidence in the consistency of the data.

The overall levels of the spectra in the Reynolds number range of $1\text{-}5 \times 10^6$ are in general quite small and would require considerable dynamic amplification by structural vibration to approach static load levels. The slopes of the spectra differ only slightly from the

Kolmogorov spectrum although for low energy levels they tend to be flatter.

CHAPTER V

WINDOW RESPONSE

Introduction

In the previous Chapter the salient features of wind loads on window units in a cladding system were identified from experimental data with special regard to dynamic loads. The question that immediately follows concerns the nature of the wind-induced dynamic response of a window unit in the exterior curtain wall. The present Chapter addresses itself to this question.

An assessment of the dynamic response of windows can, of course, be made directly from the response spectra evaluated from field measurements. However, it is essential to identify the response levels associated with the wind loads. This can be accomplished by means of the coherence function, the application of which in identifying noise and vibration sources has been previously mentioned. The coherence function, Eq.(22), as estimated from the measured wind load and response data, Eq.(42), serves to establish the causality of the wind loads for the response. In a practical measurement situation the measurement noise also affects the coherence function and can lead to erroneous, low values. These considerations and the evaluation of the response from the measured response spectra and the coherence function are discussed in the following sections in light of the experimental results.

As pointed out in Chapter II, the vibration characteristics of the window system can be described by the frequency response function H(f) and the transmissibility function T(f). These functions can be readily estimated from the ambient wind loading and response data and the validity of the estimates assessed by the respective coherence functions. Once these functions have been determined, the modal properties of the interconnected double plate system, and the nature of the forces transmitted to the boundary can be evaluated. However, one aspect of the wind load spectra, namely, the low levels in the high frequency band, suggest that significant vibration levels, that is to say, dynamic response, may not occur. If this is indeed the case, the implications are twofold:

(a) Ultra-low levels of the response spectra would provide increased confidence in the measured wind load spectra considering the uncontrolled nature of the experiment.

(b) The modal properties must be determined from the forced response.

These aspects of the dynamic response, and the measurement of modal properties, and transmissibility function by forced excitation of the window system are addressed in the later part of this Chapter. At first, however, the natural frequencies of the double plate system are estimated from a simple analytical model and are used for comparison with the measured data.

Analytical Model of the Window System

A typical insulating window assembly in the Tower Place curtain

wall is shown in Fig. 11. The following assumptions were made in modelling the window system:

1. The glass unit is simply supported in the framework, i.e. the mullions and the muntins. This is realistic since the rotational restraint offered by the compliant rubber gasket is negligible compared to the plate moments for the same order of deflections. Although in reality the presence of the neoprene gasket implies yielding supports, it is assumed for simplicity that the supports are rigid.

2. The effect of the air gap is that of distributed linear stiffness elements expressed in terms of the force per unit displacement (in modes of vibration where volume changes occur) per unit area.

3. The metal spacer at the edges of the plates introduces rotational coupling between the plates. No attempt is made to calculate the rotational coupling directly. However, in the final calculations a range of values of the parameter K_θ (rotational restraint of the channel) were examined to assess the interplate connection.

With these assumptions the double plate system is modelled as shown in Figs. 29 and 30. The symbols used are defined as follows:

K_δ linear spring stiffness lbs/ft/ft^2

K_θ rotational spring stiffness lb-ft/radian/ft.

w_j $j = 1, 2$ Displacement functions of the upper and lower plate, respectively.

The model as formulated above leads to a nonlinear set of governing differential equations. This is because any volume change ΔV causes a uniform pressure change Δp_g and as a result the stiffness contributed by the air gap is a function of the displacements w. In

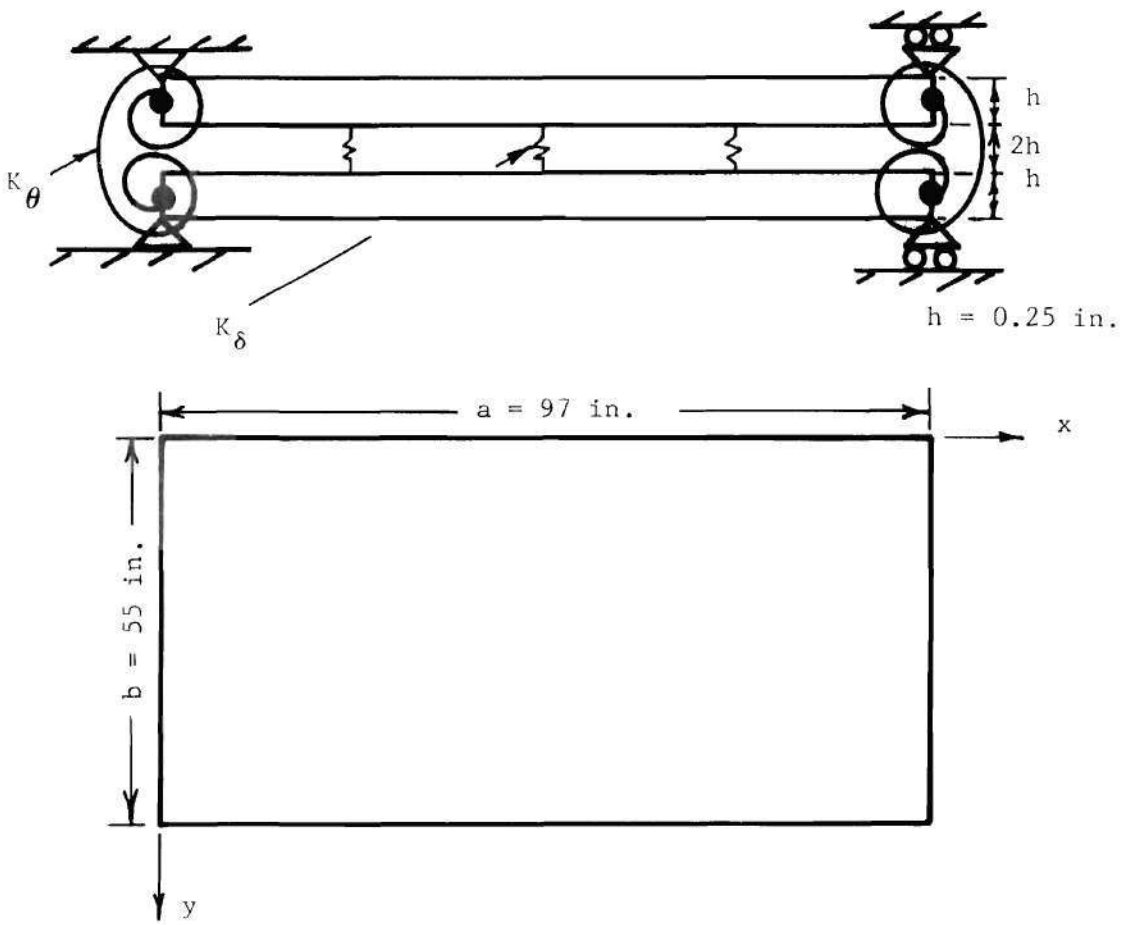

Figure 29. Structural Model of the Double Plate System

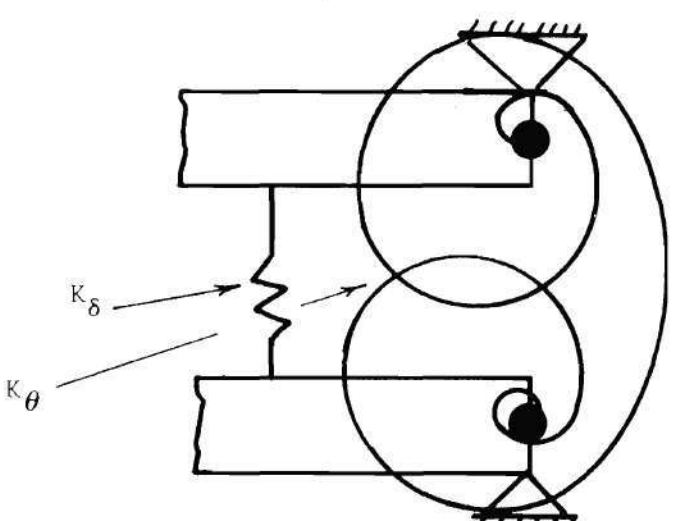

Figure 30. Details of End Connections

order to obtain an estimate of the natural frequencies the distributed spring stiffness was assumed constant in each mode of vibration. The constant $K_{\delta mn}$ was computed as the pressure change per unit modal amplitude in the mn^{th} mode. (For a net volume change the modes should be symmetric and the two plates moving out-of-phase). It is noted that the modal amplitude represents the maximum displacement in the natural mode of vibration. For a constant pressure change Δp_g, therefore, the stiffness $K_{\delta mn}$ as defined above underestimates the stiffness of the air gap and thus, the natural frequencies corresponding to out-of-phase motion. This, however, is not a serious problem since the estimates of the natural frequencies are obtained for reference purposes only.

A linear relationship between the volume change and the pressure change is assumed and is used to evaluate the interplate spring constant. The volume change is assumed to be an adiabatic process.

The governing differential equations for the double plate model of Fig. 29 can be written as follows, assuming the two plates are identical:

$$\begin{aligned} D\nabla^4 w_1 + \rho h \ddot{w}_1 &= -K_\delta (w_1 - w_2) \\ D\nabla^4 w_2 + \rho h \ddot{w}_2 &= -K_\delta (w_2 - w_1) \end{aligned} \tag{48}$$

After separation of variables

$$\begin{aligned} D\nabla^4 W_1 - \omega^2 \rho h W_1 &= -K_\delta (W_1 - W_2) \qquad (a) \\ D\nabla^4 W_2 - \omega^2 \rho h W_2 &= -K_\delta (W_2 - W_1) \qquad (b) \end{aligned} \tag{49}$$

$$W_i = W_i(x,y) \qquad i = 1,2$$

The boundary conditions are:

$$
\begin{aligned}
y = 0 \quad & W_1 = 0 \quad & D\frac{\partial^2 W_1}{\partial y^2} &= K_\theta \frac{\partial (W_1 - W_2)}{\partial y} \\
& W_2 = 0 \quad & D\frac{\partial^2 W_2}{\partial y^2} &= K_\theta \frac{\partial (W_2 - W_1)}{\partial y} \\
y = b \quad & W_1 = 0 \quad & -D\frac{\partial^2 W_1}{\partial y^2} &= K_\theta \frac{\partial (W_1 - W_2)}{\partial y} \\
& W_2 = 0 \quad & -D\frac{\partial^2 W_2}{\partial y^2} &= K_\theta \frac{\partial (W_2 - W_1)}{\partial y} \\
x = 0 \quad & W_1 = 0 \quad & D\frac{\partial^2 W_1}{\partial x^2} &= K_\theta \frac{\partial (W_1 - W_2)}{\partial x} \\
& W_2 = 0 \quad & D\frac{\partial^2 W_2}{\partial x^2} &= K_\theta \frac{\partial (W_2 - W_1)}{\partial x} \\
x = a \quad & W_1 = 0 \quad & -D\frac{\partial^2 W_1}{\partial x^2} &= K_\theta \frac{\partial (W_1 - W_2)}{\partial x} \\
& W_2 = 0 \quad & -D\frac{\partial^2 W_2}{\partial x^2} &= K_\theta \frac{\partial (W_2 - W_1)}{\partial x}
\end{aligned}
\tag{50}
$$

Considering the symmetry of the structure the solution of Eq.(49) satisfying boundary conditions given by Eq.(50) can be simplified by considering two distinct sets of vibration modes, namely in-phase and out-of-phase. For in-phase modes the two identical plates execute synchronous vibrations such that the displacements are in the same direction, i.e. the separation is maintained, all over the plate area.

In such a case the entrapped air acts as an additional mass which can be neglected in comparison with the plate mass. The eigenvalues for this case can be obtained by assuming

$$W_S(x,y) = W_1(x,y) + W_2(x,y) \tag{51}$$

as the solution of

$$D\nabla^4 W_S - \omega^2 \rho h W_S = 0 \tag{52}$$

Eq.(52) being obtained by the addition of Eqs.(49a) and (49b). The boundary conditions can be reduced in a similar fashion to:

$$\begin{aligned} y = 0,\ b \qquad & W_S = 0 \qquad \frac{\partial^2 W_S}{\partial y^2} = 0 \\ x = 0,\ a \qquad & W_S = 0 \qquad \frac{\partial^2 W_S}{\partial x^2} = 0 \end{aligned} \tag{53}$$

Eqs.(52) and (53) represent the simply supported plate conditions with the eigenvalues given by

$$\begin{aligned} \omega_{mn} &= \pi^2 \sqrt{\frac{D}{\rho h}} \left\{ \left[\frac{m}{a}\right]^2 + \left[\frac{n}{b}\right]^2 \right\} \\ W_{S_{mn}} &= \frac{2}{\sqrt{\rho ab}} \operatorname{Sin} \frac{m\pi x}{a} \operatorname{Sin} \frac{n\pi y}{b} \end{aligned} \tag{54}$$

$$\text{where,} \quad \rho \int\int W_{S_{mn}}^2 \, dxdy = 1$$

The eigenvalues for the out-of-phase motion can be obtained by considering

$$W_o = W_1(x,y) - W_2(x,y) \tag{55}$$

as the solution of the difference of Eqs.(49a) and (49b) given by:

$$D\nabla^4 W_o - (\omega^2 \rho h - 2K_\delta) W_o = 0 \tag{56}$$

Let $\Omega^2 = \omega^2 \rho h - 2K_\delta$, then

$$D\nabla^4 W_o - \Omega^2 W_o = 0 \tag{56a}$$

The boundary conditions are:

$$\begin{aligned} &y = 0,\ b \qquad W_o = 0 \qquad \frac{\partial^2 W_o}{\partial y^2} = \pm \frac{\xi_B}{b} \frac{\partial W_o}{\partial y} \\ &x = 0,\ a \qquad W_o = 0 \qquad \frac{\partial^2 W_o}{\partial x^2} = \pm \frac{\xi_A}{a} \frac{\partial W_o}{\partial x} \end{aligned} \tag{57}$$

where $\xi_B = \dfrac{2K_\theta b}{D}$; $\xi_A = \dfrac{2K_\theta a}{D}$

Eqs.(56) and (57) represent the governing equation and boundary conditions for a rotationally restrained rectangular plate, a solution for which has been obtained in Ref. 49. The procedure utilizes Rayleigh-Ritz method with the assumed eigenfunctions being those of a rotationally

restrained beam e.g.

$$W_o = \sum_m^M \sum_n^N a_{mn} X_m(x)\, Y_n(y) \tag{58}$$

where

$$X_m(x) = A_m \left\{ \mathrm{Cosh}\left(\frac{\alpha_m x}{a}\right) - \mathrm{Cos}\left(\frac{\alpha_m x}{a}\right) \right\} + B_m \left\{ \mathrm{Sinh}\left(\frac{\alpha_m x}{a}\right) + \mathrm{Sin}\left(\frac{\alpha_m x}{a}\right) \right\}$$

$$Y_n(y) = A_n \left\{ \mathrm{Cosh}\left(\frac{\alpha_n y}{b}\right) - \mathrm{Cos}\left(\frac{\alpha_n y}{b}\right) \right\} + B_n \left\{ \mathrm{Sinh}\left(\frac{\alpha_n y}{b}\right) + \mathrm{Sin}\left(\frac{\alpha_n y}{b}\right) \right\} \tag{59}$$

where

$$\left.\begin{aligned} A_r &= -\tfrac{1}{2}\,\mathrm{Cot}\,\frac{\alpha_r}{2} \quad ; \quad B_r = \mathrm{Cot}\,\frac{\alpha_r}{2}\,\mathrm{Tanh}\,\frac{\alpha_r}{2} \\ \alpha_r &= -\tfrac{1}{2}\,\xi\left(\mathrm{Tan}\,\frac{\alpha_r}{2} + \mathrm{Tanh}\,\frac{\alpha_r}{2}\right) \end{aligned}\right\} \; r=1,3,\text{etc.}$$

$$\left.\begin{aligned} A_r &= \mathrm{Tan}\,\frac{\alpha_r}{2} \; ; \quad Br = -\mathrm{Tan}\,\frac{\alpha_r}{2}\,\mathrm{Coth}\,\frac{\alpha_r}{2} \\ \alpha_r &= \tfrac{1}{2}\,\xi\left(\mathrm{Cot}\,\frac{\alpha_r}{2} - \mathrm{Coth}\,\frac{\alpha_r}{2}\right) \end{aligned}\right\} r = 2,\ 4,\ \text{etc.} \tag{60}$$

where α_r are the eigenvalues of the rotationally restrained beams.

In Ref. 49 an approximate frequency equation for vibration modes of a rotationally restrained plate is given. This is arrived at considering the fact that the characteristic beam functions used lead to a frequency determinant for the plate where the diagonal terms are much greater than the off-diagonal terms. The mn^{th} mode then is represented by the mn^{th} term only and the mn^{th} resonant frequency can be written

$$\Omega_{mn}^2 = \frac{1}{b^2}\sqrt{\frac{D}{\rho h}}\left[\left(\frac{b}{a}\right)^4 \alpha_m^4 + \alpha_n^4 + 2\left(\frac{b}{a}\right)^2 \phi_{mm}\phi_{nn}\right]^{\frac{1}{2}}$$

$$\phi_{mm} = \frac{\alpha_m^2\left[\alpha_m(B_m^2 + 1) + 2A_m(B_m - 1)\right]}{\alpha_m\left[(2A_m^2 - B_m^2 + 1)\right] + 2A_m(B_m+1)}$$

$$\phi_{nn} = \frac{\alpha_n^2\left[\alpha_n(B_n^2 + 1) + 2A_n(B_n - 1)\right]}{\alpha_n\left[2A_n^2 - B_n^2 + 1\right] + 2A_n(B_n + 1)} \qquad (61)$$

The stiffness K_δ for the entrapped air is determined along the lines of Ref. 50, neglecting resonances of the air mass* due to wave effects, and assuming adiabatic compression of the volume. The volume change is given by

$$\Delta V_{mn} = \int_o^a \int_o^b a_{mn} X_m Y_n \, dxdy$$

$$= a_{mn}\left\{x_m\right\}_o^a \left\{y_n\right\}_o^b \qquad (62)$$

where $x_m = \int_o^a X_m dx \qquad y_n = \int_o^b Y_n \, dy$

The linearized pressure-volume relationship for an adiabatic process can be written as:

$$\frac{\Delta p}{p_o} \simeq -\frac{\gamma \Delta V}{V_o}, \qquad \gamma = 1.4 \qquad (63)$$

---

* This assumption is reasonable for the present application up to 70 Hz, based on the largest plate dimension.

The interplate spring constant $K_{\delta mn}$ in the mn^{th} mode is calculated as:

$$K_{\delta mn} = \frac{\Delta p_{mn}}{a_{mn}} \simeq \frac{\gamma p_o}{V_o} \frac{\Delta V_{mn}}{a_{mn}} \tag{64}$$

$$V_o = \frac{97 \times 55 \times 0.5}{1728} \text{ cu. ft.} = 1.544 \text{ cu. ft.}$$

$$p_o = 14.7 \text{ psi} = 2116.8 \text{ psf}$$

Therefore, using Eqs.(62) and (64)

$$K_{\delta mn} = 1919.38 \quad x_m y_n \tag{65}$$

As an example for the (1,1) mode of a rotationally restrained system with $\xi_B = 2.0$ corresponds to a rotational stiffness

$$K_\theta = \frac{D\xi_B}{2b} = 256.2 \text{ ft lbs/radian/ft.}$$

and, $$K_{\delta_{1,1}} = 34347.43 \text{ lbs/ft./ft}^2.$$

The calculated values of the natural frequencies of in-phase motion up to 55 Hz, and the corresponding values for out-of-phase motion are shown in Table 5. The natural frequencies of the rotationally restrained plates are evaluated for extreme and intermediate values of ξ_B ($\xi_A = \frac{\xi_B a}{b}$). It is recognized that $\xi_B \simeq 0$ implies no plate interconnection at the boundaries, whereas $\xi_B = \infty$ implies a rigid connection.

Table 5. Natural Frequencies of the Double Plate System

Mode Shape		Natural Frequency, f_n in Hz			
m(x-ax)	n	In Phase	Out of Phase, K_θ & K_δ included		
		S.S. Bc's	$\xi_B = 1 \times 10^{-10}$	$\xi_B = 2.0$	$\xi_B = 1 \times 10^{10}$
1	1	10.46	120.02	129.35	160.14
2	1	18.09	18.09	20.04	28.44
3	1	30.81	75.60	81.98	112.46
1	2	34.21	34.21	36.86	52.10
2	2	41.84	41.84	44.32	59.80
4	1	48.61	48.61	50.41	62.03
3	2	54.56	54.56	56.85	72.80

Coherence Function from Measured Response

The practical implementation of the coherence function is based on the single input/single output problem of Fig. 31. The true source, or input, of the system is $u(t)$, assumed to be stationary, and the output is $v(t)$. Extraneous noise at the input and output measurement points is represented by $n(t)$ and $m(t)$, respectively, and is assumed to be incoherent with $u(t)$ and $v(t)$. The quantities $x(t)$ and $y(t)$ are the measurement signals. Note that $x(t) = u(t) + n(t)$ and $y(t) = v(t) + m(t)$.

The input-output relationships for such a system are:

$$G_{xx}(f) = G_{uu}(f) + G_{nn}(f) \tag{66}$$

$$G_{yy}(f) = G_{vv}(f) + G_{mm}(f) \tag{67}$$

$$G_{xy}(f) = G_{uv}(f) \tag{68}$$

$$G_{vv}(f) = |H(f)|^2 G_{uu}(f) \tag{69}$$

$$G_{uv}(f) = H(f)\, G_{uu}(f) \tag{70}$$

where Eqs.(69) and (70) follow from Eq.(20), and Eqs.(66), (67), (68) follow from the assumption that the extraneous noise signals $n(t)$ and $m(t)$ are uncorrelated* with the signals $u(t)$ and $v(t)$.

---

* For the effect of correlated noise on the coherence function see Ref. 51 .

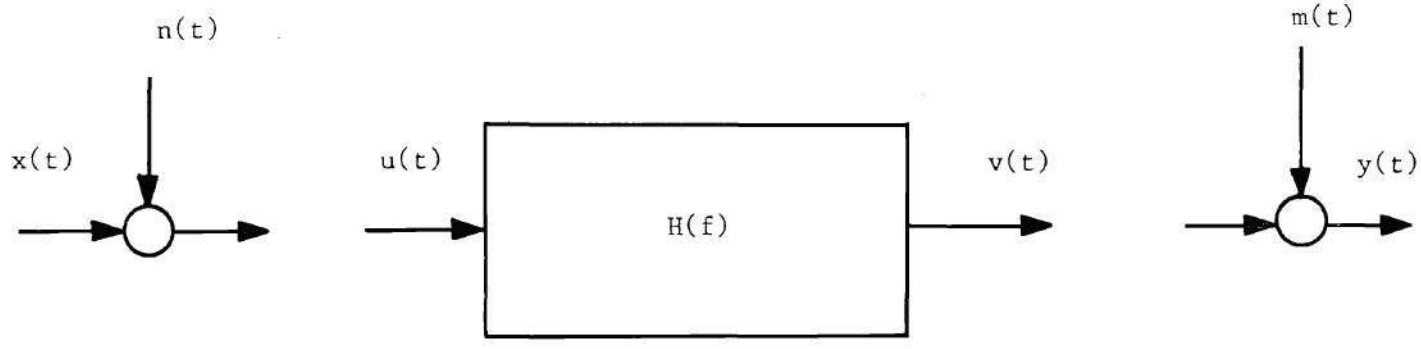

Figure 31. Ordinary Coherence Function Measurement Model

The true system coherence function $\gamma^2_{uv}(f)$ is defined as

$$\gamma^2_{uv}(f) = \frac{\left|G_{uv}(f)\right|^2}{G_{uu}(f)G_{vv}(f)} \tag{71}$$

and for a CPLS system is identically equal to one for all frequencies. The true coherence is related to the measured coherence function $\gamma^2_{xy}(f)$ as follows:

$$\gamma^2_{xy}(f) = \frac{\left|G_{xy}(f)\right|^2}{G_{xx}(f)G_{yy}(f)}$$

$$= \frac{\left|G_{uv}(f)\right|^2}{\left[G_{uu}(f) + G_{nn}(f)\right]\left[G_{vv}(f) + G_{mm}(f)\right]}$$

$$= \frac{\gamma^2_{uv}(f)}{\left[1 + \frac{G_{nn}(f)}{G_{uu}(f)}\right]\left[1 + \frac{G_{mm}(f)}{G_{vv}(f)}\right]} \tag{72}$$

Thus, the measured value of the coherence function is diminished from the true value by terms involving the measurement signal-to-noise ratios. Clearly $0 \leq \gamma^2_{xy}(f) \leq 1$. In the absence of any system nonlinearities the ratio $\gamma_{xy}/1-\gamma_{xy}$ can be interpreted as the signal-to-noise ratio at the output. Alternatively, for a noise free system $\gamma_{xy}/1-\gamma_{xy}$ can be interpreted as the linear-to-nonlinear ratio [37]. In practical measurement systems the various spectra are averaged over a sufficiently large number of samples to remove the uncorrelated noise terms.

In the present experimental study the coherence function was applied to the systems shown in Fig. 8 to determine the degree of linear dependence of the response on the measured differential pressures Δp. Several preliminary remarks are in order before the computational procedure and the results are detailed.

1. From the physics of the phenomenon it is apparent that sustained vibration of the window system cannot be expected. Hence selected sample records need to be used to compute the coherence function.

2. The sample records should be such that the response signal-to-noise ratio is considerable, i.e. the response amplitude should be above the noise floor of the measurement and data acquisition system.

3. Such a selection can be accomplished by triggering the data input to the Fourier Analyzer using the pressure (or response) signal.

4. Sorting the data as in 3, it was found, restricts the number of sample records that can be extracted from an hour long data record with stationary wind characteristics. Alternatively, therefore, visual inspection and sorting as described in Chapter IV can be used.

5. For inputs which are not triggered in (this applies to the processing equipment used and other similar analyzers) overlap processing of the data can be used to reduce the estimation errors in the coherence function [52]. This estimation technique consists of applying the FFT operation to overlapped data segments. The result is a reduced variance at the expense of the number of FFT's to be performed, i.e. computational time. Overlap processing is readily implemented on the

5451B Fourier analyzer. The overlap fraction can be varied by the addition of a delay loop to the program.

The coherence function was computed from the measured data for the following cases:

1. Coherence between the differential pressure and the internal glass plate displacement, i.e. $\gamma^2_{\Delta p, w_i}$

2. $\gamma^2_{\Delta p, w_e}$

3. $\gamma^2_{w_i, w_e}$

The first two of the above determine the fraction of the response power due to Δp. The function $\gamma^2_{w_i, w_e}$ is used to verify the existence of coupling between the two plates.

All of the previously discussed computational procedures, namely, triggered (without Hanning), free run and overlap processing were utilized to obtain the best possible coherence function estimate for the various signal pairs. Differences in the coherence functions estimated by the four techniques (this includes triggering the input on response) were insignificant and were attributed to inherent uncertainty in the estimation procedures. Overlap processing did smooth the coherence function to some extent although the difference was not substantial to warrant an increase in computation time.

The coherence functions shown in Figs. 32-34 were computed from record segments selected according to the sorting procedures described in Chapter IV. The input was free run, the sample records were disjoint and weighted by a single Hanning function. The high frequency band (0.8-50 Hz) functions were computed from the respective spectra averaged over

400 disjoint segments. The low frequency band (0.03-3 Hz) functions utilized 30 disjoint records. The coherence functions of Figs. 32, 33 are representative of the response dependence on the differential pressure. The actual wind and structural variables shown are for reference purposes only.

Figures 32 a, b and c show the coherence functions $\gamma^2_{\Delta p,w_e}$, $\gamma^2_{\Delta p,w_i}$, and $\gamma^2_{w_e,w_i}$ respectively, together with the input and output spectra, for the high frequency band. Significant values of the coherence functions in Figs. 32a, and b are seen only below 1.7 Hz. The peak values in the two cases of $\gamma^2_{\Delta p,w_e} = 0.26$ and $\gamma^2_{\Delta p,w_i} = 0.35$ at 0.8 Hz differ due to the associated statistical uncertainty. At frequencies above 1.7 Hz there appears to be no causality between the differential pressure and the response. The values of the coherence function between 0.8-1.7 Hz are too small compared to 1.0 and majority of the response power is due to sources other than wind loads. Examination of Fig. 32c reveals similar behavior in $\gamma^2(f)$ up to 3 Hz. From the spectra it can be seen that the root-mean-square value of w_e is higher (at all frequencies) than of w_i. The difference in rms values in the vicinity of 1 Hz is about 6 dB corresponding to a ratio $\frac{w_e}{w_i} = 4$. This difference can be attributed to the compliance of the entrapped air. A high value of the coherence function $\gamma^2 = 0.7$ indicating extremely good causality is seen at 11.5 Hz which is close to the natural frequency for inphase motion of the two plates in the (1, 1) mode calculated from the model (Table 5). However, Figs. 32a and b do not show any pressure-to-response causality at this frequency. This implies that the vibratory motion of the window is due to sources other than the wind loading. The internal

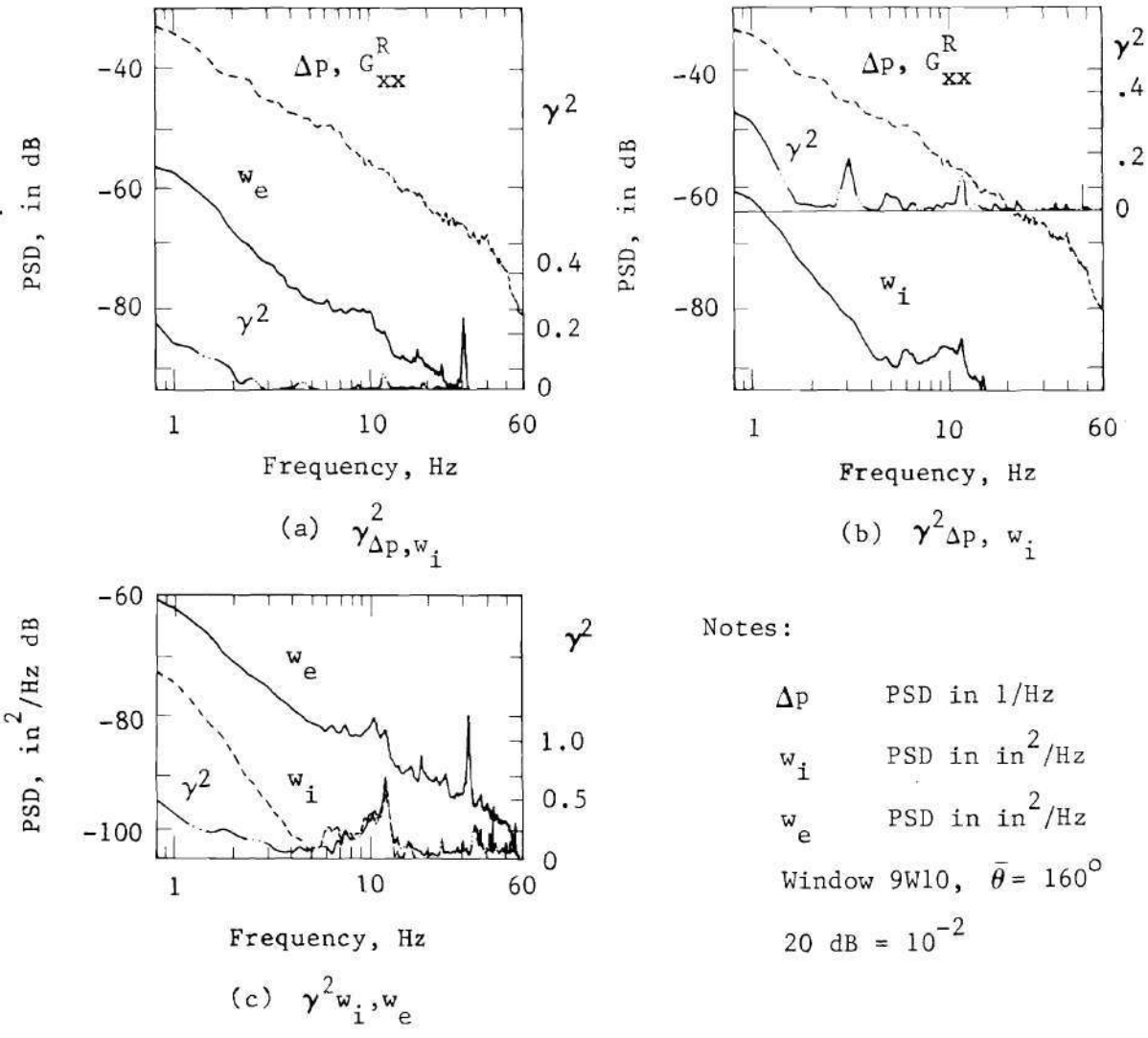

Figure 32. Measured Coherence Function, High Frequency Band

glass plate response rolls-off much faster than the external plate response at frequencies above 1 Hz. A strong peak in w_e is seen at 31 Hz and compares with the calculated (3, 1) inphase motion frequency. A corresponding peak in w_i is not so obvious. The coherence function at this frequency is of the order of 0.26. An explanation for the discrepancy at 31 Hz is that the peak is fictitious and not due to glass plate motion. The frequency could have been introduced in the signal due to floor vibrations arising from rotating machinery used in building services (generally 1800 rpm motors). The LDM being more sensitive to floor vibrations, the frequency shows up prominently in w_e. The erroneous coherence function value is typical of the false coherence case described in Ref. 31.

Figures 33a, b, and c show the coherence functions in the low frequency band (0.03-3 Hz) corresponding to the data used in Fig. 32. This low frequency loading can be assumed to be quasi-static. Excellent causality between pressure and response is seen up to 0.6 Hz from Figs. 33a and b. This leads to the conclusion that the "static" response of the window systems is largely due to pressure loads. It is noted here that since only the differential pressure was measured and the internal pressure contributes to the quasi-static differential, a distinction as to the source of the pressure loads cannot be made from the data collected, in this low frequency range.

The roll-off of w_e and w_i spectra, as seen from Fig. 33c is almost identical up to 1 Hz and the difference in spectrum levels at 1 Hz is approximately 12 dB corresponding to a ratio $\frac{w_e}{w_i} \simeq 4$.

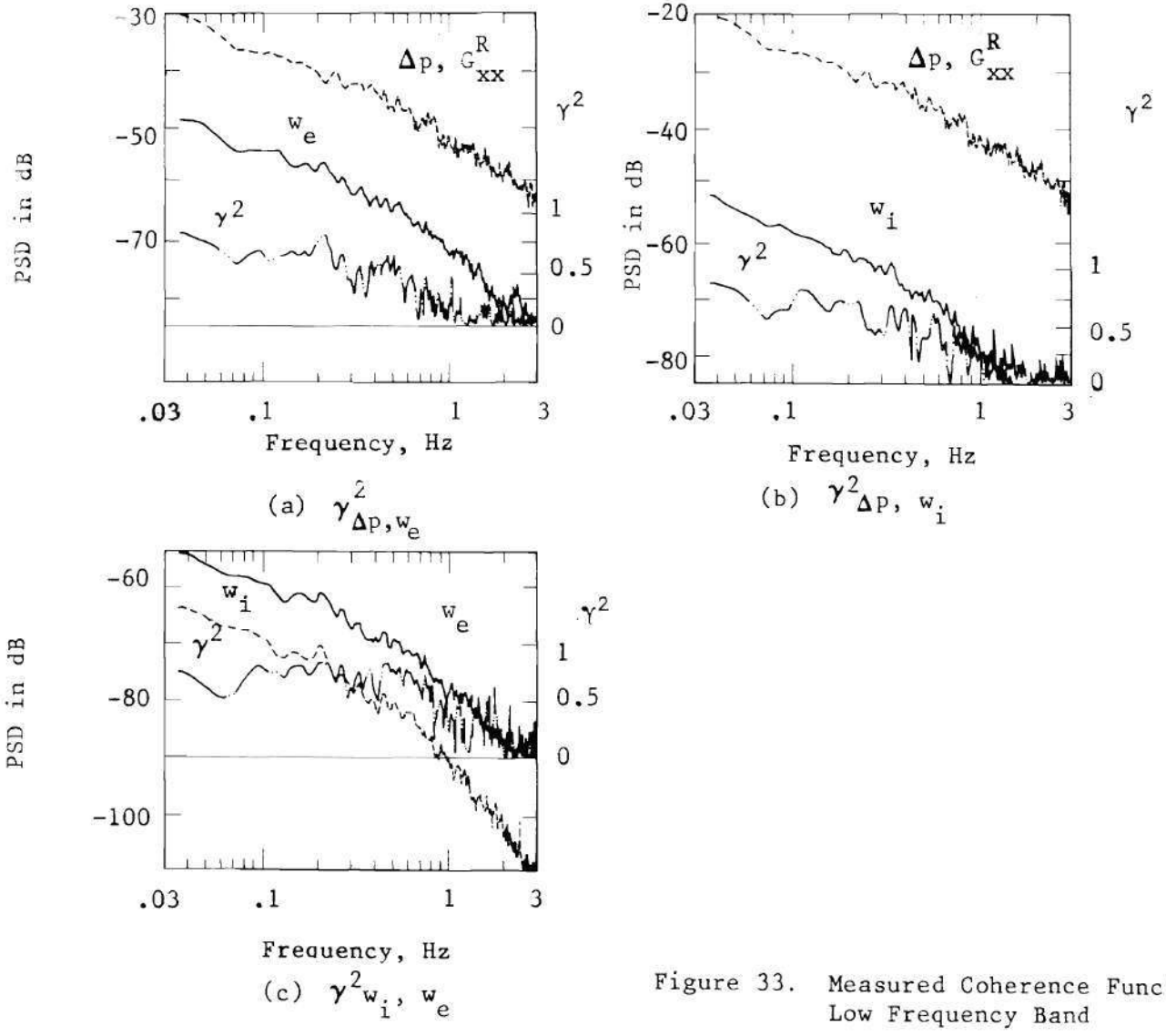

Figure 33. Measured Coherence Function, Low Frequency Band

Figure 34 shows the high frequency band spectra and coherence functions for a case which differed markedly from the representative response spectra and coherence function. The difference is seen in the frequency band extending from 6-16 Hz, where the coherence function is very close to 0.5. Considering the statistical variation in the estimates this is within the 95% confidence limits of true $\gamma^2 = 0.5$. The pressure spectrum shows a bulge between 6-8 Hz indicating that the wind pressure is responsible for the response at these frequencies. Since the window at which these data were measured was on the 9th floor, the relatively high frequency response is possibly due to gust effects.

The coherence function, as has been demonstrated, serves to identify the response levels associated with the wind or pressure loads. Several features of the window response dependence on wind loads are now apparent. High coherence between the input and output up to 1 Hz shows that the "quasi-static" response of the glass plates is primarily due to pressure loading. Beyond 1 Hz the coherence value decreases and becomes insignificant for frequencies less than 1.7 Hz. In the region from 1 to 1.7 Hz the values of the coherence function are in the vicinity of 0.25 implying that pressure loads may no longer be the sole excitation source. Interpretation of the coherence function at resonant peaks requires that care be exercised so as to isolate false coherence which may be due to an extraneous source affecting both the input and the output. At the fundamental frequency of 11.5 Hz (for window W10 on the 9th floor) which appears in the response spectrum the coherence between the pressure and the response is extremely low. Therefore, the fundamental frequency is excited by sources other than the wind loading. In some

Notes:

Δp PSD in 1/Hz

w_i PSD in in^2/Hz

w_e PSD in in^2/Hz

Window 9N4, $\bar{\theta} = 160^\circ$

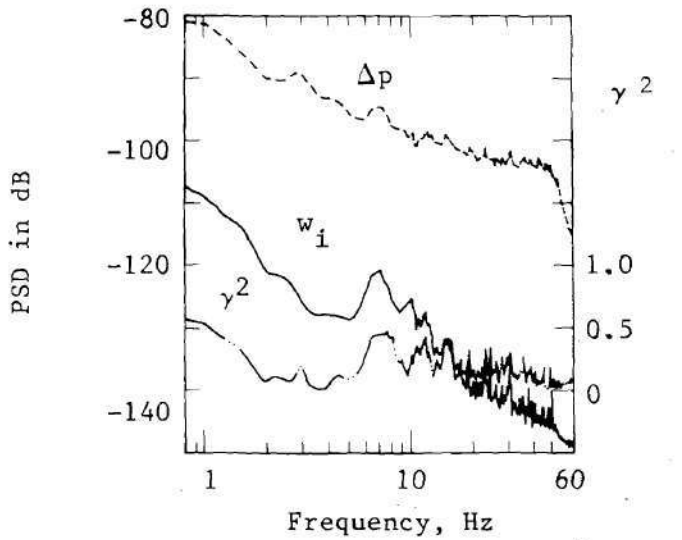

(a) Input Δp, Response w_i, $\gamma^2 \Delta p$, w_i

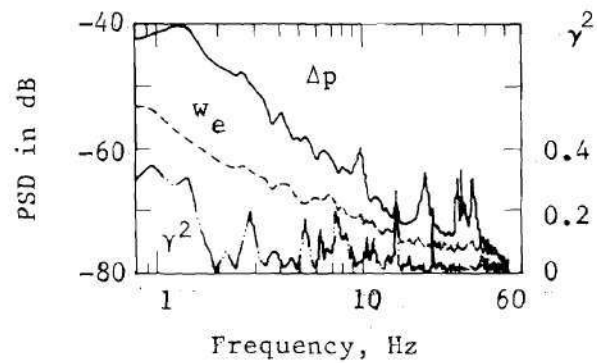

(b) Input Δp, Response w_e, $\gamma^2 \Delta p$, w_e

Figure 34. Measured Coherence Function, Window 9N4, $\bar{\theta} = 160^\circ$

instances the fundamental was also seen in the pressure spectra yielding a coherence of almost unity (it is noted that for purely sinusoidal signals the coherence function can only be 0 or 1). This was diagnosed as a typical false coherence since the fundamental was strongly excited and appeared, by way of motion of the pressure tap located on the support and/or feedback of panel vibrations to the flow, in the pressure spectra. False coherence also appears to be the reason for the high coherence function values seen at 31 Hz. This frequency corresponds to the rpm of some rotating machinery in the building.

The isolated case of Fig. 34 demonstrates that high values of the coherence function in the high frequency band may occur for a particular combination of the building profile and flow characteristics. In this case the wind loads are capable of exciting window dynamic response, in a relatively narrow frequency band extending from 6-16 Hz. In view of these observations the hypothesis of "critical response locations" appears more realistic.

System Identification

In Chapter II it was envisaged that the measured ambient wind loading and the induced dynamic response could be used to estimate the transfer function of the window system. The estimated frequency response functions were to be used in identifying the modal properties of the double plate system and the support transmissibility. The "inverse" problem thus posed is that of obtaining a mathematical model for the window system from measured data, and is labeled system identification. A survey of system identification techniques in structural dynamics is

presented in Ref. 53, and application of transfer function based identification techniques is dealt with in Refs. 54, 55, 56, 57. However, recapitulating the results of Chapter IV and the previous section, it is seen that the dynamic wind loads (i.e. loading in a spectral bandwidth spanning the first few natural frequencies of the plates, say from 5-30 Hz) are extremely small in magnitude and do not bear significant causality for the window dynamic response. The low values of the coherence function at higher frequencies have another important implication. As mentioned in Chapter II, the coherence function is a measure of the validity of the transfer function estimates. It is evident, therefore, that at higher frequencies the transfer function of the window system cannot be estimated from ambient data.

An examination of the response levels form the w_i and w_e spectra shown in Figs. 32-34 reveals that the response of the double plate system is essentially quasi-static*. This characteristic of the measured window response provides an increased confidence in the measured wind load spectra which were also seen to be quasi-static. It can be concluded, therefore, that at the locations where the measurements were conducted, the wind loads do not possess sufficient energy to excite window vibrations. The mullion acceleration response spectra and its coherence function were also computed and are shown in Fig. 35. As can be anticipated, estimation of the transmissibility function from these data is not possible.

---

* Response period large compared to the period of the fundamental.

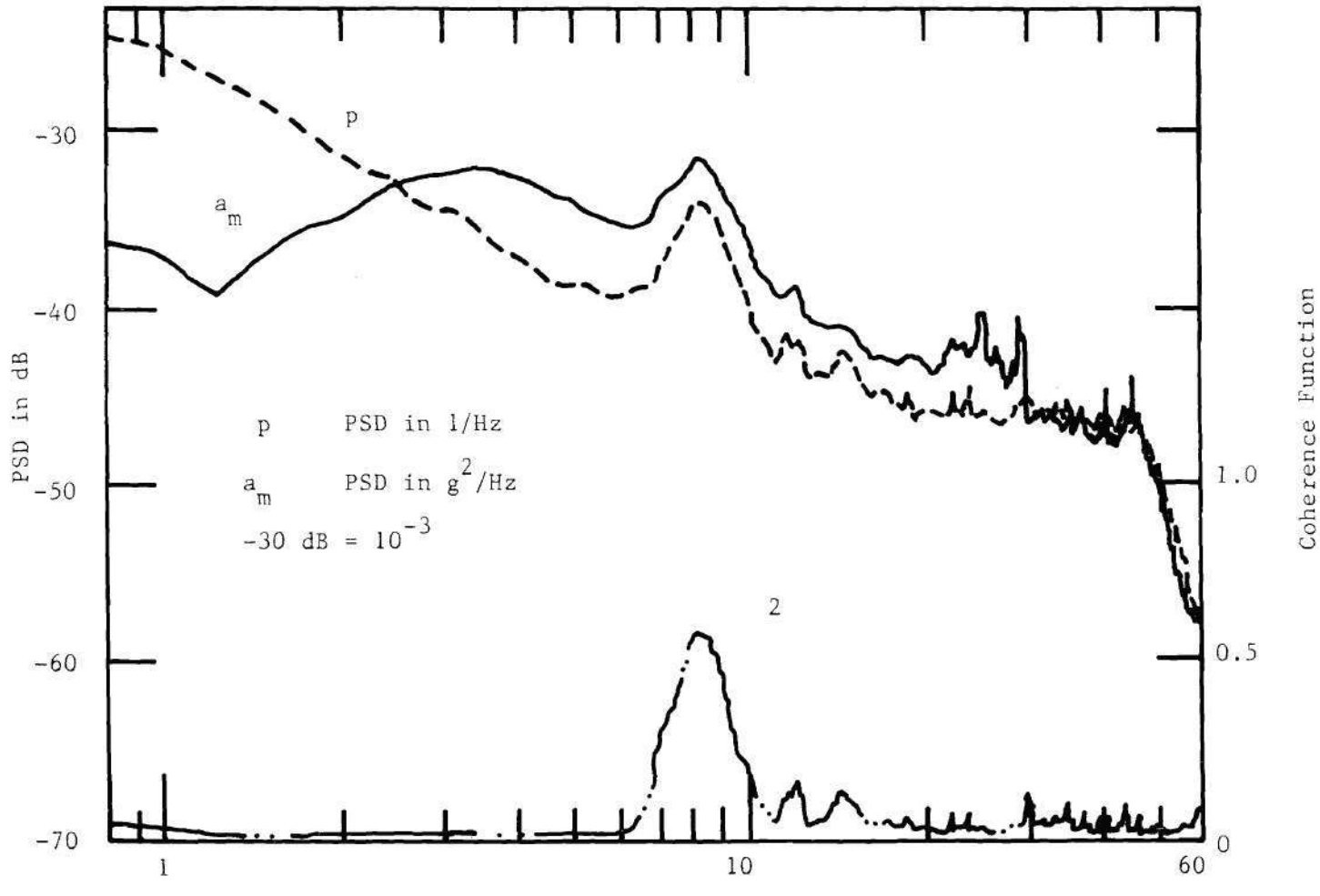

Figure 35. Mullion Acceleration Response Spectrum and Coherence Function

Identification of the modal parameters and the transmissibility function of the window system by forced excitation was, therefore, considered. These measurements could have been performed in a laboratory on a full scale window unit from the curtain wall, mounted in a test facility already designed and built [59]. However, the need for in-situ measurement of the dynamic cahracteristics of window units arises because of the following features:

(a) The dynamic characteristics of the window unit depend on the nature of its installation and the fact that it is affected by adjoining elements of the curtain wall. It would be unrealistic to simulate the entire curtain wall. In addition, any significant resonant frequency variation from one window to another can be treated as indicative of the variation in installation characteristics. A correlation between the frequency variation and the nature of the installation would enable detection of a faulty installation - during assembly of the curtain wall or at a later time in its service life when structural degradation might have occurred.

(b) Measured transmissibility function for a window provides an estimate of the support force attenuation arising from the presence of the rubber gasket. The transmissibility function can, therefore, be used to assess the quality of the gasket.

(c) In-situ dynamic measurements such as the resonant frequencies and the damping characteristics can be used towards an improved laboratory simulation.

Considering these factors, the dynamic properties of a window in an actual curtain wall were determined from forced excitation tests. The

measured dynamic properties include:

(a) Variation in the resonant frequency (only the 2, 1 mode) of windows on a flat building face.

(b) The resonant frequencies of a single window unit (up to 6 modes) and the damping coefficients in each of these modes.

(c) Transmissibility function for a single window.

Dynamic Properties by Impulse Testing

Various types of excitations can be used to measure structural frequency response functions. Excitation techniques utilizing broadband random, pseudo-random, and transient inputs in conjunction with digital processors such as the Fourier Analyzer provide faster measurements as compared with traditional sinusoidal excitation.

A simple method of performing transient tests is to use a hand held hammer, with a load cell mounted on it, to impact the structure and measuring the response to this transient excitation. The impulsive input has a flat frequency spectrum whose bandwidth depends on the "hardness" of the impacting head. A harder head providing a larger bandwidth. The transfer function computed from such an input-response pair can be used to determine the resonant frequencies and the damping coefficients. Multipoint measurement of the transfer function, i.e., computation of the transfer function between various excitation and response points can be used to determine the mode shapes corresponding to these frequencies. The modal mass and modal stiffness can also be estimated from the transfer function data, although this almost invariably requires some type of data fitting [56].

Measurement of the frequency response functions for the present application to window systems was directed at obtaining the resonant frequencies f_n, the viscous damping coefficient ζ, the mode shapes of the inner plate, and the transmissibility function. The mode shapes of the outer glass plate were not obtained since multiple point response measurements by the LDM proved time consuming and inconvenient. However, results of the analytical model of the window system are used to obtain some idea of the double plate mode shapes corresponding to measured frequencies. In addition, the transfer function between w_i and w_e provides the vibration phase angle between w_i and w_e at the resonant frequencies and, therefore, the nature of the motion.

The procedures described below for the estimation of the vibration parameters are based on the following assumptions:

(i) The modes of the system are widely spaced in frequency.

(ii) Although modal coupling exists, a lightly damped multi-degree-of-freedom system can be closely approximated by a single-degree-of-freedom system of appropriate natural frequency and damping near each of the system's natural frequencies.

The modal properties of the double plate system and the transmissibility function are presented in the following sections.

Modal Parameters

The inner plate of the window was marked at 3 spatial locations as shown in Fig. 36. The outer plate response was monitored at a single point 2' corresponding to point 2 of the inner plate. An accelerometer was used to measure the response at 2 and its location was fixed. The

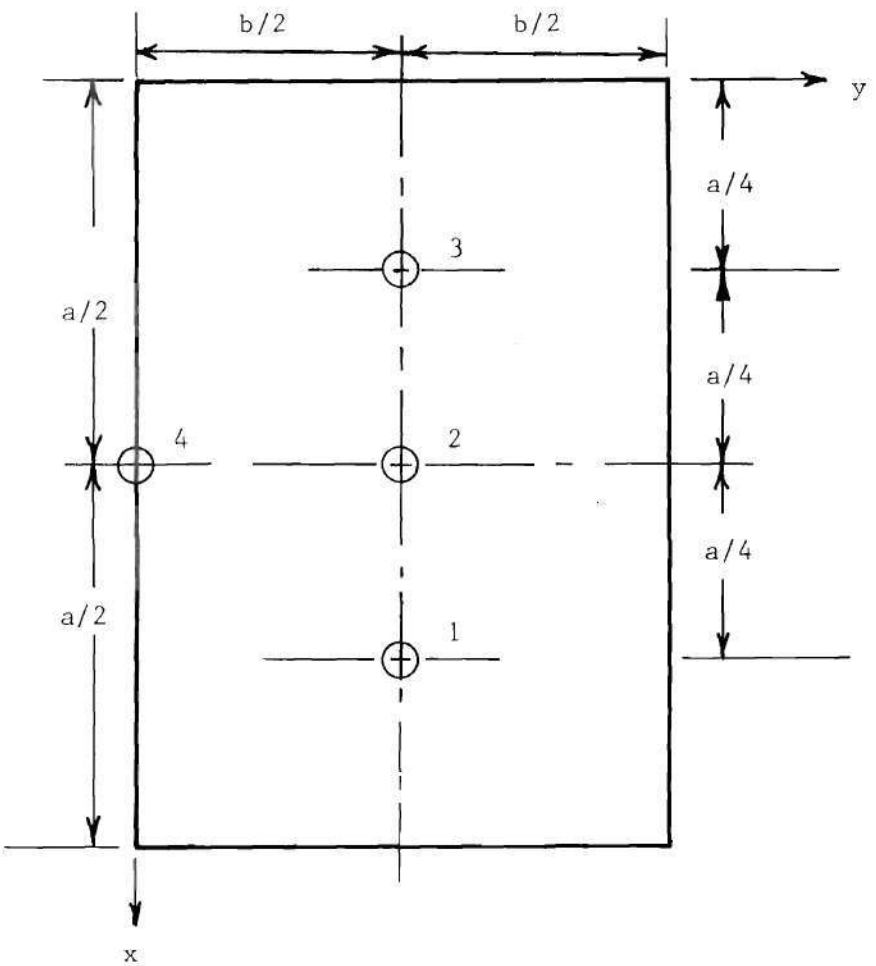

Figure 36. Location of Accelerometers on the Inner Plate

LDM measured the displacement response at point 2'. An instrumented hammer was used to excite the inner glass plate at each of the 3 points. Transfer functions for these 3 cases were computed from the measured response. The measured transfer functions $H_{2i}(f)$, $i = 1, 2, 3$, are the elments of the second row of a 3 x 3 transfer function matrix. It can be shown [56] that only a single row or column of the transfer function matrix needs to be measured to compute the modal amplitudes at the 3 points. The LDM output provides the natural frequencies of the outer plate.

The compliance of the hammer head was adjusted to provide a bandwidth of 50 Hz. The spectrum of the impulse is shown in Fig. 37. The tests were conducted on window N4 on the 28th floor. The frequency response functions for the inner plate shown in Figs. 38 through 40 were used to obtain the X-axis mode shapes. Figure 41 shows the $H_{2',1}(f)$ transfer function of the outer plate.

The modal parameters are computed from these transfer functions as follows:

Resonant Frequencies. The acceleration-to-force transfer function is called inertance whereas the displacement-to-force transfer function is called compliance. In inertance or compliance plots the natural frequency corresponds to the following transfer function characteristics:

(a) Peak of the magnitude of the transfer function

(b) Phase angle of 90^{o}

(c) Zero of Re H(f)

(d) Peak of Im H(f)

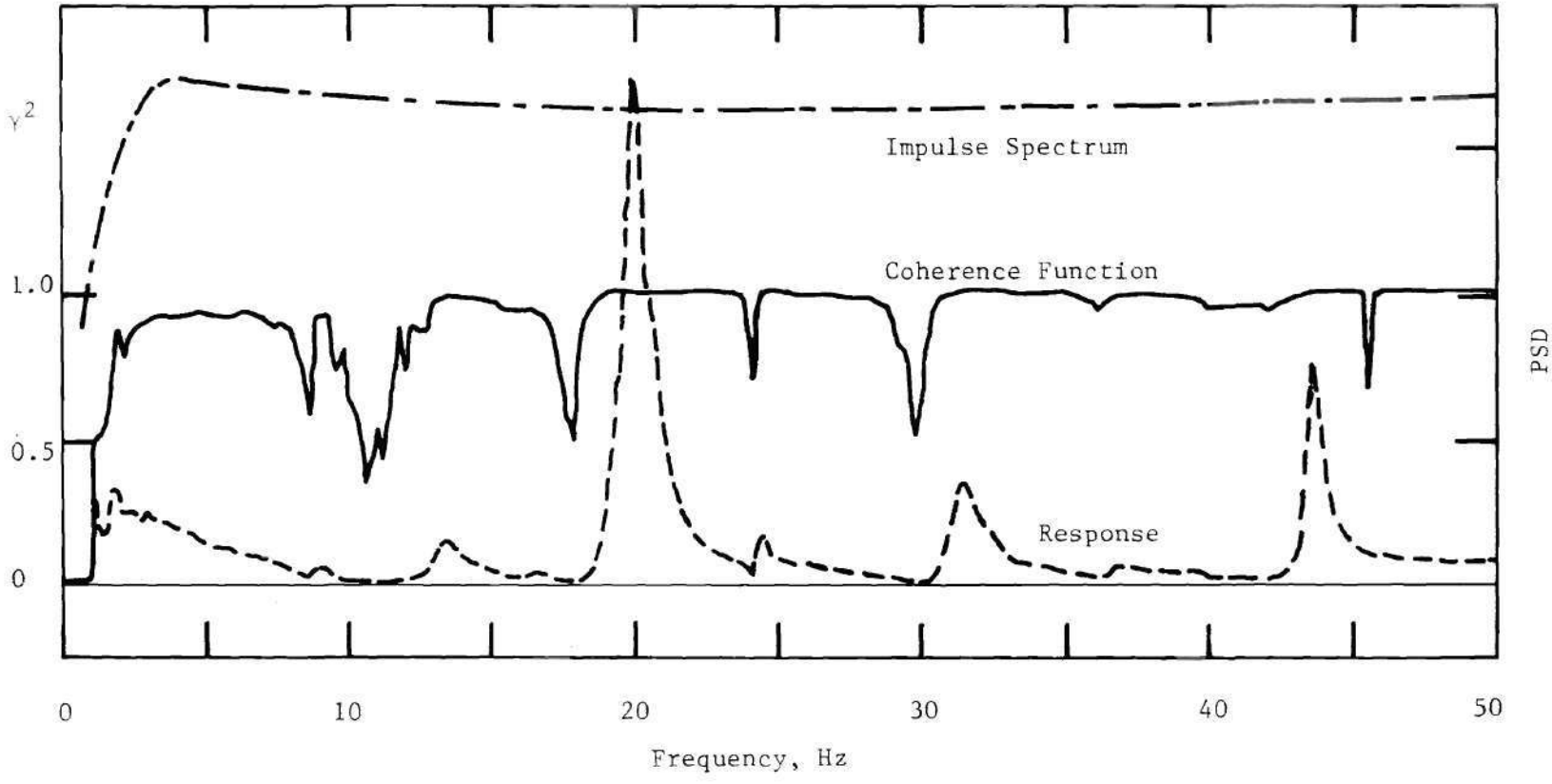

Figure 37. Spectrum of the Impulse, Response and Their Coherence Function

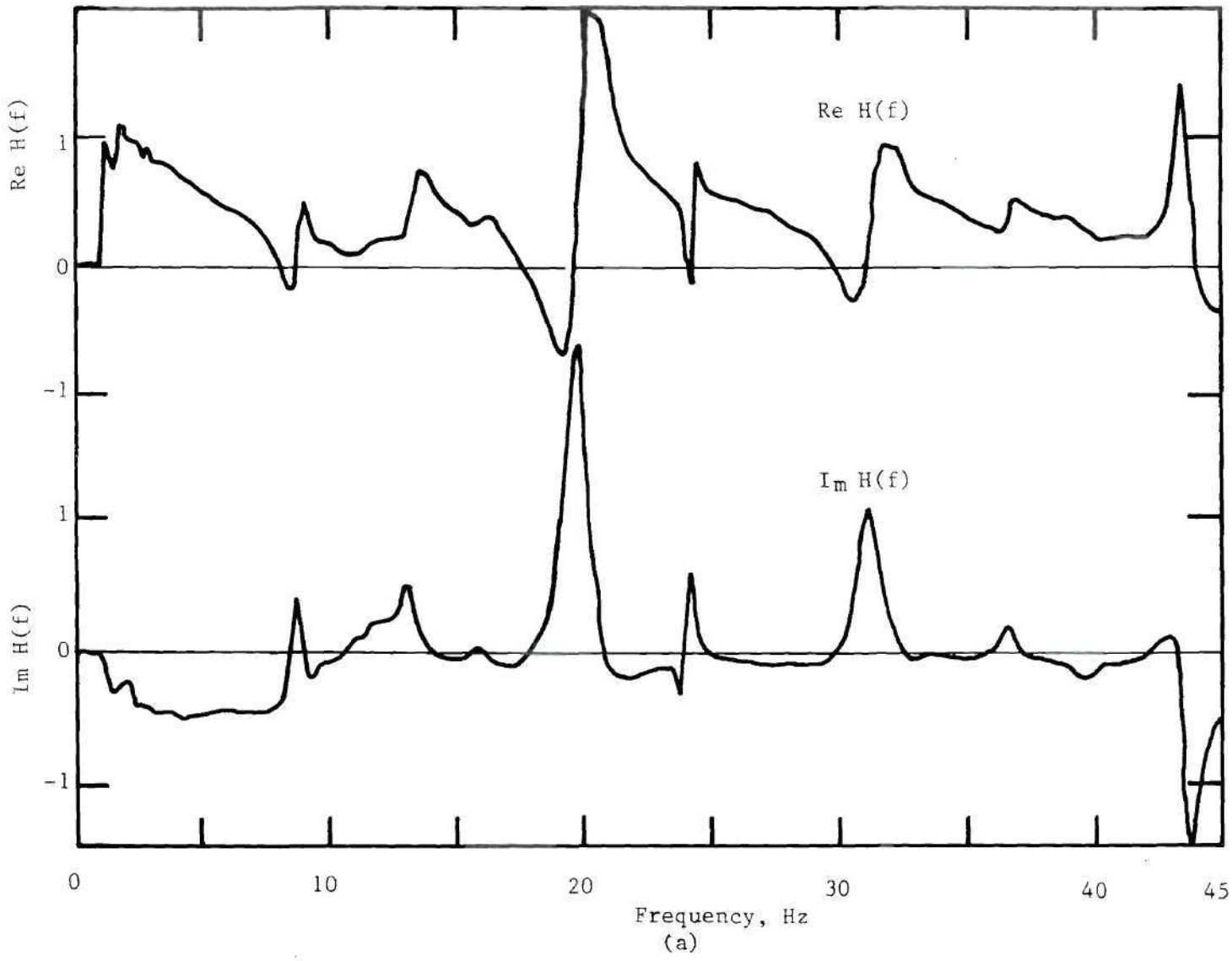

Figure 38. Frequency Response Function: Impact at 1, Response at 1

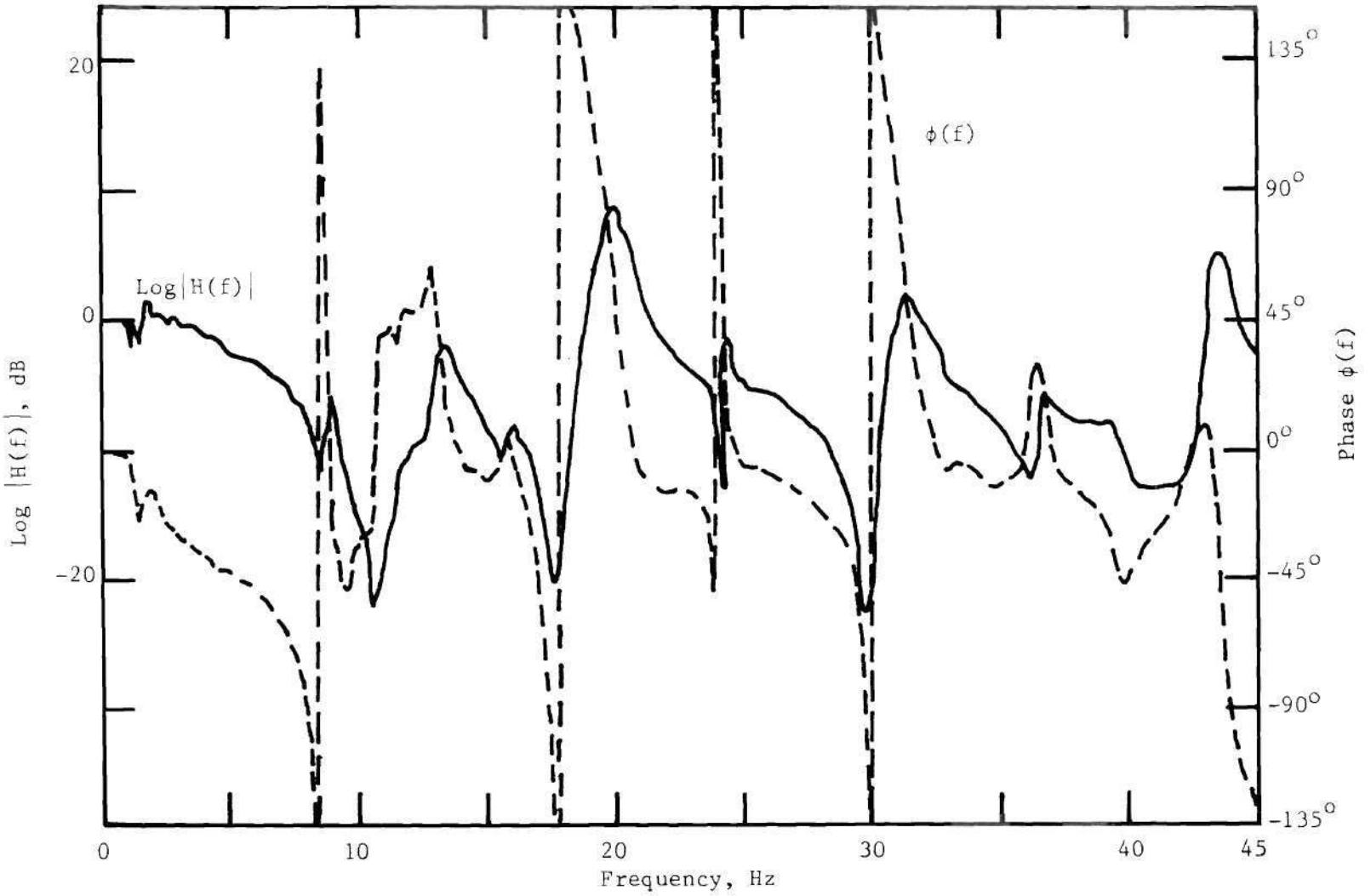

(b)

Figure 38. Frequency Response Function: Impact at 1, Response at 1

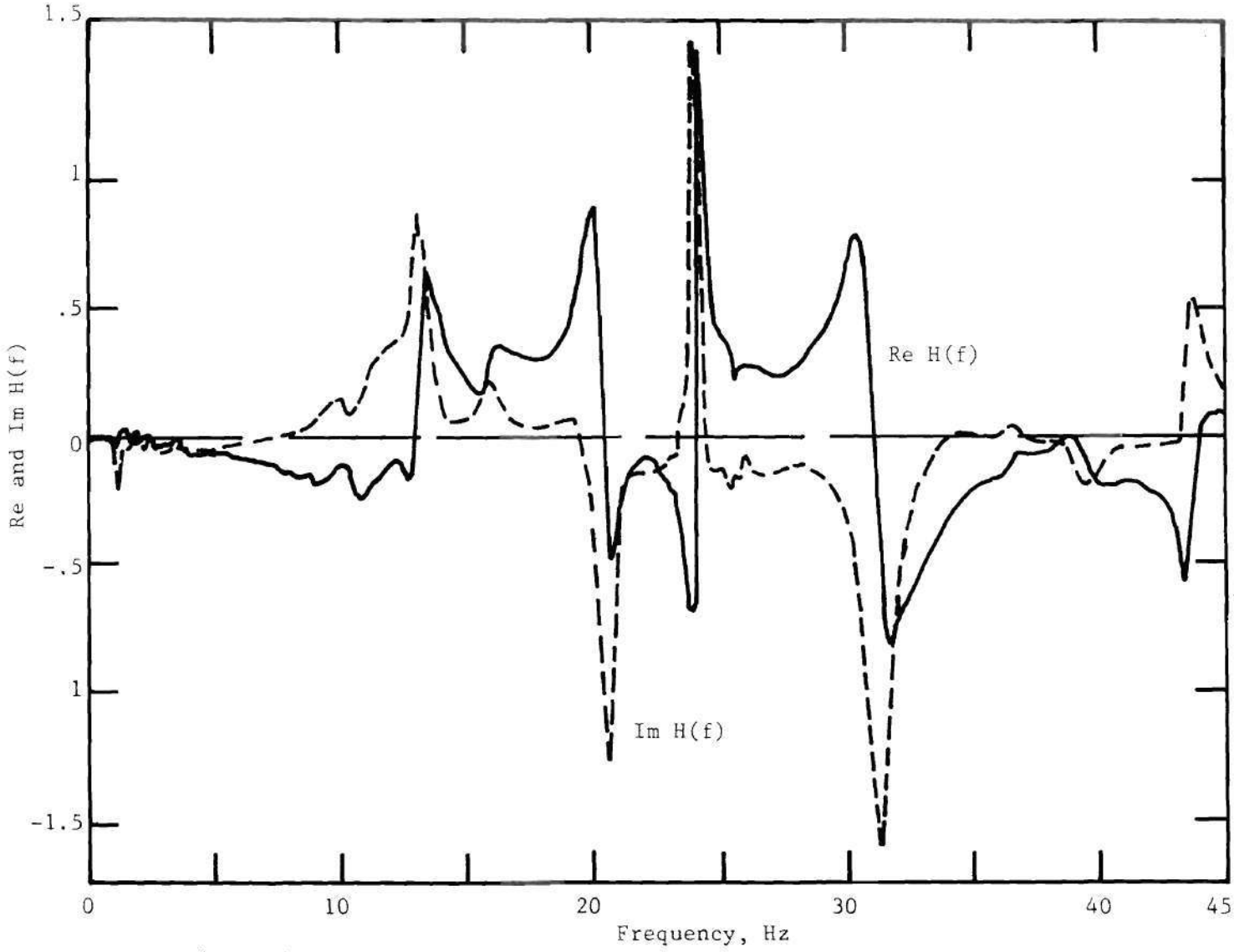

Figure 39a. Frequency Response Function: Impact at 2, Response at 1

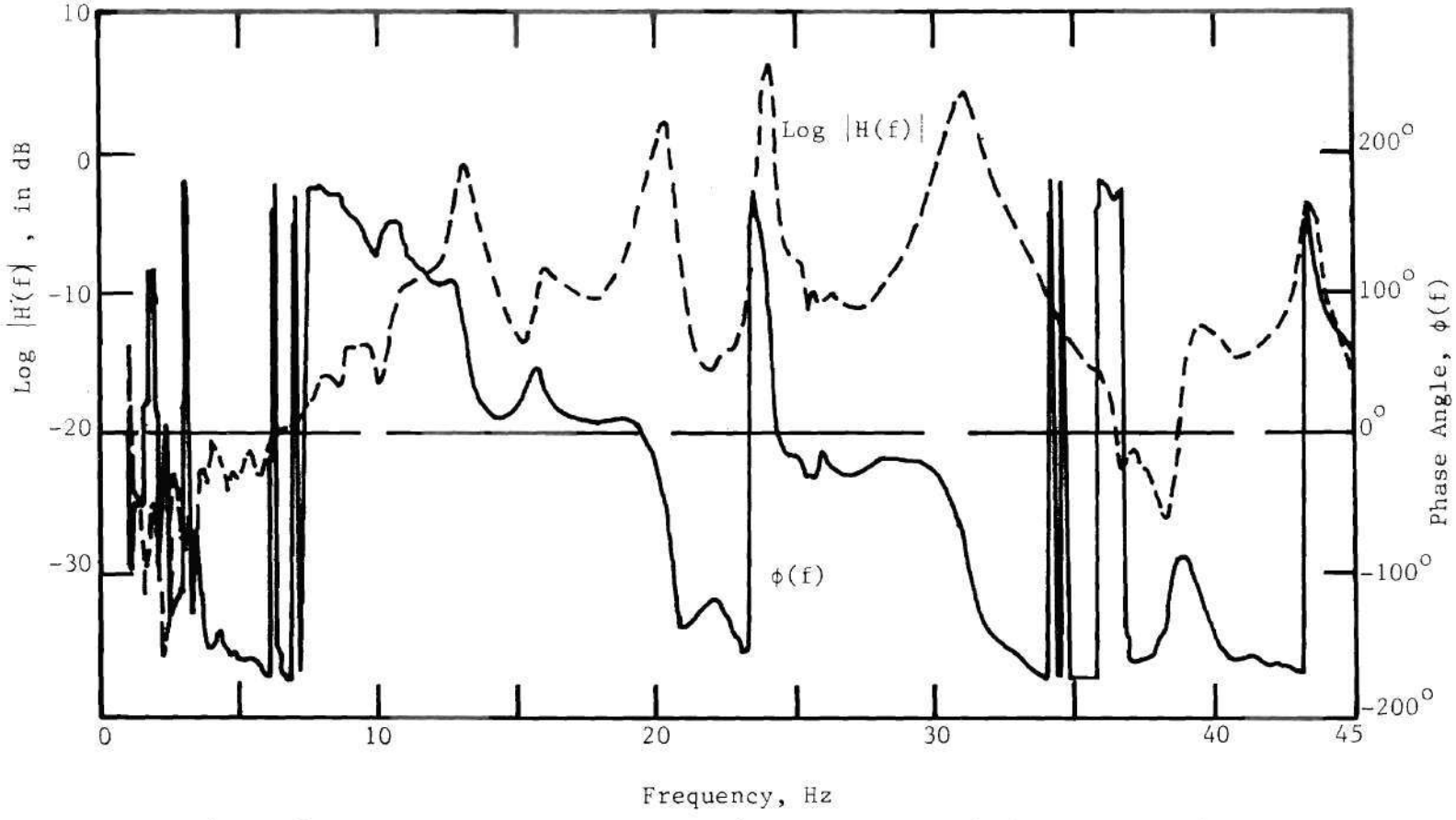

Figure 39b. Frequency Response Function: Impact at 2, Respones at 1

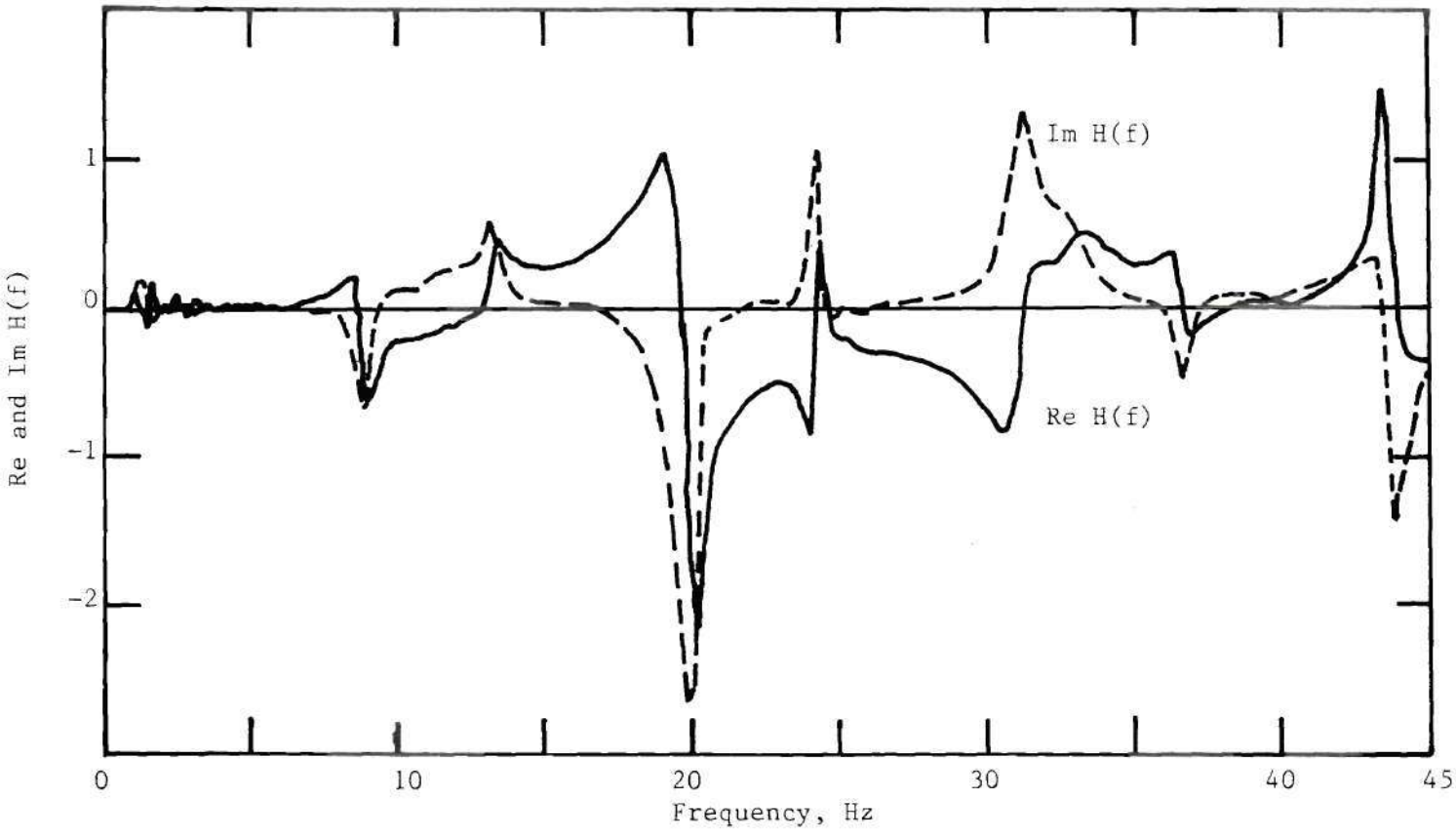

Figure 40a. Frequency Response Function: Impact at 3, Response at 1

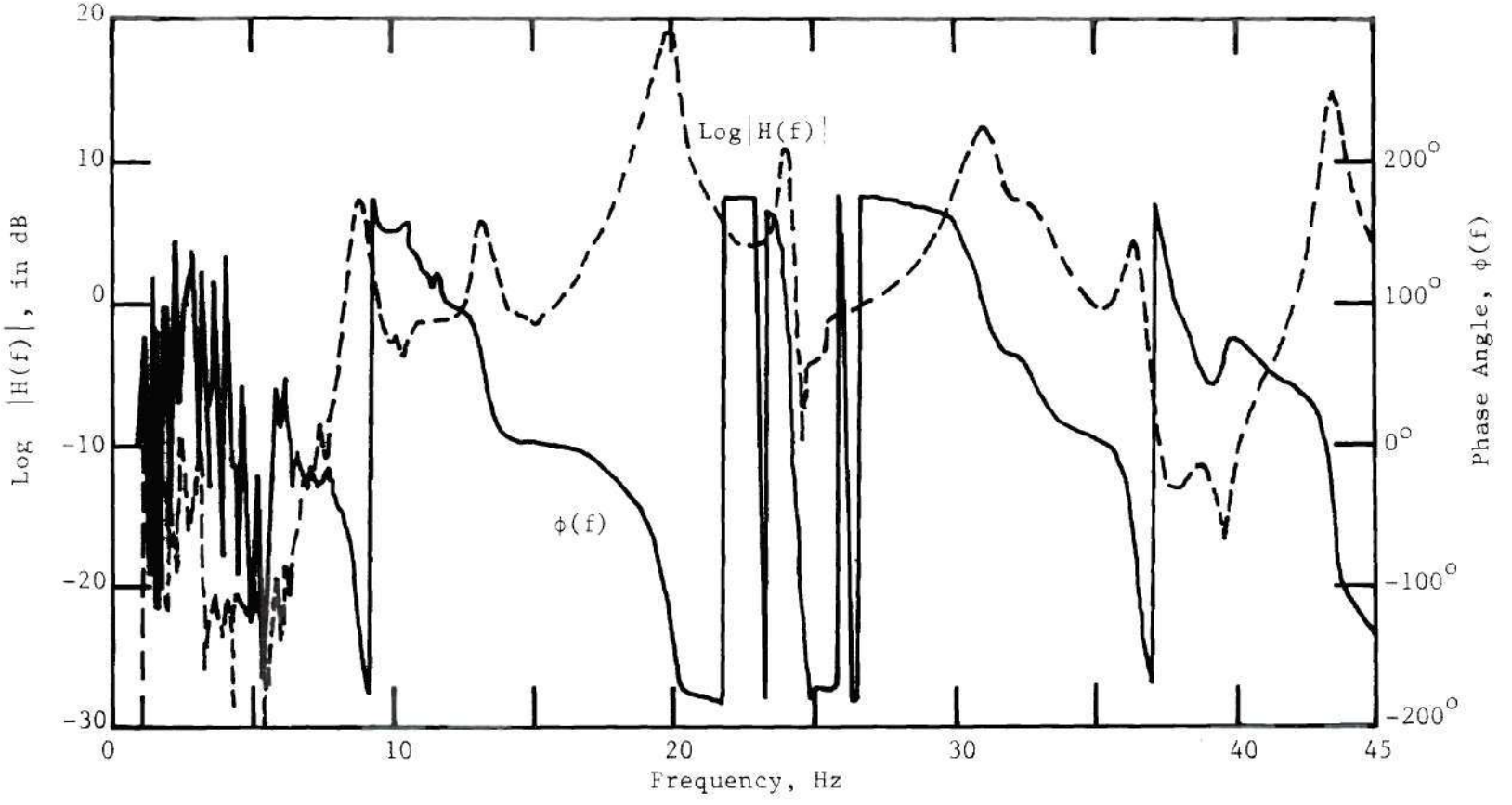

Figure 40b. Frequency Response Function: Impact at 3, Response at 1

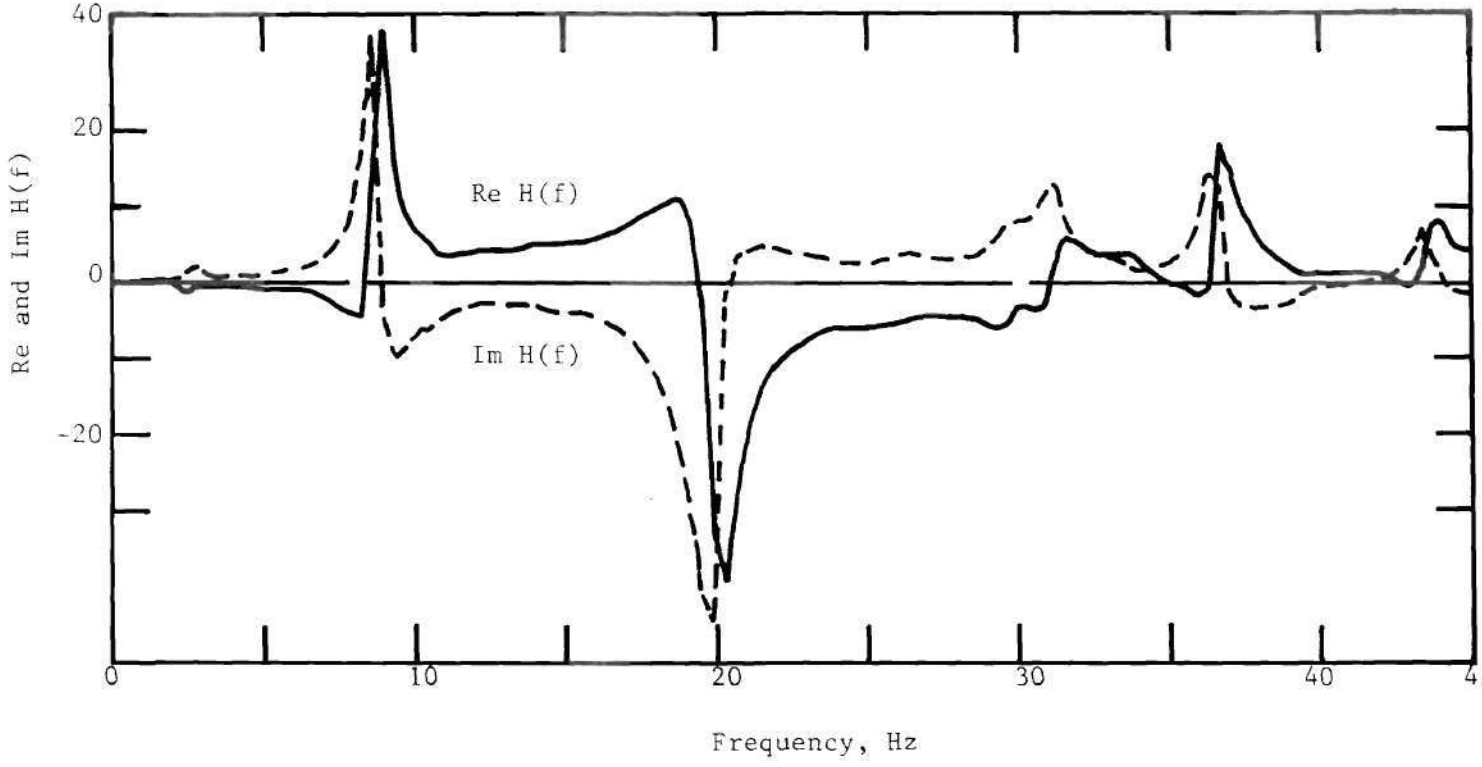

Figure 41a. Frequency Response Function: Impact at 2, Response at 2'

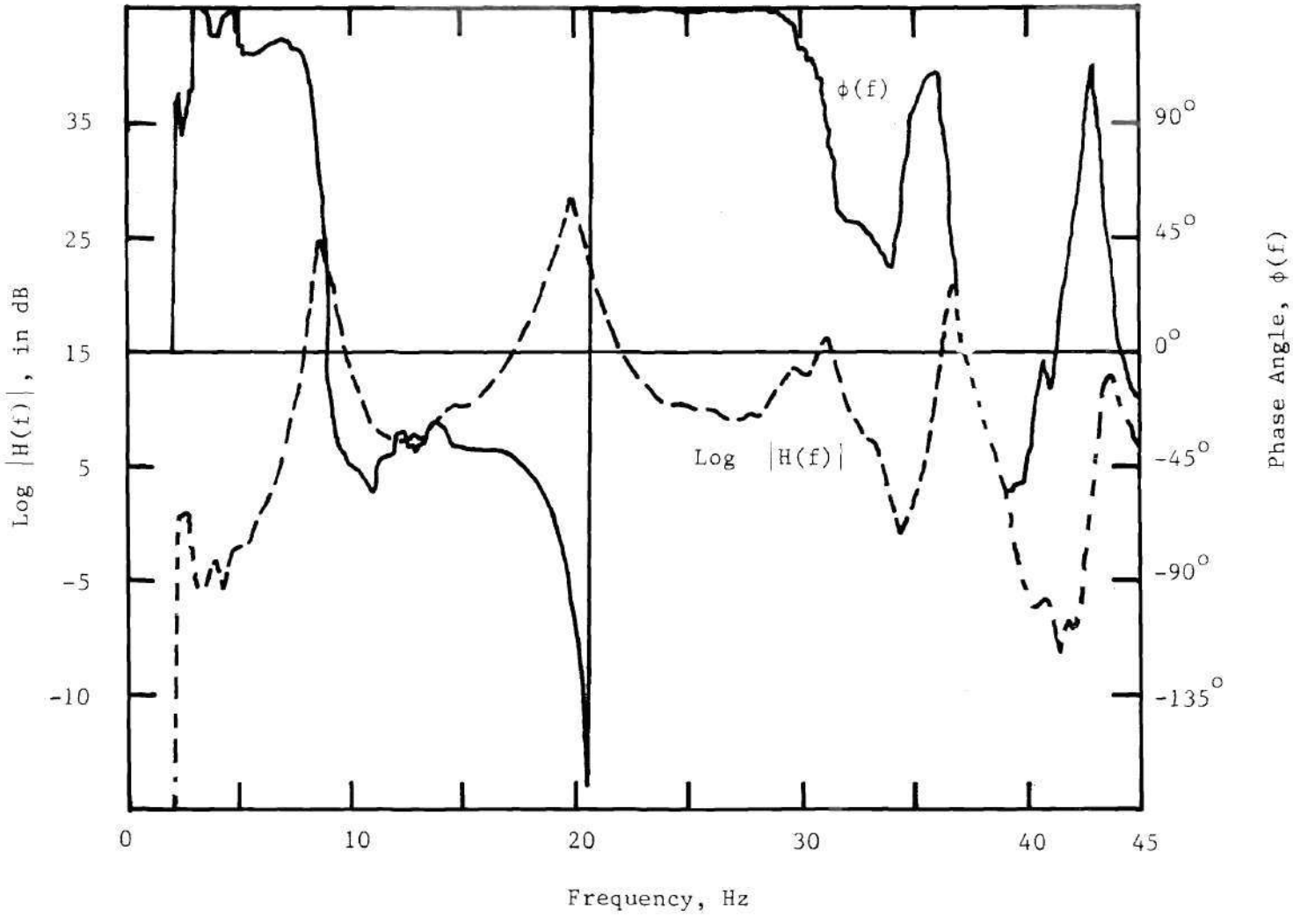

Figure 41b. Frequency Response Function: Impact at 2, Response at 2'

Damping Coefficient. Several techniques for estimating the damping coefficient from the measured transfer function are available. Vector or Nyquist plots of the frequency response function, where the real and imaginary parts of the transfer function are plotted in the complex plane, can be used to estimate the modal damping [58]. However, in practice estimation of damping form these plots requires careful curve fitting.

Damping can be measured with greater precision using the amplification factor Q defined as:

$$Q = \frac{1}{2\zeta} \tag{73}$$

Q may be measured from the frequency response functions as follows:

$$Q = f_n/\Delta f_n \tag{74}$$

where Δf_n ~half-power bandwidth of the resonance peak corresponding to f_n.

Alternatively, a method based on features of the real and imaginary response spectra can be used to estimate Q:

$$Q = \frac{(f_a/f_b)^2 + 1}{(f_a/f_b)^2 - 1} \tag{75}$$

where

f_a = Frequency above resonance, where the real part of compliance or inertance reaches a peak

f_b = Frequency below resonance, where the real part of compliance or inertance reaches a peak of opposite sign.

Mode Shape. The mode shape is estimated by measuring quadrature (imaginary) response values from all of the measured inertance or compliance functions at each resonant frequency. The N mode shapes are normalized with respect to the maximum value of the quadrature component at each of the N natural frequencies.

Applying these techniques to the transfer functions of Figs. 38 through 40, Table 6 was obtained. The corresponding mode shapes are shown in Fig. 42. The natural frequencies of the outer glass plate are shown in Table 7. The resonant frequencies were determined from condition (a) stated above and (b), (c), and (d) were used for verification. The damping coefficient was determined in accordance with Eq.(75).

The (2, 1) mode (corresponding to the results of Table 5 determined analytically) resonant frequency was determined for each of the 12 insulating windows on the north face at the 28th floor. These are shown in Table 8.

The 24% discrepancy between the calculated and measured value of the fundamental frequency may be due to the difference in the actual and modelled support conditions. The support conditions in reality are intermediate between clamped and simple supports. In addition, due to the presence of the neoprene gasket which is viscoelastic, the boundary conditions may be time dependent.

Transmissibility Function

The acceleration transmissibility defined as the magnitude of the

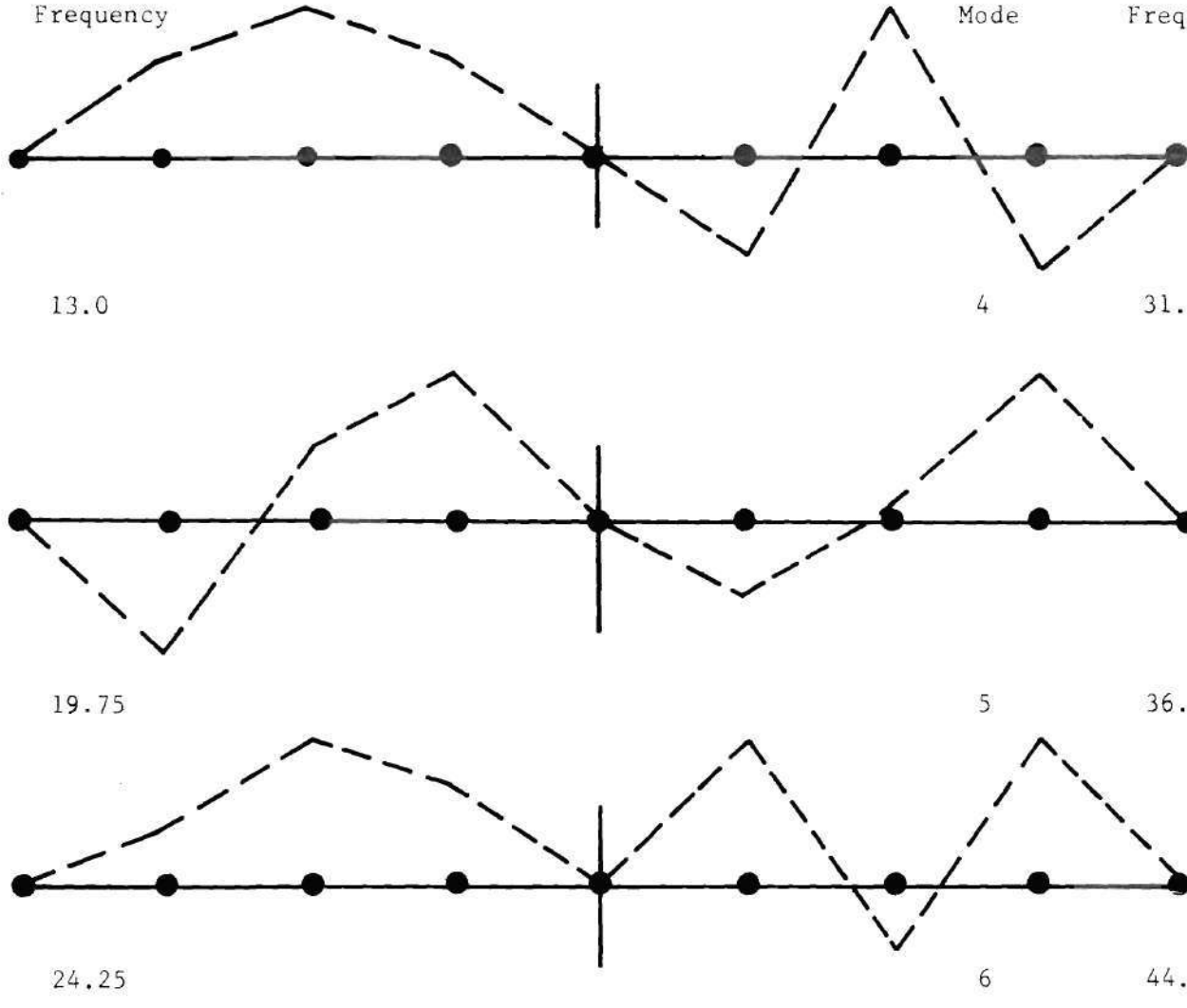

Figure 42. Mode Shapes

Table 6. Longitudinal Modes, Window 28N4, Inner Plate

Mode #	Resonant Freq. H_z	Damping Coeff. ζ	Mode Shape i.e. n =
1	13.0	.045	1
2	19.75	.028	2
3	24.0	.01	1
4	31.25	.02	3
5	36.5	---	2
6	44.0	.01	3

For plotted mode shapes see attached figures.

Table 7. Resonant Frequencies of Outer Glass Plate

Mode #	Frequency, f_n
1	----
2	20.75
3	31.0
4	36.75
5	43.75

Table 8. Variation in Resonant Frequency (2, 1) Mode

Window (Fig. 18)	Frequency, Hz
N1	18.5
N2	19.25
N3	19.25
N4	19.75
N5	18.25
N6	19.0
N7	18.5
N8	19.25
N9	18.5
N10	18.25
N11	21.25
N12	21.25

ratio of acceleration at the midpoint of the plate to the rigid body acceleration of the support was measured. Referring to Fig. 36 the magnitude of the ratio of acceleration at 2 to that at 4 was computed for an impulse applied by the hammer at point 2. The transmissibility is shown in Fig. 43.

For comparison the transmissibility of a damped simply supported plate determined analytically from a relation given in Ref. 32 was computed for damping factor ζ values of 0 and 0.1. The natural frequencies of the SS plate are different, however, the transmissibility magnitude compares in level with that for a damping factor of 0.1 for the fundamental mode. It is realistic to assume that the damping in the double plate window unit is largely due to the rubber gasket around the periphery at the supports. Therefore, a transmissibility measurement on actual window installations would reflect the quality of the gasket and whether gasket roll out from the supports was imminent.

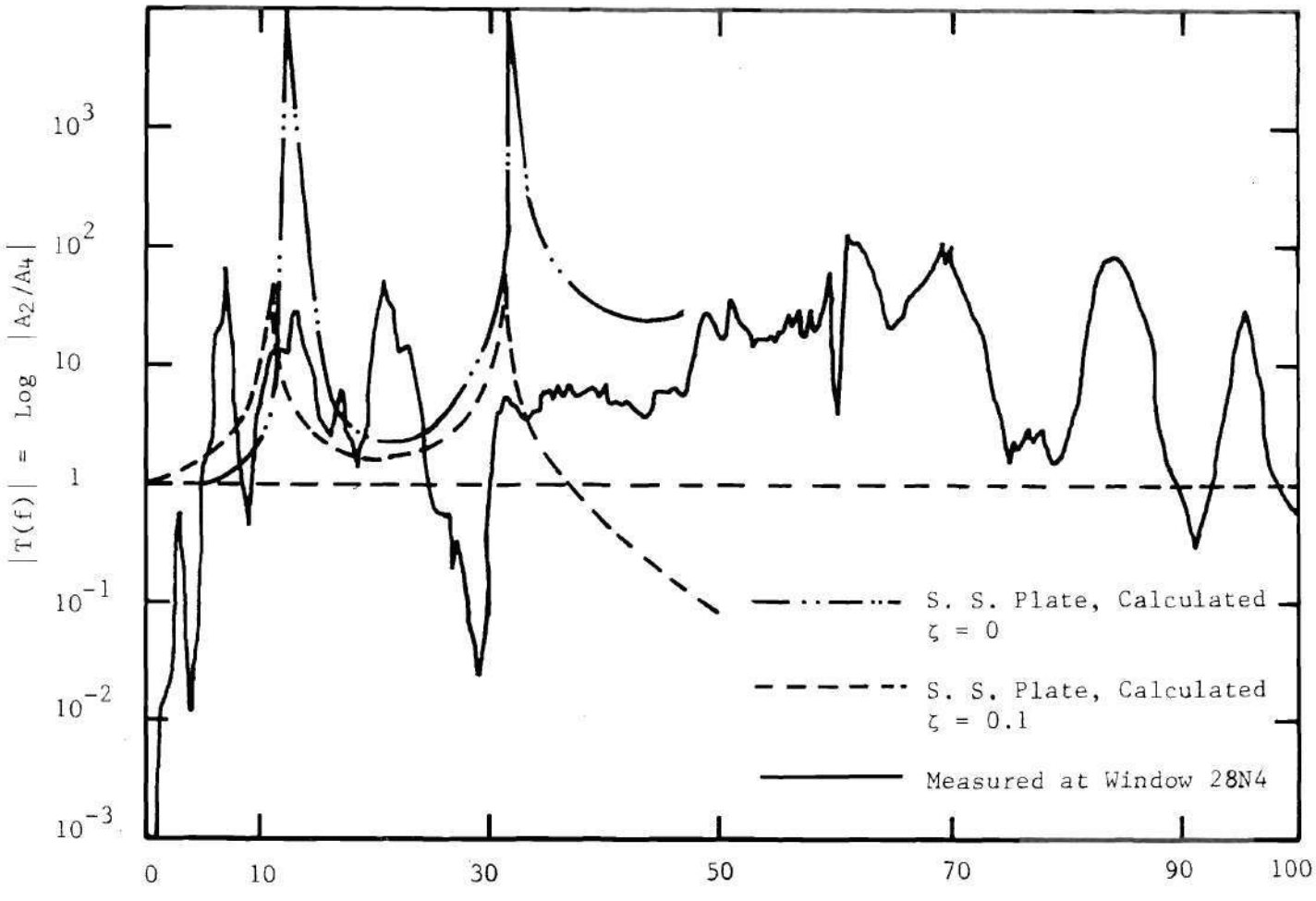

Figure 43. The Transmissibility Function

CHAPTER VI

CONCLUSIONS

Full scale measurements were carried out on a glass clad medium high-rise building to assess the cladding wind loads and characterise the dynamic response of typical window installations. The wind load and the window response were correlated on the basis of linear system theory to evaluate the window response due to wind loads.

The dependence of wind loads on the building profile and on the wind characteristics was investigated and the following features were observed:

1. Higher spectral levels and hence higher dynamic load magnitudes were seen to occur on building faces where the pressure coefficients were predominantly negative.

2. On the windward side, gust effects due to the physical features of the surrounding terrain contribute to the spectral levels. Thus on the windward side the spectral levels increase as the ground floor of the building is approached, i.e., with decreasing height.

3. In regions of separation the spectral levels increase with height.

4. The multiple corners in the building planform appear to act as roughness elements on the building profile. If this roughness is described by the ratio r of a corner side to the length of a flat face of the building then it is seen that a value in the vicinity of $r = 0.2$

tends to randomize the surface pressures. This results in an alleviation of the cladding loads.

5. Discrete flow effects such as vortex shedding, narrow band pressure fluctuations (bandwidth approximately 1 Hz) and spikes in the high frequency band spectra are seen only for some particular combination of the wind direction and the building profile, in the Reynold's number range of $1\text{-}5 \times 10^6$.

6. Exterior architectural features and reverse setbacks together with upflow effects are suspected to be responsible for narrow band and periodic loading.

7. In general, the overall levels of the spectra in the Reynolds number range of $1\text{-}5 \times 10^6$ are quite small and would require considerable dynamic amplification by structural vibration to approach static load levels.

8. The slopes of the spectra differ only slightly from the Kolmogorov spectrum although for low energy levels they tend to be flatter.

The coherence function was used to identify the response levels associated with the wind or pressure loads. The conclusions drawn from the measured coherence function are:

1. The quasi-static response of the window units is primarily due to the differential pressure loading.

2. The wind loads did not bear any significant causality for the window dynamic response in a frequency bandwidth encompassing the first few natural modes. In some cases window excitation in certain modes was due to extraneous sources.

3. An isolated case of high coherence function values in the range of 6-16 Hz was attributed to an unusual combination of the building profile and the flow characteristics. This observation substantiates the hypothesis of critical response locations.

The window unit was modelled as an elastically interconnected double plate system and the natural frequencies of undamped motion obtained. The resonant frequencies of the window unit were also determined in-situ by impulse testing. The difference in the measured and calculated fundamental frequency was approximately 25%. The measured frequency was larger and is consistent with the assumption that the actual support conditions are intermediate between simply supported and clamped.

The transmissibility function of the system was also measured and compared with the calculated transmissibility for an internally damped simply supported single plate. The magnitude of the transmissibility function at the double plate resonant frequencies was seen to be slightly less than the calculated values for a single plate with a damping factor of 0.1. The damping in the window unit is primarily due to the rubber gasket holding the double plates in the frame. The measured transmissibility serves to demonstrate that such a technique can indeed be used to assess any degradation in the gasket material during its service life.

The present study strived to investigate the direct effects of the wind on windows in a tall building from a phenomenological point of view rather than aiming at the acquisition of design wind load information. The wind loads acting on window units were characterized with respect to their frequency content and a qualitative sketch of their dependence on

the building profile was composed. A unique application of the coherence function was utilized to quantify the extent to which the dynamic response of the window units is linearly related to the wind loads. Use of the coherence function also permitted isolation of window vibration sources other than the wind loads, for example rotating machinery in the building. An isolated case of high frequency loading was observed and was attributed to the effects of the surrounding terrain.

The results of this study do not in themselves provide a rational procedure for the wind resistant design of windows. Instead, the results provide an improved understanding of the dynamic wind loading and response mechanisms to be considered in a design philosophy. The study, therefore, is a significant step in the evolution of a rational design procedure.

The problem of designing glass cladding in a tall building, as has been mentioned before, involves a complex interaction of several loading and response mechanisms. Therefore, in order to obtain a complete understanding of the loading and response mechanisms to be considered in window design, several systematic experimental and analytical studies are needed. These are summarized in the following section.

Recommendations For Future Research

The present research has demonstrated that full scale measurements are suited for phenomenological understanding of the loading and response mechanisms, and provide the basis for the development of analytical techniques for load prediction. The actual design loads need to be obtained from simulation studies at the model scale. Full scale

tests, therefore, should be tailored to provide systematic simulation criteria, i.e., a comparison of model and full scale tests is essential.

Measurements on actual structures are also necessary to evaluate the spatial correlation of the pressure loading on the building facade. These data are important for glass clad buildings where motion of the entire curtain wall may be of concern.

The effects of structural distortion (i.e. the entire building frame), under wind loading, on window assemblies needs to be quantified; window loading by building frame motion is of concern in ejection type window failures.

Thermal stresses due to nonuniform exposure of window glass (or for that matter the curtain wall) to sunlight may play a significant part in the combined thermal/wind loading of glass plates, and such conditions should be analytically and experimentally investigated.

APPENDIX A

PROPERTIES OF GLASS

Of interest are the properties of glass which have significance to the engineering problem at hand - breakage of window glass in buildings due to wind-induced loads. Addressed here are the following:

1. Geometric properties of glass used in engineering structures, and
2. Glass strength properties.

Window Glass [67]

The two types of clear glass employed in windows are sheet glass and plate glass. Sheet glass is "drawn" into a flat sheet and annealed. The drawing process gives sheet glass a characteristic surface wave which is clearly discernible, particularly in large sheets. Plate glass is made of one of two processes, both of which are designed to remove or eliminate the surface wave: rolling and polishing, and float. In the polished plate process, rolled glass is polished until a very flat finish is achieved. The float process involves casting the glass on a bed of molten tin so that gravity forces produce very flat surfaces. Plate glass (both polished and float) may be annealed (slow cooling to achieve stress relief), heat strengthened, or tempered (rapid, controlled cooling to achieve "prestressed" condition with tensile stresses in interior and compressive stresses on surfaces; tempered glass has a higher degree of prestress than does heat strengthened glass). Annealed

sheet glass and annealed plate glass are commonly used in glazing the exterior of engineered structures, heat strengthened plate glass is used in upper floors of tall buildings; and tempered plate glass is more expensive and is used principally in doors and first floor windows where safety is a consideration. Failures of tempered plate glass are characterized by fracture into many small pieces called "dicing." Annealed, heat strengthened and tempered plate glass, and annealed sheet glass, can be produced with various tints and reflective characteristics; these additives do not significantly alter the mechanical properties of the glass.

Sheet glass is generally available in thicknesses ranging from 3/32 in. to 1/2 in. Common window glass is usually single strength (SS) sheet glass which is 3/32 in. thick, or double strength (DS) sheet glass which is 1/8 in. thick. Plate glass, both polished and float is generally available in thicknesses ranging from ¼ in. - 1¼ in. Float plate glass is becoming predominant because of manufacturing changeovers to the float process. Sizes that are available relate generally to maximum allowable areas of glass for specific thicknesses as defined in building codes, standards, and manufacturers' technical bulletins. Annealed glass may be cut on the job for glazing, while heat strengthened and tempered glass must be manufactured to specified sizes.

Mechanical Strength

Scientific characterizations of glass strength may be summarized by the following:

(i) Glass fails abruptly without previous yield or permanent deformation.

(ii) Failure in glass always results from a tensile component of stress.

(iii) Glass is much stronger under compressive loads than under tensile loads.

(iv) The spread of breaking stresses obtained from testing a large group of glass specimens is much greater than from a corresponding group of metal specimens, so that the breaking stress for any individual specimen cannot be predicted with accuracy.

(v) Fatigue is pronounced under conditions of static loading (in the ceramicist's definition "fatigue" is the decrease in breaking stress with increased duration of load).

(vi) There is little difference between the effects of static or cyclic load on the fatigue of glass when considered over the same time interval.

(vii) The effect of sample size is pronounced for glass: fine fiber may have many times the nominal strength of larger sections.

(viii) Fractures of glass originate in small imperfections or flaws, the large majority of which are found at the surface.

(ix) The local stress for the slow propagation of a flaw is probably on the order of 1,000,000 psi, but, for fractures by impact, it may be several times this value.

Selected Window Glass Properties

(a) Breaking stresses of annealed glass short-time (3 sec.) flexure in air :

Polished Plate Glass	8,000-16,000 psi
Drawn Window Glass	8,000-20,000 psi

(b) Breaking stresses of annealed glass, tested in air at room temp, as a function of time:

Duration (sec)	Stress (psi)
.01	25,000
.1	20,000
1	16,000
10	13,500
100	11,000
1000	9,500

The PPG Industries Technical Services Report, Products Recommendations (Structural), see also Ref. 23 , presents glass properties in terms of "typical breaking stress," and relates safety factors to the statistical probability of failure (see Table 9). Generally, the ultimate strength of glass varies from a maximum of 20,000 psi when the load is applied in a short period of time (.01 sec) to a minimum of about 3000 psi when the load is sustained for a long period of time.

In summary, it can be seen that the strength of glass is an elusive property. For the current application the literature tells us that the mean fracture stresses in the 15,000-20,000 psi range are

Table 9. The Relationship of Coefficient of Variation, Safety Factor and Statistical Probability of Failure [23].

Regular Annealed Glass (Coefficient of Variation - 25%)		PPG Improved Heat Strengthened Glass (Coefficient of Variation - 20%)	
Safety Factor	Probable # of lights which will break at each occurrence of design load (of each 1000 loaded)	Safety Factor	Probable # of lights which will break at initial occurrence of design load (of each 1000 loaded)
1	500	1	500
2	22	1.67	22
2.5	8	1.92	8
3	4	2.13	4
4	1.3	2.50	1.3
5	Less than 1	2.75	Less than 1

reasonable when impact stresses of millisecond duration are involved, and that mean fracture stresses in the 5000-6000 psi range are reasonable when uniform stresses lasting several seconds are involved. With respect to the variability of glass strength, coefficients of variations of 0.25 are rather universally employed, with these values centered on the above mean strength values.

Table 10 summarizes the elastic constants and the density values used in the calculation of natural frequencies of the double plate system in the present study.

Fracture Mechanics of Glass

The final basic property of glass which deserves attention preliminary to detailed examination of the window damaging mechanism concerns glass failure. In many ways the study of glass response is made easier by the fact that glass fails abruptly without previous yield or permanent deformation. The study of glass response is made more complex, however, because of the intricacies and many unknowns concerning the mechanics of fracture. The fracture mechanism, analysis of the fracture surfaces, analysis of the fracture pattern, and crack propagation velocities are four basic properties of interest.

There is essentially universal agreement that the basic mechanism of glass fracture is directly related to Griffith's well known 'flaw' theory. According to these ideas, the observed strength of glass is always reduced below a so-called "theoretical strength" by the presence of flaws, and the measured strength is determined by the stress

Table 10. Mechanical Properties

Elastic Modulus	10×10^6 psi
Ultimate Strength (Tensile)	5000-6000 psi
Poisson's ratio	0.23
Density	161 lbs/cu.ft.

concentrating action of the "worst" suitably oriented flaw at its apex. Other relevant theories of glass fracture are detailed in Ref. 68 .

APPENDIX B

DYNAMIC RESPONSE OF PRESSURE SENSOR AND TUBE COMBINATION

An estimate of the useable bandwidth (flat response) can be obtained from an analysis of the system shown in Fig. 44. The tube-cavity combination is susceptible to resonsance effects due to wave phenomena and due to linear motion of elemental air mass [69]. The system behaves as a Helmholtz resonator at frequencies where wave effects must be considered. The resonant frequency for a Helmholtz resonator is given by [70]:

$$f_H = \frac{1}{2}\left[\frac{r^2 c^2}{\pi V L}\right]^{\frac{1}{2}}, \quad r \ll L \tag{B-1}$$

$$\lambda = \frac{c}{f_H}, \quad c \sim \text{velo. of sound}$$

When wave effects are insignificant, the linear motion of the air mass and the laminar friction is modelled as a lumped parameter SDOF system described by the following equations:

$$\left|\frac{P}{P_o}\right| = \frac{1}{\left[\left\{1-\left(\frac{\omega}{\omega_n}\right)^2\right\}^2 + 4\zeta^2\left(\frac{\omega}{\omega_n}\right)^2\right]^{\frac{1}{2}}}$$

$$f_n = \frac{1}{2\pi}\sqrt{\frac{3\pi r^2 c^2}{4LV}} \tag{B-2}$$

$$\zeta = \frac{2\mu}{\rho c r^3}\sqrt{\frac{3LV}{\pi}} \qquad \phi = \tan^{-1}\frac{-2\zeta(\omega/\omega_n)}{1-(\omega/\omega_n)^2}$$

See Fig. 45 for notation.

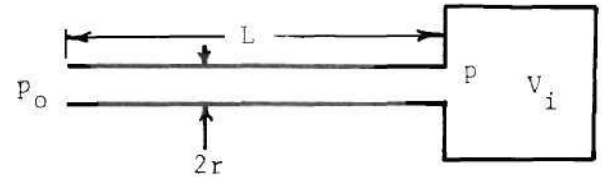

$\mu \sim$ Viscosity

Figure 44. Pressure Transducer as a Helmholtz Resonator

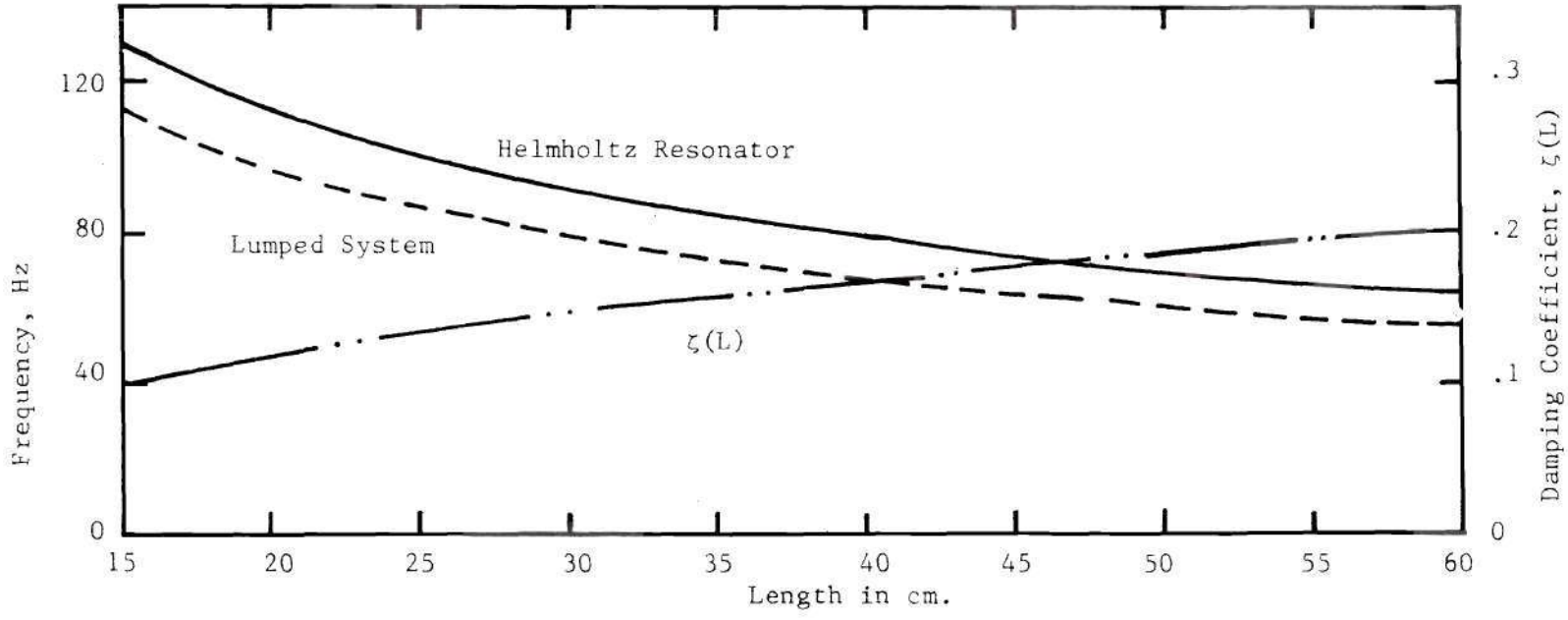

Figure 45. Resonant Frequency of Pressure Transducer as a Function of Tubing Length

Except for large L the frequency $f_H > f_n$. For large values of L, $f_H \simeq f_n$. This can be seen from Fig. 45 where r = 0.0625 in. and corresponds to the smallest diameter in the tubing used with the Barocel. Therefore, the sensor-tube dynamic system acts as a lumped parameter system.

The length L for the Barocel tubing was chosen so as to provide:

1. Maximum flat response bandwidth
2. Linear Phase response

subject to the constraints imposed by the practical aspects of mounting the Barocel. To this end use of Fig. 45 was made and the following table was drawn up:

Table 11. Dependence of f_n on Tubing Length.

L, cm	ζ	f_n Hz	k(-3dB)	$f_u = kf_n$	ϕ linear up to, Hz
15	.1	110	.54	60	40
30	.14	80	.54	43	28.0
45	.18	64	.6	38	23.0
55	.2	58	.6	35	18.0

A length of 45cm (18 in.) was found to be feasible in view of the closest mounting spot and the length of the adapters used. The linear phase is seen from Fig. 45 to correspond to a time delay of approximately 60 ms which has to be taken into account in coherence function computations.

APPENDIX C

AN OPTICAL TECHNIQUE FOR THE MEASUREMENT OF TIME DEPENDENT DISPLACEMENTS

The Laser Displacement Meter (LDM) is an optical device designed for the measurement of time dependent displacements with a particular application in view. The instrument is designed for on-site measurement of the wind-induced deflections of insulating windows in high-rise buildings. The outdoor light of an insulating window is generally inaccessible from within the building so that a method for measuring its displacements without direct contact is required.

Various schemes have been used to provide displacement information without direct contact. Instruments using capacitive effects, inductive effects, or optical radiation are common designs. Capacitive and inductive methods would require treatment of the outdoor light. A variety of optical techniques for contactless measurement of displacements are currently being used. However, some of these require relatively complex processing of the measured results and others were found to be unsuitable since they have a limited range of measurands and are affected by the presence of background illumination. The instrument described here is designed to measure both the angular and linear displacements of the outer light of a doubly glazed window by analyzing the geometric movement of a light beam reflected by it.

Design

The optical system uses a low power He - Ne laser beam directed obliquely onto a plane reflecting surface whose displacements are to be measured. This plane surface returns a reflected beam in accordance with its own motion. The returned beam is intercepted by an array of light position sensors whose output is in turn analyzed to determine the displacements of the plate. From prior considerations in the present application, only the transverse displacement response of the plate was found to be of interest. The reflected beam, however, is deflected from its reference position by the combined effect of the transverse displacement W, and rotations α and β about orthogonal axes in the plane of the plate (slope changes). The effect of one of the rotations, say β, can be largely eliminated by a combination of the following:

(i) Making the plane of reflection perpendicular to the axis of rotation α.

(ii) Using a single axis detector.

(iii) Using a cylindrical lens to form the light beam into a line parallel to the α axis (i.e., axis about which rotation will be measured). This ensures that rotations β will not cause the reflected light to move off of the single axis detector face.

With the use of a cylindrical lens and single axis detectors the reflected beam motion is then caused only by the transverse displacement W and rotation α of the plate. In order to obtain an output proportional to W only, two schemes were devised. The two schemes, one using a single beam (called the "Single Beam System") and the other using two beams

(called the "Double Beam System") are shown schematically in Figures 46 and 47 respectively.

1. The Single Beam System

In a particular configuration of the Single Beam System, the geometric parameters θ, L_1, L_2, $L_d^{(1)}$ and $L_d^{(2)}$ (see Fig. 46) are fixed and the two detector signals proportional to S_1 and S_2 constitute the output. The output is related to W and α in terms of the geometric parameters, but in general the relationships are nonlinear and complicated. However, in the present application the displacements were sufficiently small thus permitting linearization. The output can then be considered as the superposition of effects due to W and due to α taken individually.

From geometric considerations it can be shown that for small displacements the response in terms of S_1 and S_2 may be expressed as:

$$S_1 = 2W \sin\theta + 2L_1^* \cdot \alpha \qquad L_1^* = L_1 + L_d^{(1)}$$

$$S_2 = 2W \sin\theta + 2L_2^* \cdot \alpha \qquad L_2^* = L_2 + L_d^{(1)} \tag{C-1}$$

solving (C-1) for W and α leads to:

$$\alpha = \frac{S_1 - S_2}{2(L_1^* - L_2^*)}$$

$$W = \frac{S_1(L_1^*) - S_1(L_2^*)}{2(L_1^* - L_2^*)\sin\theta} \tag{C-2}$$

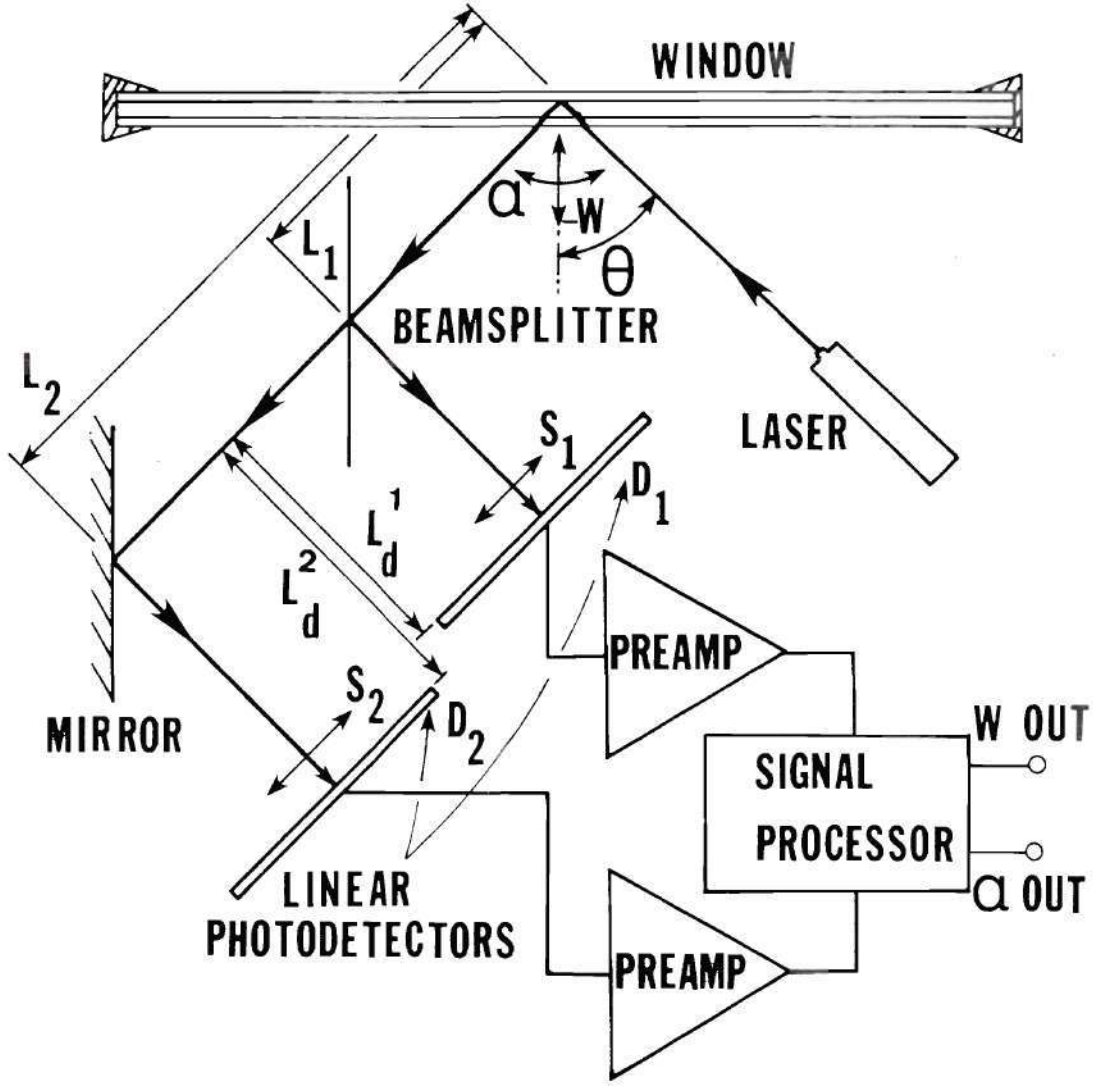

Figure 46. Single Beam System

2. The Double Beam System

The Double Beam System consists of a beam splitter (45^{o}) prism p (Fig. 47) which splits the laser beam into r_1 and r_2 which are then directed by mirrors M_1 and M_2 onto the plate at unequal angles of incidence. Thus the plate in effect 'sees' two sources. The beams reflected by the plate are intercepted by light position sensors D_1 and D_2.

As in the case of the Single Beam System the output is linearly dependent on W and α for sufficiently small values. Analysis of the ray diagram yields the following:

$$W = \frac{S_1 L_d^{(1)} + S_2 L_d^{(2)}}{2(L_d^{(1)} \sin\theta_2 + L_d^{(2)} \sin\theta_1)}$$

$$\alpha = \frac{S_1 \sin\theta_2 - S_2 \sin\theta_1}{2(L_d^{(1)} \sin\theta_2 + L_d^{(2)} \sin\theta_1)} \qquad \text{(C-3)}$$

From equations (C2) and (C3) it is seen that in both systems, for a given geometric configuration, α and W are linearly related to the detector outputs. It is only necessary to choose the geometric parameters such that the response to W is maximized while that to α is minimized.

The causes of nonlinearity and the sensitivities of the two schemes are identical but the Single Beam System is amenable to a more compact mechanical design. Hence the LDM was designed as a Single Beam System.

The detectors used were UDT type LSC-4 which are single axis detectors with a sensor length of 10 cm. The detector output is fed to a

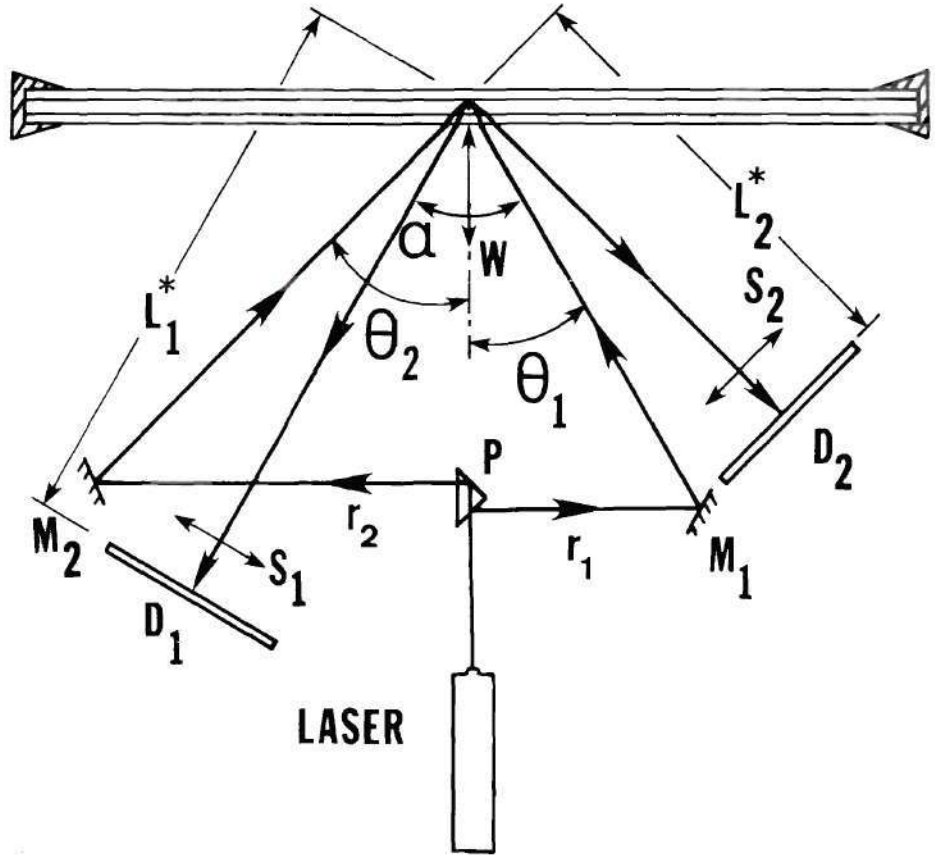

Figure 47. Double Beam System

UDT-301A preamplifier which provides two voltage outputs expressed as:

$$V_{\text{Sum Out}} = 1.125 \times 10^{4} \cdot L \qquad L \sim \text{intensity in watts}$$

$$V_{\text{Diff Out}} = 2834.65\ L \cdot S \qquad S \sim \text{spot position w.r.t sensor entroid in cm} \tag{C-4}$$

for a Lo Sens setting.

The light spot displacement is then expressed as:

$$S = 3.97\ V_d/V_s \text{ cm} \tag{C-5}$$

Once S_1 and S_2 are known for a given configuration the quantities W and α are obtained from Equation (C2). The computation of S_1, S_2, α, and W is performed by a processing circuit whose outputs are proportional to W and α. Figure 48 shows a block diagram of the detector electronics.

Performance

The calibration of the LDM was carried out with the aid of a calibrating device which provides a W input with an accuracy better than 0.003 cm and an α input with an accuracy better than 0.03 degrees. Typical input-output curves are shown in Figs. 49 and 50 for a geometrical configuration characterized by $L_1^*/L_2^* = 0.485$ and $\theta = 45^{\circ}$.

As expected from Equation (C2), the relations W vs. V_W and α vs. V_α are very linear and maybe expressed as:

$$V_W = S_W \cdot W$$

$$V_\alpha = S_\alpha \cdot \alpha \tag{C-6}$$

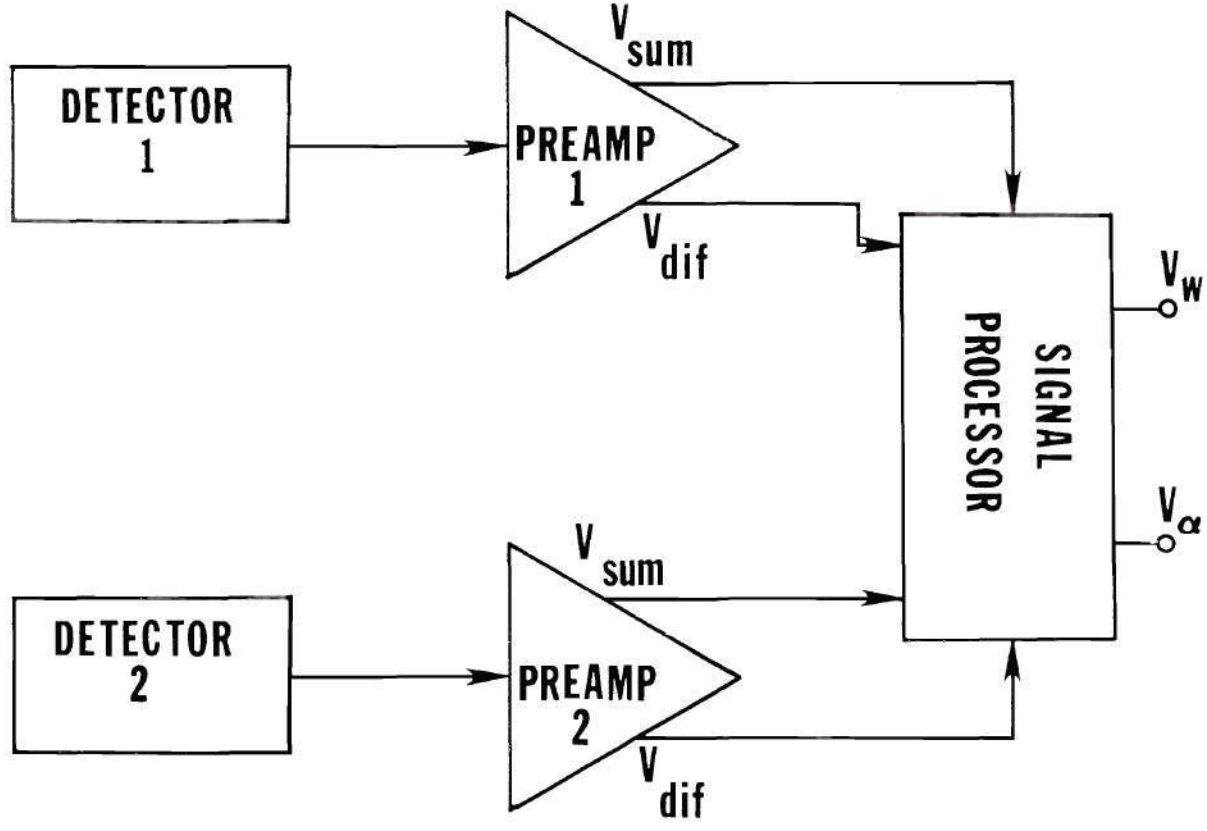

Figure 48. Schematic of Detector Electronics

where S_W and S_α are sensitivities of the LDM to W and α inputs, respectively. Their values, obtained as the slope of a least squares fit straight line, for $L_1^*/L_2^* = 0.485$ and $\theta = 45^o$ are shown in Figs. 49 and 50. The absolute value of the sensitivity can be changed by changing the gain of the signal-processor.

The frequency response of the LDM is limited by the response of the detectors and associated electronics. The calculated bandwidth is approximately 10 kHz. The range of W for the above configuration is 2.5 cm (i.e., -1.25 cm to + 1.25 cm) which is more than adequate for the present application. The maximum deviation of any measured point from the fitted straight line was less than 3% (F.S.).

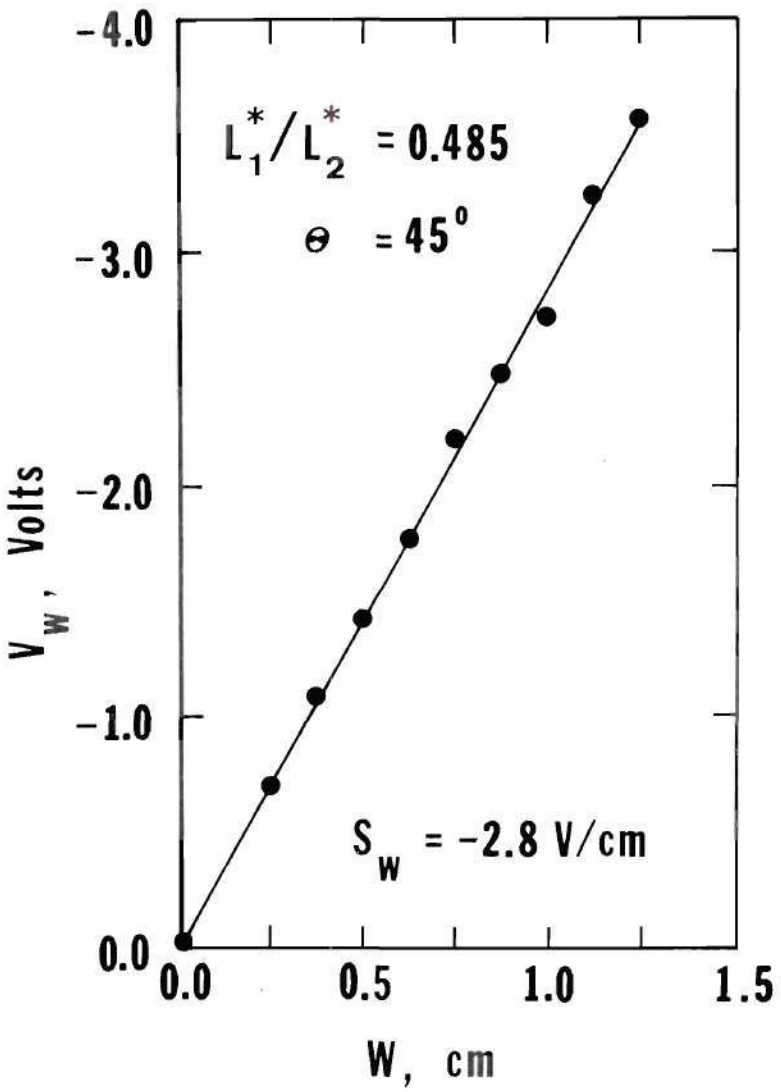

Figure 49. Sensitivity S_W

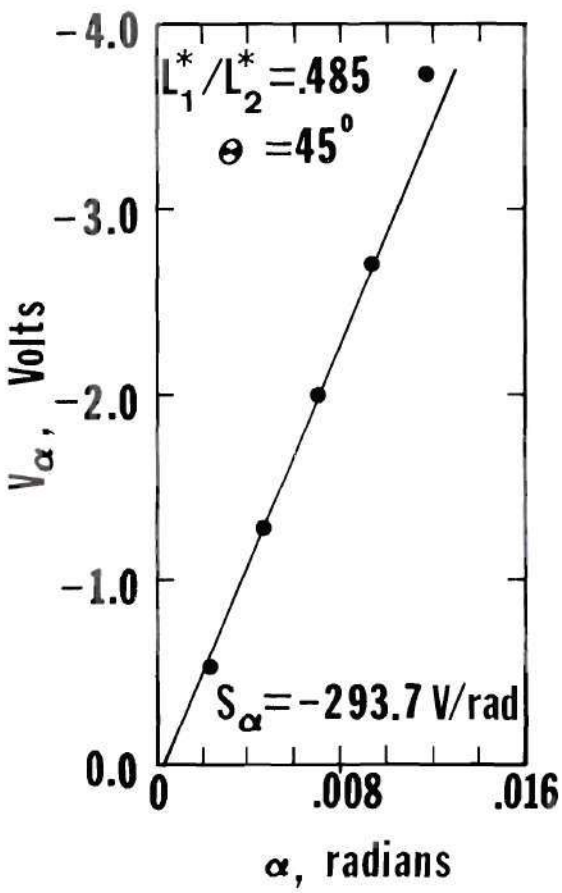

Figure 50. Sensitivity S_α

APPENDIX D

PROCEDURE FOR STATIONARITY TEST

The stationarity of the data was evaluated from sample time history records. In order to ascertain the stationarity from individual sample records, the following assumptions were made:

1. Any given sample will properly reflect the nonstationary character of the random process. This is a reasonable assumption for those nonstationary processes which involve deterministic trends.

2. Any given sample record is very long compared to the lowest frequency component in the data, excluding a nonstationary mean.

3. Any nonstationarity of interest will be revealed by time trends in the mean square value of the data.

With these assumptions in mind, the stationarity of the random data was tested by investigating a single record $x(t)$ as follows:

1. Divide the sample record into N equal time intervals where the data in each interval may be considered independent.

2. Compute a mean square value (or mean value and variance separately) for each interval and align these sample values in time sequence, as follows -

$$\overline{x_1^2},\ \overline{x_2^2},\ \overline{x_3^2},\ \ldots,\ \overline{x_N^2}$$

3. Test the sequence of mean square values for the presence of underlying trends or variations other than those due to expected sampling variations.

It is now hypothesized that the sequence of sample mean square values $\overline{x_1^2}$, $\overline{x_2^2}$, . . ., $\overline{x_N^2}$ are each independent sample values of a random variable with a mean square value of Ψ_x^2. Since the sampling distribution of the sample values is not known a priori, the hypothesis is tested by a nonparametric approach. One such nonparametric test which was applied to the present problem is the run test described in Ref. 31. A run is defined as a sequence of identical observations that is followed and preceded by a different observation or no observation at all.

If the above hypothesis is true, the variations in the sequence of sample values will be random and display no trends. Now, if the runs in the sequence are defined with respect to a median value as say (+) and (-), where (+) signs are assigned to the values in the sequence greater than the median value, then the number of runs in the sequence will be as expected for a sequence of independent random observations of the random variable, which are tabulated. If the number of runs is significantly different from the expected number for a known confidence level, the hypothesis of stationarity will be rejected. Otherwise, one would fail to reject the hypothesis.

Results of a representative stationarity test performed on the actual data are shown in Table 12. The mean square values obtained are not calibrated.

The median value of the 20 observations is 134, say, then the number of runs is 7, which lies between the extremes of 5 and 16 required for a 99% confidence test. Hence the hypothesis of stationarity is accepted.

Table 12. A Typical Run From the Pressure Data

#	1	2	3	4	5	6	7	8	9	10
$\hat{\psi}_x^2 \times 10^5$	1073	1123	487.6	169.1	1027	132.5	598.7	490.8	75.3	133.0
Runs	+	+	+	+	+	−	+	+	−	−
			1			2		3		4

#	11	12	13	14	15	16	17	18	19	20
$\hat{\psi}_x^2 \times 10^5$	155	18.68	82.0	60.53	5.054	34.37	97.6	19.18	1357	527.3
Runs	+	−	−	−	−	−	−	−	+	+
	5				6					7

REFERENCES

1. Martin, C. S., and Craig, J. I., "Window and Curtainwall Performance In Highrise Buildings," Research Proposal Submitted to the National Science Foundation, May 1973, Georgia Institute of Technology.

2. Minor, J. E., and Beason, W. L., "Window Glass Failure in Windstorms," ASCE National Structural Engineering Convention, April 14-18, 1975, New Orleans, La. Meeting Preprint 2486.

3. Eaton, K. J., "Cladding and the Wind," ASCE National Structural Engineering Convention, April 14-18, 1975, New Orleans, La. Meeting Preprint 2436.

4. Gannon, Robert, "Wind Engineering," Popular Science, October, 1975, pp. 84.

5. Cermak, J. E., "Separation-Induced Pressure Fluctuations on Buildings," Proceedings of the Seminar on Wind Loads on Structures, University of Hawaii, October 1970, pp. 55.

6. Peterka, Jon A., and Cermak, J. E., "Wind Pressures on Buildings-Probability Densities," Transactions ASCE Structures Division, June 1975 Proc. Paper 11373.

7. Ostrowski, J. S., Marshall, R. D. and Cermak, J. E., "Vortex Formation and Pressure Fluctuations on Buildings," International Research Seminar on Wind Effects on Buildings and Structures, Ottawa, Canada, 11-15 September, 1967, Vol 1.

8. Cermak, J. E., and Sadeh, W. Z., "Pressure Fluctuations on Buildings," Proceedings of the Third International Conference on Wind Effects on Buildings and Structures, Tokyo, 1971, pp. 189-198.

9. Symposium on Full-Scale Measurements of Wind Effects on Tall Buildings and Other Structures, June 23-29, 1974, University of Western Ontario, London, Canada. Description of Conference. Appendix 2. Journal of Industrial Aerodynamics, 1 (1975), pp. 126-137.

10. Newberry, C. W., et. al., "The Nature of Gust Loading on Tall Buildings," Loc. Cit. Ref. 7.

11. Dalgliesh, S. A., "Comparison of Model/Full Scale Wind Pressures on a High Rise Building," J. Ind. Aerod. 1 (1975) 55-66.

12. Dalgliesh, W. A., "Statistical Treatment of Peak Gust on Cladding," J. ASCE Structural ST9, Vol. 97, Sept. 1971, p. 2173.

13. Dalgliesh, W. A., et. al., "Wind Pressure Measurements on a Full-Scale High Rise Office Building," Loc. Cit. Ref. 7.

14. Takeuchi, M., et. al., "Actual Fluctuating Wind Pressures on a Tall Building and Its Response," Loc. Cit. Ref. 8, pp. 285.

15. Standen, N. M., Dalgliesh, W. A., and Templin, R. J., "A Wind Tunnel and Full Scale Study of Turbulent Wind Pressures on a Tall Building," Loc. Cit. Ref. 8.

16. Miyoshi, S., et. al., "Wind Pressure Coefficients on Exterior Wall Elements of Tall Buildings," Loc. Cit. Ref. 8, pp. 273.

17. Davenport, A. G., and Dalgliesh, W. A., "A Preliminary Appraisal of Wind Loading Concepts of the 1970 Canadian National Building Code," Loc. Cit. Ref. 8, pp. 441.

18. Cohen, E., and Vellozzi, J., "Proposed American Standard Building Code Requirements for Minimum Design Wind Loads," Wind Effects on High Rise Buildings, Proceedings of the Chicago Design Symposium March 23, 1970, Northwestern University, Evanston, Ill.

19. Hershey, R. L., and Higgins, T. H., "Design of Windows for Dynamic Loading," Sound and Vibration, Vol. 9, No. 3, March 1975, pp. 18.

20. American National Standard Building Code Requirements for Minimum Design Loads in Buildings and Other Structures, ANSI A58.1-1972, American National Standards Institute, New York.

21. National Building Code of Canada 1970, Issued by the Associate Committee on the NBC, NRC Ottawa, Canada.

22. Southern Standard Building Code, Southern Building Code Congress, Birmingham, Alabama, 1969.

23. Architectural Glass Products, PPG Industries, Jan. 1974.

24. Allen, D. E., and Dalgliesh, W. A., "Dynamic Wind Loads and Cladding Design," The Preliminary Publication of the International Association of Bridge and Structural Engineering Symposium held in Lisbon, 1973, pp. 279-285.

25. Ishizaki, H., "On the Wind Resistant Design of Exterior Cladding," *National Conference on Planning and Design of Tall Buildings, Proc.* Pap. Tokyo, Japan, Aug. 28-30, 1973.

26. Ishizaki, H., "On the Design of Glass Pane Against Wind Loading," Ind. Aerod. Abstracts 2.273A7.

27. Khan, F. R., "A Rational Method for the Design of Curtain Walls," Loc. Cit. Ref. 18, pp. 145.

28. Saffir, H. S., "Hurricane Camille: Data on Storm and Structural Damage," Loc. Cit. Ref. 8, pp. 457.

29. Sage, A. P., "System Identification History, Methodology, Future Prospects," in System Identification of Vibrating Structures, ASME, Ed. W. D. Pilkey and R. Cohen, 1972.

30. Meirovitch, L., Analytical Methods in Vibrations, Macmillan, London, 1967.

31. Bendat, J. S. and Piersol, A. G., Random Data: Analysis and Measurement Procedures, 1971, Wiley-Interscience.

32. Snowdon, J. C., "Forced Vibration of Internally Damped Rectangular and Square Plates With Simply Supported Boundaries," Journal of the Acoustical Society of America, Vol. 56, No. 4, pp. 1177, Oct. 1974.

33. Snowdon, J. C., "Mechanical Four-Pole Parameters and Their Applications," Journal of Sound and Vibration, Vol. 15, No. 3, pp. 307-323, April 1971.

34. Davenport, A. G., Discussion of Ref. 6, Journal of the Structural Division, ASCE, Vol. 102, No. ST11, Nov. 1976, pp. 2235.

35. Bendat, J. S. and Halvorsen, W. G., "Noise Source Identification Using Coherent Output Power Spectra," Sound and Vibration, Aug. 1975.

36. Roth, Peter, Hewlett Packard Application Note 140-1.

37. Carter, G. C. et. al., "Coherence and its Estimation via the Partitioned Modified Chirp-Z Transform," IEEE Transactions on Acoustics, Speech, and Signal Processing, June 1975.

38. Hinich, M. J., and Clay, C. S., "The Application of the Discrete Fourier Transform in the Estimation of Power Spectra, Coherence, and Bispectra of Geophysical Data," Review of Geophysics, Vol. 6, No. 3, August 1968, pp. 347.

39. Loc. Cit. Ref. 29.

40. Davenport, A. G., "A Rationale for Determination of Design Wind Velocities," Proceedings ASCE, J. Structural Div., Vol. 86, 1960, pp. 39-60.

41. Loc. Cit. Ref. 9, Appendix 1, pp. 19.

42. Schiff, A. J., "Evaluation of Pressure Transducers for Full Scale Testing," in Proceedings ASCE-EMD Specialty Conf., UCLA, March 30-31, 1976.

43. Harper, J. J., and Palfrey, J. G., "Tower Place Wind Tunnel Test," Georgia Institute of Technology, Project No. E15-300-2AA.

44. Otnes, R. K., and Enochson, L. D., Digital Time Series Analysis, 1972, Wiley-Interscience.

45. Jenkins, G. M., and Watts, D. G., Spectral Analysis and Its Applications, 1968, Holden Day, San Francisco.

46. Potter, R. W., "Compilation of Time Windows and Line Shapes for Fourier Analysis," Hewlett-Packard Co., Publication 1970.

47. Oliver, B. M., and Cage, John M., Electronic Measurements and Instrumentation, 1971, McGraw-Hill, New York.

48. Enochson, L. D., and Goodman, N. R., "Gaussian Approximation to the Distribution of Sample Coherence," Measurement Analysis Corp., Los Angeles, Ca., Contract Report AFFDL TR-65-57, Jun. 1965.

49. Carmichael, T. E., "The Vibration of a Rectangular Plate With Edges Elastically Restrained Against Rotation," Quart. Journ. Mech. and Applied Math., Vol XII, pt. 1, 1959, pp. 29.

50. Freynik, H. S., "The Nonlinear Response of Windows to Random Noise," NASA TN D-2025.

51. Talbot, C. R. S., "Coherence Function Effects on Phase Difference Determination," J. Sound and Vibration, (1975) 39 (3), pp. 345-358.

52. Carter, G. C., et. al., "Estimation of the Magnitude-Squared Coherence Function via Overlapped Fast Fourier Transform Processing," IEEE Trans. on Audio and Electroacoustics, Vol. Au-21, No. 4, August 1973.

53. Hart, G. C., et. al., "System Identification in Structural Dynamics," Loc. Cit. Ref. 42.

54. Schiff, A. J., "Identification of Large Structures Using Data From Ambient and Low Level Excitations," Loc. Cit. Ref. 29.

55. Ramsey, K. A., "Effective Measurements for Structural Dynamics Testing," Sound and Vibration, April 1976, Vol. 10, No. 4, pp. 18.

56. Richardson, M., and Potter, R. W., "Identification of the Modal Properties of an Elastic Structure from Measured Transfer Function Data," presented at the 20th ISA Symposium, May 21-23, 1974, Albuquerque, N. M.

57. Richardson, M., "Modal Analysis Using Digital Test Systems," presented at Seminar on Understanding Digital Control and Analysis in Vibration Test Systems, Goddard Space Flight Center, Md.

58. Kennedy, C. C., and Pancu, C. D. P., "Use of Vectors in Vibration Measurement and Analysis," J. Aero. Sci., Vol. 14, No. 11, Nov. 1947.

59. Craig, J. I., and Palfrey, J. G., "Full-Scale Wind Pressure Simulation for Window and Curtain Wall Structures," in ASCE/EMD Specialty Conference Proceedings, Dynamic Response of Structures, March 30, 1976.

60. Wiener, N., "Generalized Harmonic Analysis," Acta Mathematica 1930, Vol. 55, pp. 117-258.

61. Shapiro, A., "Estimation of Coherence Between Signal and Signal Plus Echoes," Bell Telephone Labs. Tech. Man., Whippany, N. J., 1963.

62. Akaike, H., "Statistical Measurement of Frequency Response Functions," Annals of the Institute of Statistical Mathematics, Supplement III, 1964, pp. 5-17.

63. Dean, W. C., Enochson, L. D., and Shumway, R. H., "The Coherency Analysis of Seismic Noise," SDLR 155, Air Force Technical Applications Center, Washington, D. C., July 1966.

64. Kaneshige, I., "Frequency Response of an Automobile Engine Mounting," Annals of the Institute of Statistical Mathematics, Supplement III, 1964, pp. 49-57.

65. Barnoski, R. L., "Ordinary Coherence Functions and Mechanical Systems," J. Aircraft, Vol. 6, No. 4, April 1969, pp. 372.

66. Goff, K. W., "The Application of Correlation Techniques to Some Acoustic Measurements," Journal of the Acoustical Society of America, Vol. 27, No. 2, March 1955.

67. Minor, J. E., "Window Glass in Windstorms," Civil Engineering Report Series CE 74-01, Texas Tech University, May 1974 (NTIS Accessions No. PB-232 258/AS).

68. Pye, L. D., Stevens, H. J., and LaCourse, W. C., Introduction to Glass Science, Plenum Press, New York, 1972.

69. Doebelin, E. O., Measurement Systems: Applications and Design, pp. 391, McGraw-Hill, 1975.

70. Holman, J. P., Experimental Methods for Engineers, McGraw-Hill, 1966, pp. 155.